arXiv:1211.6270v1 [cond-mat.mtrl-sci] 27 Nov 2012

THESE DE DOCTORAT DE
L'UNIVERSITE PIERRE ET MARIE CURIE

Spécialité

Ecole Doctorale en Physique et Chimie de Matériaux
(ED397)

Présentée par

Mlle Lucia CARAMELLA

Pour obtenir le grade de

DOCTEUR de l'UNIVERSITÉ PIERRE ET MARIE CURIE

Sujet de la thèse :

Theoretical spectroscopy of realistic condensed matter systems

soutenue le 3 Février 2009

devant le jury composé de :

M. Mébarek ALOUANI, Professeur Université Louis Pasteur, Rapporteur

M. Stefano OSSICINI, Professeur Université de Modena e Reggio Emilia, Rapporteur

M. Yves BORENSZTEIN, Directeur de Recherche CNRS Université Pierre et Marie Curie, Examinateur

M. Davide Emilio GALLI, Chercheur Université de Milan, Examinateur

M. Fabio FINOCCHI, Directeur de Recherche CNRS Université Pierre et Marie Curie, Directeur de thèse

M. Giovanni ONIDA, Professeur Université de Milan, Directeur de thèse

Università degli Studi di Milano
Dottorato di ricerca in Fisica, Astrofisica e Fisica Applicata
and
Université Pierre et Marie Curie
Ecole Doctorale Physique et Chimie de Matériaux

Theoretical spectroscopy of realistic condensed matter systems

s.s.d. FIS/03

Director of the Doctoral School (I): Prof. Gianpaolo BELLINI

Director of the Doctoral School (F): Prof. Jean–Pierre JOLIVET

Thesis Director: Prof. Giovanni ONIDA

Thesis Director: Dr. Fabio FINOCCHI

PhD Thesis of:
Lucia CARAMELLA
Ciclo XXI

Academic year: 2008/2009

Contents

Introduction **1**

I Theory **5**

1 Theoretical background **7**
1.1 The Schrödinger equation for condensed matter systems 7
1.2 The variational formulation 9
1.3 Density functional theory 9
1.3.1 Hohenberg-Kohn theorem 10
1.3.2 The Kohn-Sham equations 11
1.4 Methods 13
1.4.1 Local density approximation 13
1.4.2 Local spin density approximation 14
1.4.3 Generalized gradient approximation 15
1.4.4 Brief review of pseudopotential method 15
1.5 Time dependent density functional theory 16
1.6 Linear response 18
1.6.1 Adiabatic (spin) local density approximation 20
1.7 Dielectric function 20

2 Surface spectroscopies **23**
2.1 Experimental issues 23
2.1.1 Preparation and structural properties 24
2.1.2 Electronic properties 26
2.1.3 Reflectivity anisotropy experimental spectroscopy 28
2.1.4 Electron energy loss spectroscopy at surfaces 30
2.2 Theoretical surface spectroscopies 31

2.2.1 The slab method 31
2.2.2 Real–Space slicing technique 31
2.2.3 Theory of RAS 33
2.2.4 Theory of electron energy loss at surfaces 36

II Development 39

3 Efficient calculation of the electronic polarizability 41
3.1 Motivations 41
3.1.1 Local filed effects 43
3.2 Theoretical framework 44
3.2.1 Fundamental ingredients 44
3.2.2 The Hilbert-transform approach 46
3.2.3 Numerical efficiency for a toy system 48
3.3 Optical properties of oxidized Si(100)-(2×2) 49
3.4 Computational scaling and performances 54
3.5 Conclusions 57

III Applications 59

4 The clean Si(100) surface 61
4.1 Si(100): which reconstruction? 61
4.2 First principle scheme 63
4.3 Geometric structure 63
4.4 Computational aspect 65
4.4.1 Broadening 66
4.4.2 Slicing methods 66
4.4.3 Detector integration 67
4.5 Calculated spectra for Si(100) 69
4.5.1 Reflectivity anisotropy spectra 70
4.5.2 Calculated REELS spectra at $E_0 = 40$ eV 70
4.5.3 Calculated REELS spectra at low energy 73
4.5.4 Analysis of spectra 75
4.5.5 Discussion 77
4.6 Conclusions 81

5 The oxidized Si(100) surface 83
5.1 Atomic structure 83
5.2 Electronic structure and the effect of oxidation 88
5.3 Experimental energy loss data 91
5.4 Theoretical energy loss spectra 92
5.4.1 Clean versus oxidized Si(100): the low-energy part of the spectrum 93
5.4.2 Clean versus oxidized Si(100): REEL spectra in a wider spectral reagion 93
5.5 Conclusions 97

6 Subtleties in electronic excitations of open shell molecules 99
6.1 Brief review of TDDFT for isolated systems 99
6.2 Closed and open shell systems: the problem of the correct counting of excitations 101
6.2.1 Closed shell systems 102
6.2.2 The problem of the open shell systems 103
6.3 A simple open shell molecule: BeH 105
6.4 Energy levels and density of states 106
6.4.1 Convergence issues 109
6.5 Excitation energies 111
6.6 Conclusions 113

7 A paradigmatic case for semicore and spin-polarization effects in electronic spectra of solids: bulk iron 115
7.1 Pseudopotentials for iron 115
7.2 Properties of bulk iron 118
7.2.1 Structural properties 118
7.3 Electronic properties 119
7.3.1 Electronic properties 119
7.4 Optical conductivity 125
7.5 Conclusions 126

8 Iron, cobalt and nickel pyrites 129
8.1 Motivations 129
8.2 Structural and magnetic properties 131

8.3 Electronic properties 134
8.4 Conclusions 137

Scientific contributions **141**

A Determination of second derivative spectra **143**

Bibliography **143**

List of Figures

2.1 LEED, STM (experiments) 26
2.2 Surface Brillouin Zone 27
2.3 RAS (experiments) 29
2.4 EELS excitations 30
2.5 Three Layers Model 32
2.6 RAS geometry 34
2.7 REELS geometry 36
2.8 Three Layers Model 37

3.1 Accuracy HT method 48
3.2 Time scaling HT method (model system) 49
3.3 Si(100)-p(2×2):O (1ML) Imaginary part of the dielectric function . . 50
3.4 Si(100)-p(2×2):O (1ML) 51
3.5 Si(100)-p(2×2):O (1ML) - RAS 52
3.6 Si(100)-p(2×2):O (1ML) - SDR 53
3.7 Time scaling HT method (real system) 56

4.1 Bulk silicon lattice parameter 64
4.2 Si(100)-$p(2 \times 1)$, -$p(2 \times 2)$ and -$c(4 \times 2)$ 64
4.3 EELS: band convergence 65
4.4 Broadening in the calculated EELS 67
4.5 Si(100)-$c(4 \times 2)$ slab 68
4.6 Integration geometry 68
4.7 Integration method 69
4.8 Detector size 69
4.9 Si(100)-$c(4 \times 2)$, $p(2 \times 2)$ and $p(2 \times 1)$: RAS 71
4.10 REELS E_0 =40 eV: Si(100)-$c(4 \times 2)$, $p(2 \times 2)$ and $p(2 \times 1)$ 72
4.11 REELS E_0 =40 eV with bulk contributions: Si(100)-c(4×2) 73

4.12 HREELS experimental data 74
4.13 REELS at $E_0 = 7$ eV: Si(100)-$p(2 \times 1)$, $p(2 \times 2)$ and $c(4 \times 2)$ 75
4.14 Si(100) - HREELS and dielectric function 76
4.15 Si(100)-c(4×2) total oscillator strenght S_2 77
4.16 Si(100)-c(4×2) total oscillator strenght S_1 78
4.17 Si(100)-c(4×2) isosurface plots of $|\psi_{n\mathbf{k}}(r)|^2$ 79
4.18 Si(100)$c(4 \times 2)$ and -$p(2 \times 1)$: band structure 79

5.1 Si(100):O - 1E′, 1D and 1D Si=O models 84
5.2 Si–O related models of Si(100):O (1ML) 86
5.3 Si(100):O - total energy configurations 88
5.4 Si(100):O 1E′, 1D: band structure 89
5.5 Si(100):O 1D Si=O moled: band structure 90
5.6 Si(100)-p(2×1) vs $p(2 \times 1)$ Si=O band structure 91
5.7 Experiments: EEL second derivative spectra 92
5.8 Si(100)-$c(4 \times 2)$ vs Si(100)-$c(4 \times 2)$:O 1D, 1E' and 1D Si=O: REELS at $E_0 = 40$ eV 94
5.9 Si(100)-$c(4 \times 2)$, 1D and 1E': REELS 95
5.10 Si(100)-$c(4 \times 2)$, 1D Si=O, $p(2 \times 2)$ 1D Si=O, B and C: REELS . . 96

6.1 Excitations for a closed shell system 102
6.2 Excitations for an open shell system 104
6.3 BeH molecule 106
6.4 BeH: spin resolved KS energy levels 107
6.5 BeH: spin resolved DOS 108
6.6 BeH: supercell 109
6.7 BeH: convergence 111

7.1 Iron: wave functions 117
7.2 Iron: PP transferability 117
7.3 Birch–Murnaghan EOS for iron 119
7.4 Spin resolved DOS of BCC iron 120
7.5 Spin resolved band structure of BCC iron 122
7.6 Valence bands of BCC iron 123
7.7 Fe-3s splitting 124
7.8 Iron: optical conductivity 126

8.1 Schematic representation of metal and half metal 130

8.2 Schematic representation of spin transport 131
8.3 Pyrite structure 132
8.4 Isosurfaces of $|\psi_{n\mathbf{k}}(\mathbf{r})|^2$ for $\mathrm{CoS_2}$ 133
8.5 Isosurfaces of $|\psi_{n\mathbf{k}\uparrow}(\mathbf{r})|^2$ and $|\psi_{n\mathbf{k}\downarrow}(\mathbf{r})|^2$ for $\mathrm{FeS_2}$, $\mathrm{CoS_2}$ and $\mathrm{NiS_2}$. . . 134
8.6 Spin resolved DOS of $\mathrm{FeS_2}$, $\mathrm{CoS_2}$, $\mathrm{NiS_2}$ 136

A.1 Second derivative spectra of EEL 144

List of Tables

5.1 Structural lengths of Si(100):O 84
5.2 Energetics of Si(100):O configurations studied 87

6.1 Energy levels of BeH 110
6.2 Excitation energies of BeH 112

7.1 Iron: lattice parameter 119
7.2 Core states splitting of iron 121

8.1 Optimized S–S distances FeS_2, CoS_2 and NiS_2 132

Introduction

A deep understanding of the interaction between matter and radiation (including electrons and light) is a key issue in order to describe the physical nature and the properties of materials. This can be achieved with a joint effort of numerical simulations and experiments. In fact, the physical origin of the experimental spectral features can often be understood unambiguously with the help of numerical simulations.

Nowadays numerical computation of ground state properties of condensed matter systems can be successfully treated within the density functional theory (DFT). In this context, the problem of solving the Schrödinger equation for the ground state of a many body system can be exactly recast into the variational problem of minimizing an energy functional with respect to the charge density. The success of this approach has been shown during the last years by ab initio calculations describing the ground state properties of realistic systems, in particular in case of reconstructed surfaces. However, ground state properties are not enough to describe those experiments involving excitations of the electronic system. In most cases, an external probe modifies the charge distribution of the sample, producing excited states and a dynamical rearrangement of the density.

In the last years, excited state theories providing an overcome of limits of DFT have been proposed. A particularly fruitful attempt to go beyond the ground state theory is offered by time dependent density functional theory (TDDFT), providing an exact reformulation of quantum mechanics in terms of time evolving density. Within this theory, the complexity of the problem is confined to the exchange–correlation potential V_{xc}, whose analytic form is unknown but several approximations are available in literature, giving correct predictions in many realistic cases. However, in many interesting applications, the simpliest approximation (as independent particle RPA) are successful. This is the case, for example, of the simulation of the surface optical spectroscopy, such as reflectivity anisotropy (RA) or differential spectroscopy (SDR).

On the other hand, new experiments require more complete theories including, for example, spin degree of freedom in order to treat magnetic systems, or local field effects in order to describe strong anisotropic systems, or the inclusion of semicore and core levels in order to obtain information about core and semicore spectroscopies. It is hence important to implement these more complete theories in ab initio computational codes in order to describe more realistic condensed matter systems. In particular, these implementations are fundamental to be able to treat systems with explicit inclusion of surfaces, or isolates sytems. Moreover, new more efficient algorithms are essential and the improvement of existing codes is required in order to extend the range of numerical simulation applicability to systems with a larger size (in terms of number of atoms).

Theoretical spectroscopy is a successful combination of these quantum theories and computer simulation intended to describe the fundamental mechanisms of interaction between materials and perturbing external fields.
The present work is an example of what is possible to obtain with the theoretical and numerical tools we have just mentioned. In particular, we will discuss problems of numerical efficiency and the inclusion of some aspects neglected up to now, such as the inclusion of spin variable and semicore levels.

This manuscript contains different parts: a thread can be drawn from the technical development of methods, to simulations of a variety of physical systems. Moreover, the study of a large variety of complex physical applications helps to point out the limits and the advantages of the theories adopted.
After a brief review of the theoretical background presented in chapter 1, in chapter 2 we describe in details the methods used to simulate surface spectroscopies and the main experimental techniques.
From the following chapter, we approach the core of the work developed in this thesis, in paticular in chapter 3 we focus on the dynamical response function $\chi(\mathbf{r}, \mathbf{r}', \omega)$ and we present the developement of an Hilbert transform (HT) based method to evaluate the independent particle response. The time scaling analysis of the HT–method on a model shows that it is convenient for large systems. As an application, we studied the crystal local field effects on the optical spectra of the Si(100)-(2×2) surface, weakly oxidized. In chapters 4 and 5, we focused RA and EEL spectra of clean and oxidized Si(100) surfaces. Chapter 4 is devoted to the clean surface, for which we discuss the spectra calculated on three reconstructions: p(2×1), p(2×2) and c(4×2). The oxidation process of this surface is then analyzed in chapter 5, where several oxygen adsorption sites are studied through geometric optimization

and calculation of EEL spectra.

The following part of this manuscript is devoted to spin polarized systems. The limits of DFT and TDDFT-LDA approach are highlighted in the case of BeH, a simple molecule with unpaired number of electrons (see chapter 6). The successful calculation of the optical conductivity for bulk iron is then presented in chapter 7 and spin resolved electronic properties of this system are provided including the $3s$ and $3p$ semicore states.

In the last part of the manuscript, chapter 8, it is summarized the interesting electronic and magnetic properties of iron, cobalt and nickel pyrites. These compounds are complex spin polarized systems that could have stimulating applications in the new field of spin electronics.

Part I

Theory

Chapter 1

Theoretical background

The problem of finding the electronic ground state of a condensed matter system is equivalent to solve the fundamental equation of quantum mechanics, i.e. the Schrödinger equation for a set of interacting electrons immersed in an external potential. The Density Functional Theory (DFT) provides a successful tool to treat the problem giving a variational reformulation of the equations in terms of the electronic density. In this chapter we briefly review this theory. The fundamental theorems and its Time Dependent generalization (TDDFT) is reviewed with a presentation of the methods used in this thesis for the numerical simulation of realistic systems.

1.1 The Schrödinger equation for condensed matter systems

The non-relativistic time-indipendent Schrödinger equation of a system constisting of N interacting electrons in an external potential generated by M atomic nuclei is given by:

$$\widehat{H}\Psi(\mathbf{r}_1,...,\mathbf{r}_N) = E\Psi(\mathbf{r}_1,...,\mathbf{r}_N) \tag{1.1}$$

where $\Psi(\mathbf{r}_1,...,\mathbf{r}_N)$ represents the wave function of the N-electron many body system. The hamiltonian in eq. (1.1) is the sum of four operators:

$$\begin{aligned} \widehat{H} &= \widehat{T}_e + \widehat{V}_{ee} + \widehat{V}_{ei} + \widehat{T}_i + \widehat{V}_{ii} & (1.2) \\ &= \sum_{i=1}^{N}\left[-\frac{1}{2}\nabla_i^2 + \frac{1}{2}\sum_{i\neq j}\frac{1}{|\mathbf{r}_i - \mathbf{r}_j|}\right] - \sum_{\alpha=1}^{M}\frac{Z_\alpha}{|\mathbf{r}_i - \mathbf{R}_\alpha|} + \sum_{\alpha=1}^{M}\left[-\frac{1}{2}\nabla_\alpha^2 + \frac{1}{2}\sum_{\beta\neq\alpha}^{M}\frac{Z_\alpha Z_\beta}{R_{\alpha\beta}}\right] \end{aligned}$$

where we assumed atomi units $\hbar = m = e = a_0 = 1$. The terms in eq. (1.3) are associated to the kinetic energy and the Coulomb interaction of electrons (T_e and

V_{ee} respectively) and nuclei (T_i and V_{ii} respectively), and to the potential energy of the electrons in the field of the nuclei V_{ei}. $Z_{\alpha(\beta)}$ are the atomic numbers of the elements involved and $R_{\alpha\beta}$ are the nuclei distances.
Several approaches can be adopted in order to solve eq. (1.3).
First, the *pseudopotental approach* assumed in this thesis, simplifies the treatment of the problem reducing the number of the active electrons just to the valence ones and describing for each atom the joint effect of the nucleus and the core electrons with a suitable potential. For this reason in the following we will refer to ions instead of nuclei in the previous treatment.

Secondly, ions and electrons masses are extremely differents ($M_i >> m_e$) determining different time scale motions. Assuming that ions are allowed to move adiabatically in the field of the electrons ground state, the problem can be treated perturbatively within the Born Oppenheimer approximation. Hence, writing the wavefunction as:

$$\begin{aligned} \Psi(\{r\},\{R\}) &= \psi_{\{R\}}(\{r\})\phi(\{R\}) && (1.3)\\ \text{where } \{r\} &= \{\mathbf{r}_1,...,\mathbf{r}_N\} \\ \text{and } \{R\} &= \{\mathbf{R}_1,...,\mathbf{R}_M\} \end{aligned}$$

it is possible to decouple the hamiltonian separating the ionic and electronic part:

$$\begin{aligned} \left[T_e + V_{ee} + V_{ei}\right]\psi_{\{R\}}(\{r\}) &= E_e^n(\{R\})\psi_{\{R\}}(\{r\}) && (1.4)\\ \left[T_i + V_{ii} + E_e^n(\{R\})\right]\phi(\{R\}) &= E_{tot}\phi(\{R\}) && (1.5) \end{aligned}$$

where label i refers to ions and $E_e^n(\{R\})$ in eq. (1.4) represents the electronic contribution to the potential energy, i.e. the glue for the nuclei, in fact without this attractive term, the system would not be bonded. Conversely in eq. (1.5) ions contribute to the potential V_{ei} and are seen by the electrons as fixed point charges.

In conclusion, taking in account the approximations assumed, the Eq. 1.3 reduce to the eigenvalues problem of the operator:

$$H = -\sum_{i=1}^{N}\frac{1}{2}\nabla_i^2 + \sum_{i<j} v(\mathbf{r}_i,\mathbf{r}_j) - \sum_{i=1}^{N} v(\mathbf{r}_i) \qquad (1.6)$$

where the first term is the kinetic energy of electrons, the third is the external potential due to the ions in which the electons are immersed, the second term represents the complexity of the problem, it describes the interaction between electrons and prevents the decoupling of the equation in N one particle equations.

1.2 The variational formulation

If we consider a time–independent Hamiltonian, as described in the previous section, and we assume that periodic boundary conditions are applied, the spectrum of eigenvalues and eigenfunctions is discrete. For an arbitrary function Ψ with non vanishing norm, we can define the quantity:

$$E\left[\Psi\right] = \frac{\langle \Psi|\widehat{H}|\Psi\rangle}{\langle \Psi|\Psi\rangle} \tag{1.7}$$

It is then possible to prove that the Schrödinger equation $\widehat{H}|\Psi\rangle = E|\Psi\rangle$ is equivalent to the variational principle $\delta E\left[\Psi\right] = 0$.
In fact, taking the variation of eq. (1.7) we obtain:

$$\begin{aligned} \delta(E\left[\Psi\right]\langle\Psi|\Psi\rangle) &= \delta E\left[\Psi\right]\langle\Psi|\Psi\rangle + E\left[\Psi\right]\langle\delta\Psi|\Psi\rangle + E\left[\Psi\right]\langle\Psi|\delta\Psi\rangle \\ &= \langle\delta\Psi|\widehat{H}|\Psi\rangle + \langle\Psi|\widehat{H}|\delta\Psi\rangle. \end{aligned} \tag{1.8}$$

and considering that $\widehat{H}$ is hermitian we can conclude that:

$$\begin{aligned} \delta E\left[\Psi\right] = 0 \;\; &\Leftrightarrow \;\; \langle\delta\Psi|\widehat{H} - E|\Psi\rangle + \langle\Psi|\widehat{H} - E|\delta\Psi\rangle = 0 \\ &\Leftrightarrow \;\; \left(\widehat{H} - E\left[\Psi\right]\right)|\Psi\rangle = 0 \end{aligned} \tag{1.9}$$

The importance of the functional defined in eq. (1.7) can be seen expanding Ψ over the wavefunctions $\{\psi_n\}$:

$$\begin{aligned} \Psi = \sum_n c_n\psi_n \;\; &\Rightarrow \;\; E\left[\Psi\right] = \frac{\sum_n |c_n|^2 E_n}{\sum_n |c_n|^2} \\ &\Rightarrow \;\; E\left[\Psi\right] - E_0 = \frac{\sum_n |c_n|^2 (E_n - E_0)}{\sum_n |c_n|^2} \end{aligned} \tag{1.10}$$

where $E_0 = \min\{E_n\}$ is the ground state energy.
Hence we can conclude that:

$$E\left[\Psi\right] \geq E_0 \;\; ; \quad \Psi = \alpha\Psi_0 \;\Leftrightarrow\; E\left[\Psi\right] = E_0 \tag{1.11}$$

i.e. the ground state energy E_0 is implicitly defined by the minimization (1.11).

1.3 Density functional theory

Density Functional Theory (DFT) is a successful tool largely used in order to study ground state properties of condensed matter systems. Within this theory the problem of solving the Schrödinger equation for the ground state can be exactly recast into the variational problem of minimizing a functional with rispect to the charge density. The complexity of the problem is reduced in principle from having to deal with a function of 3N variable to one, the density, that depends only on the 3 spatial coordinates. In fact, the key quantity of the theory is the electronic density $\rho(\mathbf{r})$ that, respect to the many–body wavefunction $\Psi(\mathbf{r}_1, ..., \mathbf{r}_N)$, is a real quantity and has an intuitive physical interpretation. A review of the topic can be found in literature [1, 2, 3, 4], in this section we will review briefly the most important milestones.

1.3.1 Hohenberg-Kohn theorem

The essential role that is played by the charge density in the search for the electronic ground state was pointed out for the first time by Hohenberg and Kohn [2].
Let us consider a system of N interacting electrons immersed in an external potential V_{ext} with hamiltonian:

$$\widehat{H} = \widehat{H}_{\text{int}} + \widehat{V}_{\text{ext}} \tag{1.12}$$

in particular $H_{\text{int}} = T_e + V_{ee}$ and the external potential V_{ext} is due to the interaction, for example, between electrons and ions. Assuming that the ground state is not degenerate, the first part of the Hohenberg–Kohn theorem asserts that for every density $\rho(\mathbf{r})$ V-representable[1], the external potential V_{ext} is a functional of the charge density $V_{\text{ext}} = V_{\text{ext}}[\rho(\mathbf{r})]$, within an additive constant.

Let us assume, *ad absurdum*, that there exists a different potential V'_{ext} with a ground state Ψ' corresponding to the same ground state density $\rho(\mathbf{r})$. If E and E$'$ are the respective ground state energies we can write:

$$\begin{aligned} E < \langle\Psi'|\widehat{H}|\Psi'\rangle &= \langle\Psi'|\widehat{H}'|\Psi'\rangle + \langle\Psi'|\widehat{H} - \widehat{H}'|\Psi'\rangle \\ &= E' + \int \rho(\mathbf{r})[V_{\text{ext}}(\mathbf{r}) - V'_{\text{ext}}(\mathbf{r})]d\mathbf{r} \end{aligned} \tag{1.13}$$

A similar equation can be written in case of $\langle\Psi|\widehat{H}'|\Psi\rangle$, in fact:

$$\begin{aligned} E' < \langle\Psi|\widehat{H}'|\Psi\rangle &= \langle\Psi|\widehat{H}|\Psi\rangle + \langle\Psi|\widehat{H}' - \widehat{H}|\Psi\rangle \\ &= E - \int \rho(\mathbf{r})[V_{\text{ext}}(\mathbf{r}) - V'_{\text{ext}}(\mathbf{r})]d\mathbf{r} \end{aligned} \tag{1.14}$$

and now adding eq. (1.13) to eq. (1.14):

$$E + E' < E + E' \tag{1.15}$$

---

[1] A density is V-representable if it is positive defined, normalized to a number N, and such that there exists an external potential $V(\mathbf{r})$ for which there is a non-degenerate ground state corresponding to that density.

that is the *absurdum.*

Therefore, the theorem establishes the legitimacy of the charge density as the fundamental variable in the electronic problem, demonstrating a one-to-one correspondence between the density and the external potential $\rho = \rho[V_{ext}]$. Hence, this relation is invertible so the external potential can be viewed as a functional of the density $V_{ext} = V_{ext}[\rho]$.

Moreover, since the ground state energy is a function of the external potential $E_0 = E_0[V_{ext}]$, it is now possible to write it as a function of the charge density (HK functional):

$$E^{HK}[\rho(\mathbf{r})] = T[\rho(\mathbf{r})] + E_H[\rho(\mathbf{r})] + \int V_{\text{ext}}\rho(\mathbf{r})d\mathbf{r} \tag{1.16}$$

where $E_H[\rho(\mathbf{r})]$ is the Hartree energy given by:

$$E_H[\rho(\mathbf{r})] = \frac{1}{2}\int d\mathbf{r}\int d\mathbf{r}'\frac{\rho(\mathbf{r})\rho(\mathbf{r}')}{|\mathbf{r}-\mathbf{r}'|} \tag{1.17}$$

Once that the existance of the HK functional is established the second part of the theorem affirms that the minimum of the functional $E^{HK}[\rho(\mathbf{r})]$ is obtained when the charge density ρ is exactly the ground state density (*energy variational principle*).

In conclusion, the total energy of an N interacting particles system can be written as a functional of the density. This functional exists, is universal and non depending on the form of the external potential, however its analytical form is unknown.

1.3.2 The Kohn-Sham equations

The Hohenberg-Kohn theorem provides the theoretical justification to reformulate the search for the many–body ground state as a varational problem on the charge density. Although the analytical form of the HK functional is unknown, the minimization procedure lead to a set on N associated differential equations:

$$\begin{aligned} \delta E^{HK}[\rho] &= \delta\left[T[\rho] + V_H[\rho] + \int V_{ext}\rho(\mathbf{r})d\mathbf{r} - \lambda\left(\int \rho(\mathbf{r})d\mathbf{r} - N\right)\right] = 0 \\ \frac{\delta T[\rho]}{\delta\rho(\mathbf{r})} &+ \frac{\delta V_H[\rho]}{\delta\rho(\mathbf{r})} + V_{ext} = \lambda \end{aligned} \tag{1.18}$$

where V_H is the Hatree potential and λ are Lagrange multipliers required by the normalization constraint.

The Kohn and Sham approach is based on the introduction of an auxiliary non interacting system of N electrons, having the same density of the real interacting system in a suitable external potential.

We can write the ground state density of the interacting system expanded on a basis of N independent orthonormals orbitals:

$$\rho(\mathbf{r}) = \sum_i f_i \phi_i^*(\mathbf{r}) \phi_i(\mathbf{r}) \tag{1.19}$$

where f_i represents the occupation factor of the orbital i.
Hence, the HK functional can be written in terms of the kinetic energy of the non interacting system:

$$E^{HK}_{V_{ext}}[\rho] = T_0 + E_H[\rho] + \int V_{ext} \rho(\mathbf{r}) d\mathbf{r} + E_{xc}[\rho] \tag{1.20}$$

where T_0 is the kinetic energy of the non–interacting system:

$$T_0[\rho] \;\; = \;\; T_0[\phi_i] = \sum_i \int \phi_i^*(\mathbf{r}) \left[-\frac{\nabla^2}{2} \phi_i(\mathbf{r}) \right] d\mathbf{r} \tag{1.21}$$

E_H is the Hartree energy and E_{xc} is the only unknown term:

$$E_{xc}[\rho] \;\; = \;\; E - T_0 - E_{\mathrm{H}} - V_{\mathrm{ext}}. \tag{1.22}$$

In particular, the E_{xc} term contains the contributions given by the difference in the kinetic energy of the interacting and non interacting system, i.e. $\Delta T[\rho] = T[\rho] - T_0[\rho]$, the exchange effects (Fermi correlation) and the correlation effects (Coulomb correlation).

Now, we can calculate the minimum of the HK functional (1.20) for the KS non interacting system in a fixed external potential V_{ext} and with the N×N constraints due to the orthonormality of the orbitals:

$$\frac{\delta}{\delta \phi^*} \left[E - \sum_{n,m} \lambda^N_{m,n} \left(\int \phi^*_m \phi_n - \delta_{m,n} \right) \right] = 0 \tag{1.23}$$

where:

$$\frac{\delta}{\delta \phi_i^*} = \frac{\delta \rho}{\delta \phi_i^*} \frac{\delta}{\delta \rho} = \phi_i \frac{\delta}{\delta \rho} \tag{1.24}$$

From eq. (1.23) we can obtain the following set of equations:

$$\left[-\frac{1}{2} \nabla^2 + V^{\mathrm{eff}}_{\mathrm{DFT}} \right] \phi_i = \lambda_i \phi_i \tag{1.25}$$

where $H^{\mathrm{KS}} = -\frac{1}{2}\nabla^2 + V^{\mathrm{eff}}_{\mathrm{DFT}}$ is the Kohn-Sham Hamiltonian and $V^{\mathrm{eff}}_{\mathrm{DFT}}$ is the sum of three contributions:

$$V^{\mathrm{eff}}_{\mathrm{DFT}} = V_{\mathrm{H}} + V_{\mathrm{ext}} + V_{\mathrm{xc}} \tag{1.26}$$

the Hartree potential V_{H}, the external potential V_{ext} and the exchange-correlation potential given by:

$$V_{\mathrm{xc}} = \frac{\delta E_{xc}[\rho]}{\delta \rho(\mathbf{r})} \tag{1.27}$$

Now, if we rewrite the density eq. (1.19) expanded over the N occupied orbitals:

$$\rho(\mathbf{r}) = \sum_{i}^{N} |\phi_i(\mathbf{r})|^2 \tag{1.28}$$

we must solve the set of N one particle equations. Now, if we assume that $\{\phi_i\}$ diagonalize the N×N hermitian matrix H^{KS}:

$$\lambda_{mn} = \langle \phi_m | H^{KS} | \phi_n \rangle \tag{1.29}$$

we can write N one-particle equations:

$$\left\{ -\frac{\nabla^2}{2} + V_{\mathrm{ext}}(\mathbf{r}) + \int \frac{\rho(\mathbf{r}')}{|\mathbf{r}-\mathbf{r}'|} d\mathbf{r}' + V_{\mathrm{xc}}(\mathbf{r}) \right\} \phi_i(\mathbf{r}) = \lambda_i \phi_i(\mathbf{r}) \tag{1.30}$$

where λ_i are now interpreted as the KS energies ϵ_i^{KS}.
Since the last two terms of the hamiltonian depend on the eigenvectors throught eq. (1.28), the eigenvalues and eigenvectors can be determined self consistently.
The equations (1.28) and (1.30) are called *Kohn and Sham equations* and provide a procedure to calculate the total ground–state energy of the system:

$$E = E_{V_{\mathrm{ext}}}[\rho_0] = \sum_{i=1}^{N} \epsilon_i^{KS} - E_H[\rho_0] + E_{xc}[\rho_0] - \int \rho_0(\mathbf{r}) V_{\mathrm{xc}}(\mathbf{r}) d\mathbf{r} \tag{1.31}$$

In conclusion it is worth mentioning that the KS eigenvalues do not have any physical meaning, as, for instance, Hartree–Fock eigenvalues that are related to real orbital energies via the Koopmans theorem. However, there exists a number of approximations of the exchange-correlation potential (see sections 1.4.1, 1.4.2 and 1.4.3) providing good agreements with experimental results in many applications. This justifies the practical usefullness of the KS scheme.

1.4 Methods

1.4.1 Local density approximation

Once the Kohn-Sham scheme is defined there still exists the problem of the missing analytical representation of the exchange–correlation energy.

A commonly used approximation is offered by the Local Density Approximation (LDA) [5], which makes DFT practically applicable to a wide variety of systems and provides a correct description of systems in which the density varies slowly in space. The form of E_{xc} is given by:

$$E_{xc}^{LDA}[\rho(\mathbf{r})] = \int \epsilon_{xc}^{heg}(\rho(\mathbf{r}))\rho(\mathbf{r})d\mathbf{r} \tag{1.32}$$

where the local dependence of E_{xc} on the density $\epsilon_{xc}^{heg}(\rho(\mathbf{r}))$ is given in terms of the exchange–correlation energy of the homogeneous electron gas of constant density $\rho = \rho(\mathbf{r})$. Hence the systems is locally approximated to an homogeneous electrons system. The function ϵ_{xc}^{heg} can be separated in an exchange part:

$$\epsilon_x(\rho) = -\frac{3}{4}\left(\frac{3}{\pi}\right)^{1/3}\rho^{1/3} \tag{1.33}$$

and a correlation term $\epsilon_c(\rho)$, a function that can be obtained by Quantum Monte Carlo simulations (QMC), the most popular form has been given for different densities by Ceperley and Adler [6].

Moreover the exchange–correlation potential can be written as:

$$\begin{aligned} V_{xc}^{LDA}(\mathbf{r}) &= \frac{\delta E_{xc}^{LDA}}{\delta n(\mathbf{r})} \\ &= \epsilon_{xc}(\rho(\mathbf{r})) + \rho(\mathbf{r})\frac{d\epsilon_{xc}}{d\rho} \end{aligned} \tag{1.34}$$

The domain of applicability of the LDA has proved to be valid for a large amount of systems, even not homogeneous ones. However, its results are not appropriate for the case of few electron systems (see chapter 6). For localized systems self–interaction corrections (SIC [7]) are usually used.

1.4.2 Local spin density approximation

The Local Spin Density Approximation (LSDA) provides a generalization of the LDA to the case of spin polarized calculations. Let us define the spin polarization parameter ζ:

$$\zeta = \frac{\rho_\uparrow - \rho_\downarrow}{\rho_\uparrow + \rho_\downarrow} \qquad 0 \le \zeta \le 1 \tag{1.35}$$

In the limiting case where $\zeta = 0$, $\rho_\uparrow = \rho_\downarrow$ and we will recover the LDA for unpolarized systems (U), conversely, if $\zeta = 1$ the system is completely spin polarized (P) and it is possible to write the following parametrizations (see Ref. [7]):

$$\epsilon_x^P(\rho) = 2^{1/3}\epsilon_x^U(\rho) \tag{1.36}$$

$$\epsilon_c^P(\rho) = \frac{1}{2}\epsilon_c^U(2^{4/9}\rho) \tag{1.37}$$

for the exchange and correlation part, respectively. In the intermediate cases the parametrization for ϵ_{xc} is given by:

$$\epsilon_{xc}(\rho) = \epsilon^U_{xc}(\rho) + f(\zeta)\left[\epsilon^P_{xc}(\rho) - \epsilon^U_{xc}(\rho)\right] \tag{1.38}$$

where the smooth interpolation function $f(\zeta)$ is defined by:

$$f(\zeta) = \frac{(1+\zeta)^{4/3} + (1-\zeta)^{4/3} - 2}{2^{4/3} - 2} \tag{1.39}$$

1.4.3 Generalized gradient approximation

A natural way to improve the LDA in order to account for the inhomogeneities of the density is to make a gradient expansion of the exchange-correlation energy with respect to the density. In this way ϵ_{xc} results to be dependent on the local derivative of the density:

$$E^{GGA}_{xc}[\rho_\uparrow, \rho_\downarrow] = \int f(\rho_\uparrow, \rho_\downarrow, \nabla\rho_\uparrow, \nabla\rho_\downarrow) d\mathbf{r} \tag{1.40}$$

This is the so called Generalized Gradient Approximation (GGA), often used in terms of the Perdew-Burke-Ernzerhof (PBE) [8, 9] parametrization.
The GGA improves the LDA with respect to some applications (molecules or systems with strongly inhomogeneous density distribution) but it does not offer a systematic advance in the DFT calculation tools.

1.4.4 Brief review of pseudopotential method

Pseudopotential approach treats an all-electron variational calculation of ground state properties in terms of the only valence wavefunctions immersed in a modified potential. In this way, core states, being the most localized and expensives to be represented, are not directly included in the calculations: their effect on valence electrons is described by a suitable *pseudo*potential. A review of the topic can be found in the literature, ranging from the most influential works [10, 11, 12, 13, 14, 15, 16, 17] to other important but less fundamental ones [18, 19, 20, 21].
In the following we briefly summarize the most important steps of the method. All-electron valence orbitals can be represented as a linear combination of core orbitals $|\psi_c\rangle$ and a smooth function $|\phi^P_v\rangle$:

$$|\psi_v\rangle = |\phi^P_v\rangle + \sum_c \alpha_{cv} |\psi_c\rangle \tag{1.41}$$

where $\alpha_{cv} = \langle\psi_{c'}|\phi^P_v\rangle$ are coefficients that guarantee the core-valence orthogonality. By inverting eq. (1.41) with respect to $|\phi^P_v\rangle$, it is possible to write valence pseudo wavefunction in terms of all-electron core and valence states. Then, applying the Hamiltonian to $|\phi_v^P\rangle$ it is possible to show that they are eigenstates of a modified hamiltonian with the same eigenstates of the all-electron wavefunctions:

$$\left[\widehat{H} + \sum_c (\epsilon_v - \epsilon_c)|\psi_c\rangle\langle\psi_c|)\right] |\phi_v^P\rangle = \epsilon_v |\phi_v^P\rangle \tag{1.42}$$

The projector defined in eq. (1.42) by $\widehat{\mathcal{P}} = \sum_c (\epsilon_v - \epsilon_c)|\psi_c\rangle\langle\psi_c|$ is not local. Moreover, because $\langle\phi_v|\widehat{\mathcal{P}}|\phi_v\rangle$ is positive defined it represents a repulsive and short range potential, as it should be to correctly describe core orbitals.

In the general scheme, norm conserving pseudopotentials are derived from an atomic reference state requiring that *pseudo* and all-electron valence eigenstates have the same energies and density outside a chosen core cutoff radius. Normalization of the pseudo orbitals guarantees that they include the same amount of charge in the core region. Futhermore *pseudo* and all-electron logarithmic derivatives agree, at the reference energies, beyond the cutoff radius. Finally, norm conservation ensures that the *pseudo* and all-electron logarithmic derivatives agree also around each reference level to first order in the energy.

In this way a pseudopotential exhibits the same scattering properties as an all–electron potential in a neighboorhood of the atomic eigenvalues [22]. This property provides a measure of the transferability of the pseudopotential.

1.5 Time dependent density functional theory

Density functional theory is a successful tool for a large range of applications, however some limits can be underlined.
First, DFT is a ground state theory and it is not obvious how to generalize the KS eigenvalues in order to represent the quasi particle energies[2]. Secondly, DFT is a theory dealing with stationary states, hence it is not possible to apply it to the case of time–dependent hamiltonians.

Part of those limits are overcomed by the Time Dependent Density Functional Theory (TDDFT) that is an exact reformulation of time dependent quantum mechanics where the fundamental variable is the time–dependent electronic density $\rho(\mathbf{r}, t)$ instead of the many–body function of the system. The first milestone is the Runge–Gross theorem [23] that provide a generalization of the Hohenberg–Kohn theorem to time dependent densities. The theorem states that there exists a one–to–one correspondence between the time dependent external potential $W(t)$ and the time dependent density of an evolving system at a fixed initial state:

---

[2] For instance, the direct interpretation of the KS eigenvalues as the quasiparticle energies of the system leads to the understimation of the bandgap of semiconductors.

$$W(t) \leftrightarrow \rho(\mathbf{r}, t) \tag{1.43}$$

If we consider the Hamiltonian describing an N-electrons system given by:

$$\widehat{H}(t) = \widehat{T} + \widehat{V} + \widehat{W}(t) \tag{1.44}$$

where, beyond the kinetic and the coulombian term (T and V respectively), a time–dependent external potential $W(t) = \sum_i V_{\text{ext}}(\mathbf{r}, t)$ appears that can be expandend around an initial time t_0 such as $V_{\text{ext}}(\mathbf{r}, t_0) = V_{\text{ext}}(\mathbf{r})$.
The time evolution of the system is described by the Schrödinger equation:

$$H(t)\psi(t) = i\frac{\partial}{\partial t}\psi(t) \tag{1.45}$$

Two time dependent densities $\rho(\mathbf{r}, t)$ and $\rho'(\mathbf{r}, t)$, having a commun initial state $\psi(t_0) = \psi_0$ and influenced by two different external potentials V_{ext} and V'_{ext}, expandable around t_0 and such as $V'_{\text{ext}} \neq V_{\text{ext}} + c(t)$, are always different. Hence $\rho(\mathbf{r}, t)$ determines the external potential but for a time dependent function $c(t)$. Conversely the potential fixes the density but for a time dependent phase:

$$\psi(t) = e^{-i\alpha(t)}\psi\left[\rho, \psi_0\right](t) \tag{1.46}$$

Hence, for every time–dependent observable $\widehat{O}(t)$ that is not depending on time derivative or time integral, is a functional of the density:

$$\langle\psi(t)|\widehat{O}(t)|\psi(t)\rangle = O\left[\rho\right](t) \tag{1.47}$$

From the Runge–Kohn theorem it is straightforward to build the Kohn–Sham scheme for the time dependent case (see Refs. [24] and [25]). We can write the action:

$$A[\psi] = \int_{t_0}^{t_1} dt\langle\psi(t)|i\frac{\partial}{\partial t} - \widehat{H}(t)|\psi(t)\rangle \tag{1.48}$$

where ψ is the many–body wavefunction with initial condition $\psi(t_0) = \psi_0$. The time–dependent Schrödinger equation corresponds to a stationary point of $A[\psi]$ similarly to classical mechanics, where the trajectory is a stationary point of the action $A = \int_{t_0}^{t_1} L(t)dt$ with L the Lagrangian of the system. The action in eq. (1.51) is a functional of the density and has a stationary point corresponding to the correct $\rho(\mathbf{r},t)$, i.e. solving the Euler equations:

$$\frac{\delta A[\rho]}{\delta\rho(\mathbf{r},t)} = 0 \tag{1.49}$$

it is possible to recover the density.
Similarly to the static case, we can write:

$$A[\rho] = B[\rho] - \int_{t_0}^{t_1} dt \int d\mathbf{r}\rho(\mathbf{r},t)V_{ext}(\mathbf{r},t) \tag{1.50}$$

where B is a universal functional given by:

$$B[\rho] = \int_{t_0}^{t_1} dt\langle\psi(t)|i\frac{\partial}{\partial t} - \widehat{T} - \widehat{V}|\psi(t)\rangle \tag{1.51}$$

Now, an auxiliary non interacting system can be associated to the interacting one in a similar way than to the Kohn–Sham scheme. The stationary condition can be applied to eq. (1.50) with the condition $\rho(\mathbf{r},t) = \sum_i |\phi_i(\mathbf{r},t)|^2$ in order to obtain the time dependent KS equations:

$$\left[-\frac{1}{2}\nabla^2 + V_{ext}(\mathbf{r},t) + \int V(\mathbf{r},\mathbf{r}')\rho(\mathbf{r}',t)d\mathbf{r}' + V_{xc}(\mathbf{r},t)\right]\phi_i(\mathbf{r},t) = i\frac{\partial}{\partial t}\phi_i(\mathbf{r},t) \tag{1.52}$$

In eq. (1.52) it is possible to recognize three contributions to the effective potential:

$$V_{\text{eff}}(\mathbf{r},t) = V_{\text{H}}(\mathbf{r},t) + V_{\text{ext}}(\mathbf{r},t) + V_{\text{xc}}(\mathbf{r},t) \tag{1.53}$$

the Hartree and the external potential (V_{H} and V_{ext} respectively) and the exchange–correlation potential defined by the functional derivative:

$$V_{\text{xc}}(\mathbf{r},t) = \frac{\delta A_{\text{xc}}}{\delta\rho(\mathbf{r},t)} \tag{1.54}$$

where A_{xc} is the exchange–correlation part of the action (1.51).

1.6 Linear response

Within the TDDFT framework we can calculate the linear response of an N particle system to an external time dependent perturbation. The response will be related the excited states of the system and can be defined as the variation of the density with respect to the variation of the time dependent external potential causing the perturbation:

$$\chi(\mathbf{r},t,\mathbf{r}',t') = \frac{\delta\rho(\mathbf{r},t)}{\delta V_{\text{ext}}(\mathbf{r}',t')}|_{V_{\text{ext}=0}} \tag{1.55}$$

Similarly, the linear response in the case of the auxiliary non interacting KS system can be expressed by:

$$\chi^0(\mathbf{r},t,\mathbf{r}',t') = \frac{\delta\rho(\mathbf{r},t)}{\delta V_{\text{eff}}(\mathbf{r}',t')}|_{V_{\text{eff}}=0} \tag{1.56}$$

where the functional derivatives are calculated at the first order in V_{ext} in eq. (1.55) and in V_{eff} in eq. (1.56).

Now, using the following relation:

$$\frac{\delta\rho}{\delta V_{\text{ext}}} = \frac{\delta\rho}{\delta V_{\text{eff}}}\frac{\delta V_{\text{eff}}}{\delta V_{\text{ext}}} = \chi^0\frac{\delta V_{\text{eff}}}{\delta V_{\text{ext}}} \tag{1.57}$$

we can write:

$$\frac{\delta V_{\text{eff}}(\mathbf{r},t)}{\delta V_{\text{ext}}(\mathbf{r}',t')} = \delta(\mathbf{r}-\mathbf{r}')\delta(t-t') + \int\left[\frac{\delta(t-t'')}{|\mathbf{r}-\mathbf{r}''|} + f_{xc}(\mathbf{r},t,\mathbf{r}'',t'')\right]\chi(\mathbf{r}'',t'',r',t')d\mathbf{r}''dt'' \tag{1.58}$$

where:

$$f_{xc}(\mathbf{r},t,\mathbf{r}',t') = \frac{\delta V_{xc}[\rho(\mathbf{r},t)]}{\rho(\mathbf{r}',t')}|_{V_{\text{ext}}=0} \tag{1.59}$$

is the exchange–correlation kernel, the quantity that contains the core of the complexity of the problem. Combining eq. (1.57) and (1.58) it is possible to write a Dyson equation for χ and χ^0:

$$\chi(\mathbf{r},\mathbf{r}',\omega) = \chi^0(\mathbf{r},\mathbf{r}',\omega) + \int d\mathbf{r}_1 d\mathbf{r}_2 \chi^0(\mathbf{r},\mathbf{r}_1,\omega)\left[\frac{1}{|\mathbf{r}_1-\mathbf{r}_2|} + f_{xc}(\mathbf{r}_1,\mathbf{r}_2,\omega)\right]\chi(\mathbf{r}_2,\mathbf{r}',\omega) \tag{1.60}$$

The analytical form of the exchange–correlation kernel is unknown, for this reason, the solution of this integral equation is not trivial.

In the case of $f_{xc} = 0$ the approximation is called the independent particle random phase approximation (IP-RPA) that is equivalent to the Hartree theory but with the addition of time dependency. In this scheme the density fluctuation at the first order is written as:

$$\rho(\omega) = \int \chi^0(\mathbf{r},\mathbf{r}',\omega)V_{\text{eff}}(\mathbf{r}',\omega)d\mathbf{r}' = \int \chi(\mathbf{r},\mathbf{r}',\omega)V_{\text{ext}}(\mathbf{r}',\omega)d\mathbf{r}' \tag{1.61}$$

where χ^0 is built using the KS eigenvalues and eigenvectors calculated with an approximation for the exchange–correlation potential V_{xc} in the KS hamiltonian.

The problem of the efficient evaluation of the response function will be discussed extensively in chapter 3, where a new method for the calculation of $\chi^{(0)}$ will be also presented. For this reason, we postpone to that chapter the details on the analytical form of this quantity.

1.6.1 Adiabatic (spin) local density approximation

The adiabatic local density approximation (ALDA) furnishes a way to compute the excitation energies of a system within the TDDFT. Within this approximation the exchange–correlation potential defined in eq. (1.54) is written as:

$$V_{xc}(\mathbf{r},t) \simeq \frac{\delta E_{xc}[\rho]}{\delta \rho_t(\mathbf{r})} \tag{1.62}$$

where the functional derivative is taken respect to the instantaneous density in such a way that the exchange–correlation energy depends just on the density at a fixed time[3]. By consequence, the exchange–correlation kernel becomes:

$$f_{xc}(\mathbf{r},t,\mathbf{r}',t') = \frac{\delta V_{xc}(\mathbf{r},t)}{\delta \rho(\mathbf{r}',t')} \simeq \delta(t-t')\frac{\delta V_{xc}(\mathbf{r},t)}{\delta \rho(\mathbf{r}',t')} \tag{1.63}$$

and using local density approximation, see eq. (1.34), we can also write:

$$f_{xc}^{ALDA}(\mathbf{r},t,\mathbf{r}',t') = \delta(t-t')\delta(\mathbf{r}-\mathbf{r}')\left(2\frac{d\epsilon_{xc}^{heg}(\rho)}{d\rho} + \rho\frac{d^2\epsilon_{xc}^{heg}(\rho)}{d^2\rho}\right) \tag{1.64}$$

Moreover, if we want to include the spin variable (ALSDA) we obtain the following expression:

$$\begin{aligned} f_{xc}^{ALDA}(\mathbf{r},t,\mathbf{r}',t') &= \delta(t-t')\delta(\mathbf{r}-\mathbf{r}') \qquad (1.65) \\ &\left(\frac{d\epsilon_{xc}^{LSDA}(\rho,\zeta)}{d\rho_\uparrow} + \frac{d\epsilon_{xc}^{LSDA}(\rho,\zeta)}{d\rho_\downarrow} + \rho\frac{d^2\epsilon_{xc}^{LSDA}(\rho,\zeta)}{d\rho_\uparrow d\rho_\downarrow}\right) \end{aligned}$$

where the derivation is defined as:

$$\begin{aligned} \frac{d\epsilon(\rho,\zeta)}{d\rho_\uparrow} &= \frac{\partial\epsilon(\rho,\zeta)}{\partial\rho} + \frac{\partial\epsilon(\rho,\zeta)}{\partial\zeta} \\ \frac{d\epsilon(\rho,\zeta)}{d\rho_\downarrow} &= \frac{\partial\epsilon(\rho,\zeta)}{\partial\rho} - \frac{\partial\epsilon(\rho,\zeta)}{\partial\zeta} \end{aligned}$$

1.7 Dielectric function

The key quantity connecting the theories presented in the previous sections and the experimental spectra is the dynamical dielectric function $\varepsilon(\mathbf{r},\mathbf{r}',\omega)$. When an external perturbing field is applied to the sample, the charge density rearrages and an additional potential V_{ind} is induced by the polarization of the system. The total potential, or *screened* potential, is due to the contribution of the external and the induced potential:

---

[3] For this reason, in adiabatic LDA memory effects are neglected.

$$V_{tot} = V_{ext} + V_{ind} \tag{1.66}$$

and it can be also written in terms of the dielectric function:

$$V_{tot} = \int \varepsilon^{-1}(\mathbf{r}, \mathbf{r}')V_{\text{ext}}(\mathbf{r}')d\mathbf{r}' \tag{1.67}$$

The dynamical dielectric function can be recovered as:

$$\varepsilon(\mathbf{r}, \mathbf{r}', \omega) = \delta(\mathbf{r} - \mathbf{r}') - \int d\mathbf{r}''v(\mathbf{r} - \mathbf{r}')\chi(\mathbf{r}'', \mathbf{r}', \omega) \tag{1.68}$$

where $v(\mathbf{r} - \mathbf{r}')$ is the bare coulomb interaction. The dynamical dielectric function $\varepsilon(\omega)$ takes in account the rearrangement of the charge density presenting hole and charge accumulation due to the perturbation. However, the screened potential usually is calculated from the external potential inducing the polarizabilty of the system (see eq. (1.67)). Hence, the important microscopic quantity is the inverse of the dielectric function that can be written as:

$$\varepsilon^{-1}(\mathbf{r}, \mathbf{r}', \omega) = \delta(\mathbf{r} - \mathbf{r}') + \int d\mathbf{r}''v(\mathbf{r} - \mathbf{r}'')\chi(\mathbf{r}'', \mathbf{r}', \omega) \tag{1.69}$$

In conclusion, the response function χ and the dynamical dielectric function $\epsilon(\mathbf{r}, \mathbf{r}', \omega)$ represent the key ingredients for theoretical spectroscopy. In the next chapter we will present the connections between ϵ and the three class of experimental spectroscopies considered in the present thesis: energy loss, reflectivity and absorption spectra.

Chapter 2

Surface spectroscopies

Every real solid is surrounded by surfaces. Moreover the miniaturization of the technological devices requires a better understanding of mechanisms at the atomistic scale at which surface effects become important[1].
From the experimental point of view, surface atoms are only visible in sensitive techniques or by studying processes involving atoms at the surface (crystal growth, adsorption, oxidation, etching, ...).
Under normal conditions (atmospheric pressure and room temperature) a real surface of a solid is different from an ideal truncated bulk because of a reordering of the surface atomic bonds and because prepared surfaces are normally very reactive to atoms and molecules in the environment. From chemisorption to physisorption, all kinds of particle adsorption gives rise to an adlayer on the topmost atomic layers of the solid.

Because of this complexity, first principles calculations can be very helpful to better understand the physics of such a system. In this section we will briefly review the significant experiments and the theoretical tools devoted to describe surface physics.

2.1 Experimental issues

Spectroscopy is a useful tool to get information about the physical nature or geometrical reconstruction of surfaces. Many high level experimental technologies has been developed in the last decades in order to create and analyse the surfaces of materials, an exhaustive review of the topic can be found in the literature [26, 27, 28]. Here we summarize the highlights to introduce our results presented in the followings chapters.

---

[1] In effect if we look at the number of surface atoms ($N_A(S)$) with respect to the bulk ($N_A(B)$) in a 1 cm^3 volume cube we can say that surface effects are negligible because: $\frac{N_A(S)}{N_A(V)} = \frac{10^{15}}{10^{23}} = 10^{-8}$. On the contrary in the case of a 100 Å length cube we write: $\frac{N_A(S)}{N_A(V)} = \frac{10^4}{10^6} = 10^{-2}$, hence the surface signals are not negligible anymore.

2.1.1 Preparation and structural properties

In order to get spectroscopic information, a well defined surface has to be prepared on a particular solid, using a special preparation process and under well defined external conditions.

There are several ways to prepare a surface from a crystalline material and they can be grouped into three categories: (i) *cleavage* (limitated to cleavage planes), (ii) treatment of imperfect and contaminated surfaces by *ion bombardment and thermal annealing* and (iii) *epitaxial growth* of a crystal layer by means of evaporation or molecular beam epitaxy (MBA). In all cases Ultra High Vacuum (UHV), i.e pressure conditions lower than 10^{-8}Pa (10^{-10} torr) are required.

However, despite the great care in preparing surfaces, irregular deviations from perfect smoothness and purity are always present (steps, terraces or in general *surface roughness*) making real surfaces far from the ideal ones.

Surface atoms rearrange with respect to the bulk crystal positions because forces acting on the on top atoms differ from interactions between atoms inside the volume, and as a results this difference can be enhanced depending on the bounding behaviour of the material.

However, the deviation of atom positions from that of an infinite crystal decreases with increasing distance from the surface.

Hence in our theoretical models we will assume with confidence that positions of atoms deep inside the bulk are the same as those in an infinite crystal. On the contrary, the distortions of the atomic configuration due to the termination of the crystal, are important close to the surface.

In the case of silicon, the main element considered in this work, when a surface is created tetrahedral bonds are broken, and a non negligible atomic rearrangement is expected to destroy the translational symmetry of an ideal bulk truncated surface. Moreover dangling bonds are usually unstable because rebonding lowers the total energy pushing surface atoms closer to form pairs (dimers). For this reason we can expect that a silicon surface is a good example of a *reconstruction* process.

On the contrary, in the case of materials where chemical bonds are less directional (as the case of metals), surfaces are created by *relaxation* of the topmost layers along the direction perpendicular to the surface plane. In this case the changes may conserve the translational-symmetry of the bulk.

The main experimental techniques used in the study of surface structure exploit the diffraction of neutral atomic beams or electrons. With Low-Energy Electron Diffraction (LEED) the surface periodicity and a reconstruction are observed directly via the diffraction pattern, which give an image of the reciprocal lattice. The size and shape of the spots contain information about the extention of domains and the presence of surface defects. The atomic positions inside the unit cell and the relaxation can be studied through the intensity profiles of the diffracted beam, i.e., by plotting the measured intensity of each diffraction spot as a function of the energy of the incoming electron. The information of the atomic position is obtained by comparing the experimental LEED profiles with those obtained by a theoretical simulation of the electron diffraction in the crystal, where the atomic positions are the input data. An example of LEED patterns is reported in Fig. 2.1.
Reflection High Energy Electron Diffraction (RHEED) is also used, principally to monitor the thin film growth. In this technique incident energies of $10-100$keV and incident angles of about $3-5$ degrees are used.

The structural analysis of LEED is often performed togheter with Auger Electron Spectroscopy (AES) to control the chemical composition of the sample. In AES a beam of electrons with energies beyond 1keV strikes the surface and the number of electron backscattered N(E) is analysed as a function of the energy. The $\frac{dN}{dE}$ gives the signature of the elements present in the sample.

Moreover we mention the light-ion Rutherford backscattering (RBS), where beams of H^+ or He^{2+} ions are used with energies of hundreds of keV (LEIS up to 20 keV, MEIS from 20 eV to 200 keV and HEIS to 2 MeV). The ions are scattered by the nuclei of the crystal following the dynamics of classical Rutherford scattering and lose energy along straight trajectories through interaction with the electrons. Information on the composition and atomic displacements in the surface layers can be obtained thanks to this method detecting the number of ions as a function of the energy and the outcoming directions of ions diffused backward.

Another important technique employed to investigate the structural properties of semiconductors is Scanning Tunnel Microscopy (STM). Due to Binnig and Rohrer (1982), this technique gives the local density of occupied and empty states integrated over a given energy range around the Fermi level. This technique does not need UHV. An example of STM image is reported in Fig. 2.1.

From all these techniques we can get structural information about the system

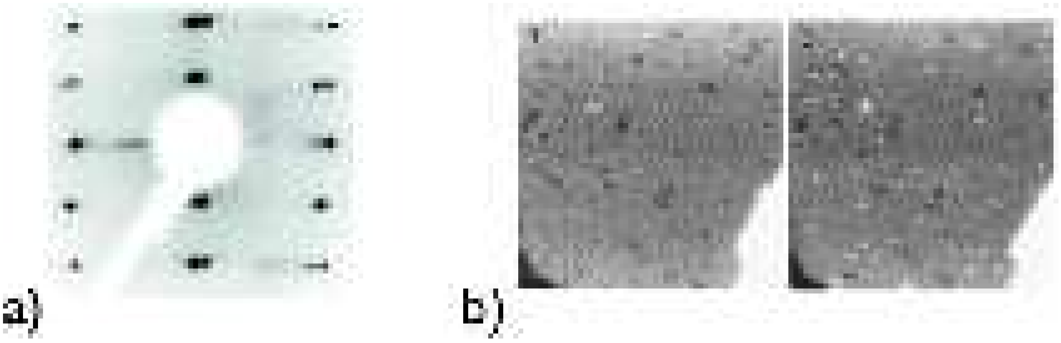

Figure 2.1: Examples of experimental images obtained by LEED (left) for a vicinal surface, explaining the double spots in the image, and STM (right). In particular in a) LEED patterns of a Si(001)-(1×2) are reproduced from [31] in b) an STM image of the Si(100)-(2×1) surface at 61K, filled (a) and empty (b) states, from [32].

but a comprehensive interpretation of the data must usually be supported by a theoretical description which involves the knowledge of the electronic structure [29, 30].

2.1.2 Electronic properties

In translationally invariant systems the wave vector $\mathbf{k}$ defines a set of good quantum numbers for each type of elementary excitation. In the case of an ordered surface of a crystal, such a wavevector $\bar{\mathbf{k}}$, is restricted to two dimensions (parallel to the surface) because in the third direction the system is not translationally invariant anymore. The Surface Brillouin Zone (SBZ) becomes 2 dimensional and is defined as the smallest polygon in the 2D reciprocal space situated symmetrically with respect to a given lattice point (the origin) and bounded by points $\bar{\mathbf{k}}$, satisfying the equation:

$$\bar{\mathbf{k}}\cdot\mathbf{g} = \frac{1}{2}|\mathbf{g}|^2 \tag{2.1}$$

where $\mathbf{g}$ is a surface reciprocal lattice vector. Figure 2.2 represents three of the five SBZ, referring to the ones we considered in the next chapters of this thesis: p-rectangular, c-rectangular and square. Further details on surface theory can be found in [28]. Among the experimental techniques which allow to inspect directly the band structure and the electronic structure in the 2 dimensional BZ we mention the most fundamental: Photoemission (PES), Angle–Resolved Photoemission (ARPES) and Inverse Photoemission (IPES).

PES is the most important technique able to give a picture of the Density of

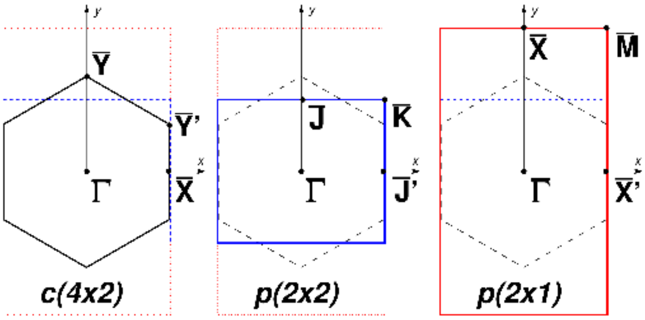

Figure 2.2: Surface Brillouin Zone for the three surface reconstructions that we considered in the present thesis: a c-rectangular, a p-square and a p-rectangular.

States (DOS) at the upper atomic planes. The physics behind the PES technique is an application of Einstein's photoelectric effect. The sample is exposed to a beam of light inducing photoelectric ionization; synchrotron radiation is the ideal isochromatic radiation source. The energies of the emitted photoelectrons are characteristic of their original electronic states. For solids, photoelectrons can escape only from a depth of the order of nanometers, so that it is the surface layer which is mostly analyzed. PES can be performed with X-ray (XES), E≃20–150 eV, where it is possible to see transitions between surface bands below the edge of the bulk bandgap (the small cross section can be improved using grazing angles) [27].

ARPES gives information about the k-dispersion of bands and allows to separate the contributions from bulk and surface states. The former connect states with the same 3D **k**-vector, the latter involve photoemission processes conserving only the component parallel to the surface $\mathbf{k}_{||}$. The detected 2D vector connecting surface states and the continuum can be written as:

$$k_{||}^{out} = k_{||}^{in} + \mathbf{g} \qquad \forall k_{\perp} \tag{2.2}$$

where **g** is a vector of the surface reciprocal lattice. Hence, plotting the electron energy as a function of the emission angle θ by:

$$\begin{aligned} E_{kin} &= \frac{\hbar^2}{2m}(k_{||}^2 + k_{\perp}^2) \\ k_{||}(\theta) &= k_{||}\sin\theta = \frac{\sqrt{2mE_{||}}}{\hbar}\sin\theta \end{aligned} \tag{2.3}$$

we can say that the peaks in the energy distribution curve represent the initial state of the solid labelled by $k_{||}$.

Inverse photoemission (IPES) allows to detect the energy of the photon emitted when an electron of an external beam of given E and **k** falls into an empty conduction surface band or an image state. Even optical adsorption is a useful method to study the occupied and unoccupied states that in a first approximation can be described by the Joint Density of States (JDOS) defined by:

$$JDOS(\omega) = \int \rho(E)\theta(E_F - E)\rho(E - \hbar\omega)\theta(E + \hbar\omega - E_F)dE \tag{2.4}$$

Finally STM is used to describe electronic states of the surfaces by introducing a potential difference between the tip and the sample.In this way it is possible to have a spatial map of the wave function at different energies for both empty and filled states (see Fig. 2.1).

In conclusion it is worth mentioning that spectroscopies which study the electronic structure are also an indirect test of the surface atomic structure.

2.1.3 Reflectivity anisotropy experimental spectroscopy

Optical spectroscopy is an important tool to probe surfaces since they allow for *in situ*, non–destructive and real–time measurements. Moreover, material damage or contamination associated with charged particle beams are avoided.

However, since the light penetration and wavelength are much larger than typical surface thicknesses (few Å), optical spectroscopy is less sensitive to the surface.

Nevertheless, a trick can be used in order to resolve the surface signal. This is the case of Reflectivity Anisotropy Spectroscopy (RAS) and Surface Differential Reflectivity (SDR), optical techinques of great importance for detecting transitions between surface states. Surface sensitivity is greatly enhanced with the use of appropriate conditions which enhance the contribution of interband transitions involving surface states [33].

RAS is defined as the difference between the normalized reflectivities measured at normal incidence, for two orthogonal polarizations of light belonging to the surface plane:

$$\begin{aligned} RAS &= 2\frac{R_y - R_x}{R_y + R_x} \\ &= 2\frac{(R_0 + \Delta R_y) - (R_0 + \Delta R_x)}{2R_0 + \Delta R_y + \Delta R_x} \end{aligned} \tag{2.5}$$

where R_0 is the isotropic Fresnel reflectivity. Since the bulk of a cubic material is optically isotropic, any reflectivity anisotropy must be related to the reduced symmetry of the surface or to another symmetry breaking perturbation, for instance an electric field. In the case of $\frac{\Delta R_\alpha}{R_0} << 1$ we can write:

$$RAS \simeq \frac{\Delta R_y - \Delta R_x}{R_0} \tag{2.6}$$

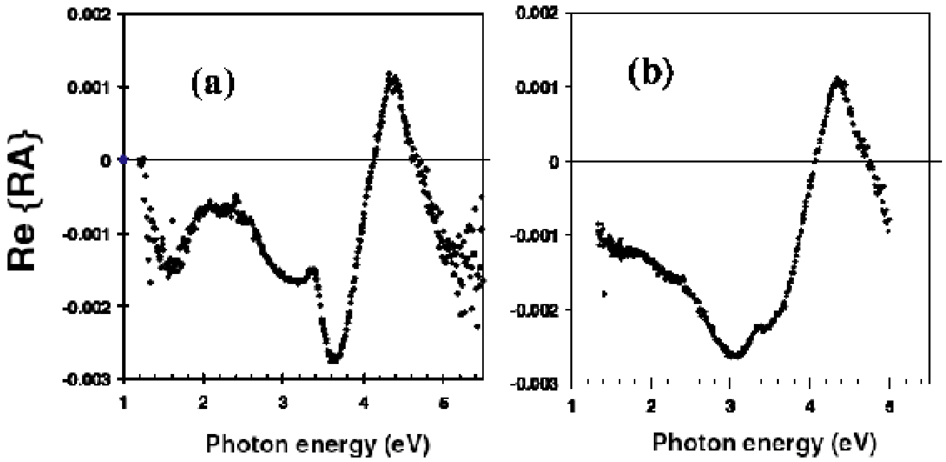

Figure 2.3: Experimental RA spectrum of the clean Si(100). We report as an example, the results taken from Ref. [34] to show how the choice of the surface can affect a RA spectra: Nominal (a) and vicinal (b) surfaces are considered, and it is evident how the low energy spectral features are enhanced in the case of the nominal surface.

An example of measured RAS is represented in Fig. 2.3 and geometry scattering is shown in Fig. 2.6.

On the contrary an SDR spectrum is defined by the difference in the reflectivity measured on a clean surface before and after passivation (e.g. by adsorbing atoms or molecules on the surface). Passivation (oxidation, the case we discuss in chapter 5), removes surface states but does not affect bulk contributions. One hence obtains, for the optical response specific to the surface:

$$SDR = \frac{\Delta R_{clean} - \Delta R_{pass}}{R_{clean}} \tag{2.7}$$

In conclusion, it is important to mention that all these techinques can be appreciably sensitive to the experimental definition of the surface in the sense that in some cases (e.g. Si(100) and Si(100):O, as treated in this work: see chapters **??**) the RA signal is modified because of the presence of steps, terrace or different oriented domains. The influence of steps on the reflectance spectra has been analysed by Jaloviar *et al.* [35]; hence Shioda and der Weide [36] use highly oriented surfaces (with terraces 1000 times larger than vicinal surfaces) in order to obtain more accurate RA profiles. Finally, a comparison of RA spectra obtained by nominal and vicinal surfaces is shown as an example in Fig. 2.3 where we reproduce data from Ref. [34] to illustrate how the use of nominal surfaces improves the spectral resolution in the low energy region of the spectrum.

2.1.4 Electron energy loss spectroscopy at surfaces

A natural complement to optical spectroscopy is Electron Energy Loss Spectroscopy (EELS) which, despite some complications in the interpretation of the data, turns out to be surface sensitive probe, particularly in High Resolution EELS (HREELS), which uses low energy incoming beams.

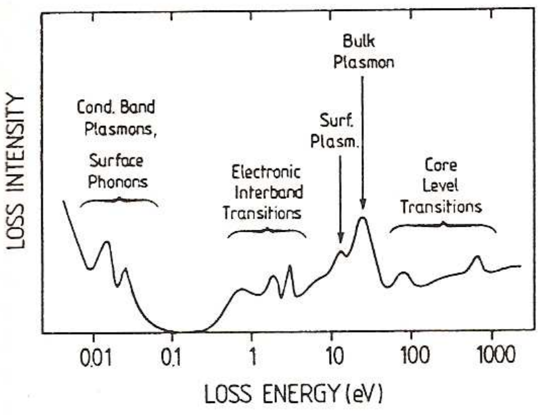

Figure 2.4: Schematic representation of all kind of excitations that can be detected by EEL spectroscopy. This figure is reproduced from [26]

In an EEL experiment a material is exposed to a beam of electrons with a defined narrow range kinetic energy. Some of the electrons undergo inelastic scattering, losing part of their energy and having their paths slightly and randomly deflected from the specular direction. The amount of energy loss can be measured via an electron spectrometer and interpreted in terms of excitations of the sample. Inelastic interactions include phonon excitations, inter and intra-band transitions, plasmon excitations, and inner shell ionizations (see Fig. 2.4).

Usually EELS is performed in transmission, but to be surface sensitive it must be applied in a reflection geometry (REELS), see Fig. 2.7, and use relatively low incident energies (around 50–100 eV, versus 1 keV for bulk). In HREELS the beam is highly monochromatic and the energies of the electrons range up to few eV.

2.2 Theoretical surface spectroscopies

A real surface is a complex physical system whose geometry, i.e. atomic positions, is generally unknown and usually involve many degrees of freedom. This makes calculations very heavy and can create serious obstacles when fully treating excited states. For this reason calculations are usually performed at different levels of sophistication, involving various simplifications and approximations, according to the accuracy required and the numerical heaviness.

We assume to be able to calculate the dielectric tensor of a general bulk system (as discussed in the previous chapters) and we are going to describe how to use it in order to reproduce and predict surface spectroscopic experiements.

2.2.1 The slab method

The description of the crystal termination is solved here using the slab method, i.e. representing the surface by means of an atomic slab of suitable thickness (usually 20-30 Å). Using plane-wave basis sets, the three dimensional periodicity of the system can be recovered by considering repeated slabs, separated by a sufficiently large region of empty space.

In Figure 2.5 we illustrate the example of a slab inside a supercell and indicate the three layers involved (giving the name to the three layers model): a bulk region (composed by the inner atoms of the slab), a surface layer with thickness d (top layers of the slab), and a vacuum volume. The thickness of the surface layer must be smaller than the wavelength λ of the light. The bulk properties are assumed to be described by an isotropic dielectric function $\varepsilon_b(\omega)$ and the surface is described by a frequency dependent dielectric tensor, where the complex diagonal elements are defined by $\varepsilon_{xx}(\omega)$, $\varepsilon_{yy}(\omega)$ and $\varepsilon_{zz}(\omega)$.

In practical calculations, the vacuum region is chosen large enough to avoid the interaction between the two surfaces of the slab and careful convergence tests have to be performed. Figure 2.5 shows the case of a symmetric slab geometry describing an oxidised silicon surface. The slab method is general; also non symmetric slabs can be used, even if the case is not treated in this thesis.

2.2.2 Real–Space slicing technique

Within the description of the three-layers model, an electron impinging on the surface feels the potential from this surface layer through its dielectric function ε_s as well as the potential of the bulk region. However, microscopic calculations generally

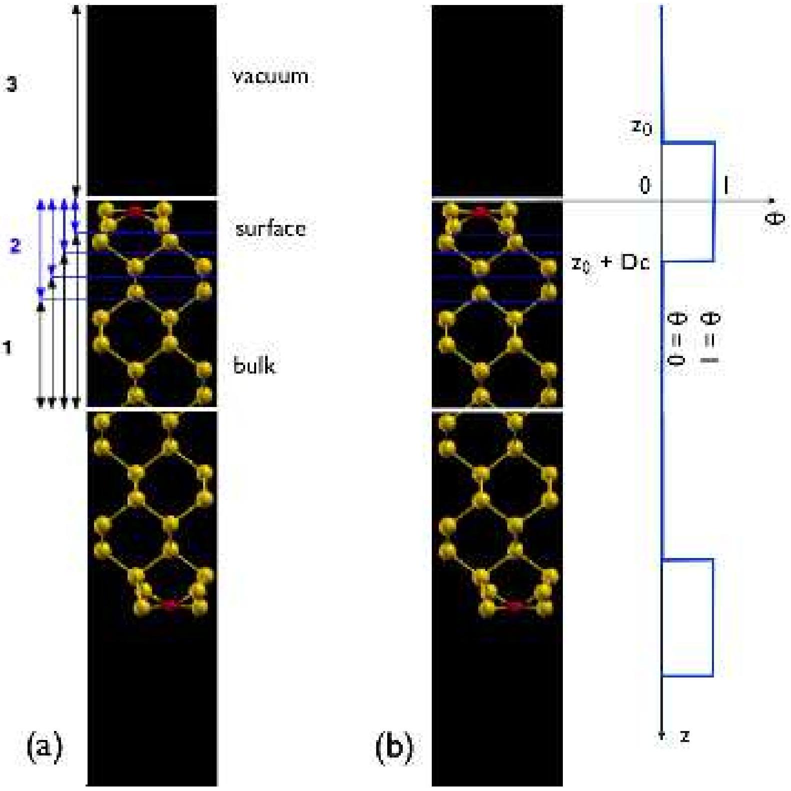

Figure 2.5: Schematic representation of an oxidised silicon surface whithin the supercell approach used in our calculations. 4 oxygen atoms (red circles) and 64 silicon atoms (yellow circles) form the symmetric slab. The supercell is the union of the 16 layer slab and the vacuum region. In figure (a), the bulk, surface and vacuum regions of the three-layer model are indicated for the upper half of the slab. On Fig. (b) blue line represents an example of a cutoff function used in the real-space slicing technique.

output the dielectric function of the supercell ε_c. In previous works [37], ε_s was extracted from ε_c by using the expression:

$$I(\omega) = (N_b - 2N_s)d_l\varepsilon_b(\omega) + 2N_s d_l \varepsilon_s(\omega) \tag{2.8}$$

Here d_l is the interlayer spacing, N_s (N_b) is the number of layers in each surface (bulk) region, and I is the integral of the slab RPA dielectric susceptibility $\varepsilon(\omega, z, z')$ over z and z', i.e., $I(\omega) = N_c d_l \varepsilon_c$. However this approach cannot always guarantee perfect cancellation of the bulklike layers in the supercell, and may even lead to unphysical negative loss features. A more reliable approach is to extract ε_s directly using a *real–space slicing* technique, i.e. by projecting out the response of a defined surface layer using a *cut off* function in real space (for a detailed treatment see Ref. [38]).

This technique is usually reported in terms of the polarizibility of the half slab α^{hs}, which, in case of symmetric slabs, is obtained dividing by 2 the full polarizability α:

$$\mathrm{Im}[4\pi\alpha_{ii}^{hs}(\omega)] = \frac{4\pi^2 e^2}{m^2\omega^2 A}\sum_k\sum_{v,c}|P^i_{v\mathbf{k},c\mathbf{k}}|^2\delta(E_{c\mathbf{k}} - E_{v\mathbf{k}} - \hbar\omega) \tag{2.9}$$

where $P^i_{v\mathbf{k},c\mathbf{k}}$ are the matrix elements of the momentum operator[2].

We introduce now a cutoff function $\theta(z)$ aimed at *projecting out* the optical transitions related to a certain selected region of the slab. The function $\theta(z)$ is a sum of two Heaviside step functions:

$$\theta(z) = H(z - z_0) - H(z - (z_0 + D_c)) \tag{2.10}$$

where D_c is the thickness of the cutoff function (see Fig. 2.5).

The cutoff function is introduced into the calculation of the optical properties through the use of a modified matrix element $\tilde{P}_{v\mathbf{k},c\mathbf{k}}$, defined by:

$$\tilde{P}^i_{v\mathbf{k},c\mathbf{k}} = -i\hbar\int d\mathbf{r}\psi^*_{v\mathbf{k}}(\mathbf{r})\theta(z)\frac{\partial}{\partial r_i}\psi_{c\mathbf{k}}(\mathbf{r}), \tag{2.11}$$

and hence the polarizability of the slice is described by the relation:

$$\mathrm{Im}[4\pi\alpha_{ii}^{cut}(\omega)] = \frac{8\pi^2 e^2}{m^2\omega^2 A}\sum_k\sum_{v,c}[P^i_{v\mathbf{k},c\mathbf{k}}]^*\tilde{P}^i_{v\mathbf{k},c\mathbf{k}}\delta(E_{c\mathbf{k}} - E_{v\mathbf{k}} - \hbar\omega). \tag{2.12}$$

In the next paragraphs we will show an application of this technique to analyse the layer-by-layer contribution of the electron energy loss spectra.

2.2.3 Theory of RAS

By exploiting a reflection geometry and the polarizability of the incident wavevector, certain spectroscopies are able to resolve the surface contribution to the optical properties of a material. In the case of normal incidence light travelling from a first medium with $\varepsilon = \varepsilon_1$ to a second medium with $\varepsilon = \varepsilon_2$ (see Fig. 2.6) the Fresnel reflectivity is defined by :

$$R_0 = \left|\frac{N_2 - N_1}{N_2 + N_1}\right|^2 = \left|\frac{\sqrt{\varepsilon}_2 - \sqrt{\varepsilon}_1}{\sqrt{\varepsilon}_2 + \sqrt{\varepsilon}_1}\right|^2 \tag{2.13}$$

---

[2] If the pseudopotential is non local, $\hat{v}m$ is used instead of the momentum operator

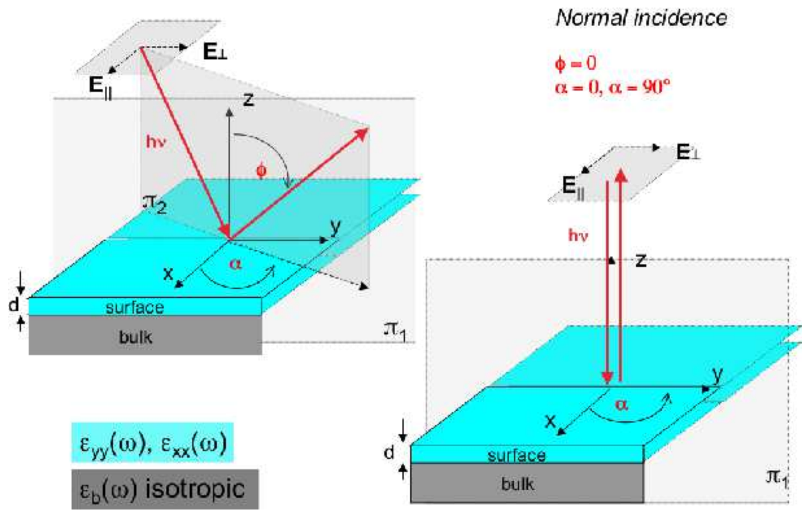

Figure 2.6: Schematic illustration of the general SDRS geometry in oblique incidence (left), and RAS assuming normal incidence (right). The light propagation direction is represented by red lines, and we indicate the polarization of light in two orthogonal directions belonging to the surface plane. The bulk is assumed to be isotropic, while the surface is described by a frequency dependent dielectric tensor with eigenvectors parallel to x and y.

where $N_i = \sqrt{\varepsilon_i}$ is the complex refraction index $N = n_1 + in_2$.
Accordingly, *reflectance* is defined as a complex number r for which $R = |r|^2$. From the experimental point of view, measurements are usually performed with respect to this quantity by:

$$I(\omega) = \frac{I_{rif}(\omega)}{I_{inc}(\omega)} = \left|\frac{E_0^{rif}}{E_0^{inc}}\right|^2 = |r|^2 \tag{2.14}$$

On the contrary, reflectivity is a real number and $R \in [0,1]$ with special cases occurring when $R = 1$ (large difference between N_1 and N_2), $R = 0$ ($N_1 = N_2$) or when N_i for the two media are both real or imaginary. Reflectance is a complex quantity linking the electric field amplitudes:

$$E = E_0 e^{i(\beta \mathbf{kx} - \omega t)} = E_0 e^{i\frac{\omega}{c}(Nx - ct)} = E_0 e^{i\frac{\omega}{c}(n_1 x - ct)} e^{-\frac{\omega}{c} n_2 x} \tag{2.15}$$

where $\omega = vk$, and hence $k = \frac{\omega}{v} = \frac{\omega}{c}N$. From Eq. 2.15 we can write:

$$|E|^2 = |E_0|^2 e^{-2\frac{\omega}{c} n_2 x} \tag{2.16}$$

from which we deduce that energy decreases exponentially.
If now we consider the energy density $\bar{\omega}$ and the absorption coefficient α:

$$\frac{\partial\bar{\omega}}{\partial x} = -\alpha\bar{\omega} \tag{2.17}$$

we obtain:

$$\begin{aligned} \alpha &= \frac{2\omega}{c} n_2 && (2.18) \\ \mathrm{Re}\varepsilon &= n_1^2 - n_2^2 && (2.19) \\ \mathrm{Im}\varepsilon &= n_1 n_2 && (2.20) \end{aligned}$$

and finally

$$\alpha = \frac{\varepsilon_2}{n_1}\frac{\omega}{c}. \tag{2.21}$$

In the case of an interface with vacuum, the reflectivity is simplified:

$$R(\omega) = \left|\frac{N-1}{N+1}\right|^2 = \left|\frac{(n_1-1)^2+n_2}{(n_1+1)^2+n_2}\right|^2 \tag{2.22}$$

In the case of non normal incidence (see Fig. 2.6) two contributions are distinguished:

$$\begin{aligned} R_s &= \left|\frac{\cos\theta - \sqrt{\varepsilon - \sin^2\theta}}{\cos\theta + \sqrt{\varepsilon - \sin^2\theta}}\right|^2 && (2.23) \\ R_p &= \left|\frac{\varepsilon\cos\theta - \sqrt{\varepsilon - \sin^2\theta}}{\varepsilon\cos\theta + \sqrt{\varepsilon - \sin^2\theta}}\right|^2 && (2.24) \end{aligned}$$

related to p and s waves respectively.

In experiments, the RA spectrum is calculated starting from the knowledge of the reflectance and hence the reflectivity by means of Eq. 2.5.
Theoretical models link reflectivity to the dielectric tensor. In the particular case where $\frac{\Delta R_i}{R_0} << 1$, the relative deviation of the reflectivity with respect to the Fresnel contribution is given in terms of the surface and bulk dielectric tensor ε_s, ε_s by the equation:

$$\frac{\Delta R_i}{R_0} = \frac{4\omega}{c}\cos\theta \mathrm{Im}\left(\frac{\varepsilon_{ii}^s - \varepsilon_b}{\varepsilon_b - 1}\right) \tag{2.25}$$

representing SDRS formula in s-polarization, or, in the case of normal incidence:

$$\frac{\Delta R_i}{R_0} = \frac{4\omega}{c}\mathrm{Im}\left(\frac{4\pi\alpha_{ii}(\omega)}{\varepsilon_b - 1}\right) \tag{2.26}$$

In Eq. 2.26 we used the slab polarizability instead of the surface and bulk dielectric function. More details of this theory can be found in reference [33].

2.2.4 Theory of electron energy loss at surfaces

We use a semiclassical dipole scattering theory that accounts for the long-range interaction between the incident electrons and the medium under study [26, 39]. Assuming planar scattering, and taking yz as being the scattering plane (z is the surface normal, see Fig. 2.7) the scattering probability is defined by:

$$\mathrm{P}(\mathbf{k},\mathbf{k}') = \mathrm{A}(\mathbf{k},\mathbf{k}')\ \mathrm{Im}\ \mathrm{g}(\mathbf{q}_{||},\omega) \tag{2.27}$$

where $\mathbf{k}$ and $\mathbf{k}'$ are the incident and scattered wavevectors respectively. The kinematic factor, $\mathrm{A}(\mathbf{k},\mathbf{k}')$:

$$\mathrm{A}(\mathbf{k},\mathbf{k}') = \frac{2}{(ea_0\pi)^2}\frac{1}{\cos\theta}\frac{k'}{k}\frac{q_{||}}{|q_{||}^2+q_{\perp}^2|^2} \tag{2.28}$$

mostly contains the information concerning the scattering geometry (see Fig. 2.7).

The angle θ is the direction of the incident beam with respect to the normal to

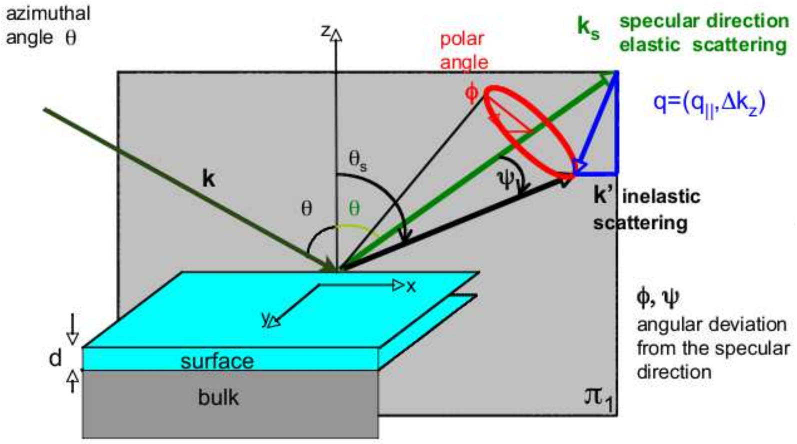
azimuthal angle θ
z
polar angle
φ
k_s
specular direction elastic scattering
$q=(q_{||},\Delta k_z)$
θ_s
k
θ
θ
ψ
k' inelastic scattering
x
y
d
surface
bulk
φ, ψ
angular deviation from the specular direction
π_1

Figure 2.7: Schematic representation of the reflection geometry for Electron Energy Loss Spectroscopy experiments.

the surface plane, and $q_{||}, q_{\perp}$ are the parallel and perpendicular components of the transferred momentum $\mathbf{q} = \mathbf{k} - \mathbf{k}'$.

The loss function is defined by:

$$\mathrm{g}(\mathbf{q}_{||},\omega) = -\frac{1}{1+\varepsilon_{\mathrm{eff}}(\mathbf{q}_{||},\omega)} \tag{2.29}$$

and represents the part of Eq. 2.27 involving the approximation of the model and the separation between bulk and surface contributions to the dielectric function.

If the surface were to be modelled as a semi-infinite truncated bulk, $\varepsilon_{\mathrm{eff}}$ would be replaced by ε_{b} and we would obtain the familiar expression of Mills [39].

In this work we adopt an anisotropic three-layer model of the surface as derived by Selloni and Del Sole [40, 41]. The surface is modelled as in Fig. 2.8: a semi-infinite layer of vacuum, a surface layer of thickness d, represented by the surface dielectric *tensor* ε_s, and a semi-infinite layer of bulk (dielectric function ε_b). The effective dielectric function is defined by:

$$\begin{aligned}\varepsilon_{\mathrm{eff}}(\mathbf{q}_{||},\omega) &= \varepsilon_s(\mathbf{q},\omega)\times\\ &\times\frac{\varepsilon_s(\mathbf{q},\omega)+\varepsilon_b(\mathbf{q},\omega)+\Delta(\mathbf{q},\omega)e^{-2\mathbf{q}_{||}d\varepsilon_{\mathrm{aux}}(\mathbf{q},\omega)}}{\varepsilon_s(\mathbf{q},\omega)+\varepsilon_b(\mathbf{q},\omega)-\Delta(\mathbf{q},\omega)e^{-2\mathbf{q}_{||}d\varepsilon_{\mathrm{aux}}(\mathbf{q},\omega)}}\end{aligned}\tag{2.30}$$

where d is the thickness of the surface, $\varepsilon_b(\mathbf{q},\omega)$ and $\varepsilon_s(\mathbf{q},\omega)$ are the bulk and surface dielectric function and $\Delta(\mathbf{q},\omega)=\varepsilon_b(\mathbf{q},\omega)-\varepsilon_s(\mathbf{q},\omega)$.

In particular $\varepsilon_s(\mathbf{q},\omega)$ and the auxiliary function $\varepsilon_{aux}(\mathbf{q},\omega)$ are written as a function of the y,z components of the dielectric tensor: $\varepsilon_s(\mathbf{q},\omega)=\sqrt{\varepsilon_{s,y}(\mathbf{q},\omega)\varepsilon_{s,z}(\mathbf{q},\omega)}$ and $\varepsilon_{\mathrm{aux}}(\mathbf{q},\omega)=\sqrt{\frac{\varepsilon_{s,y}(\mathbf{q},\omega)}{\varepsilon_{s,z}(\mathbf{q},\omega)}}$.

Although the dielectric functions appearing in Eq. 2.30 are fully dependent on $q_{||}$ and ω, such quantities are not easy to calculate, since q and ω are not independent. Hence we make the approximation of replacing $\varepsilon_s(\mathbf{q},\omega)$ with the optical dielectric function $\varepsilon_s(\omega)\approx\lim_{\mathbf{q}\to 0}\varepsilon_s(\mathbf{q},\omega)$. This appears to be a reasonable assumption since for most of the experiments modelled in this work, q is rather small.

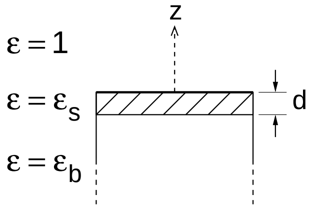

Figure 2.8: Schematic representation of the constituent parts of the three-layer model of the surface.

Surface dielectric functions are calculated according to Ref. [38] using a cutoff function (as discussed in the previous sections) in order to select the number of terminal layers contributing to the surface response.

Part II

Development

Chapter 3

Efficient calculation of the electronic polarizability

In this section we show the application of an efficient numerical scheme to obtain the independent–particle dynamic polarizability matrix $\chi^{(0)}(r, r', \omega)$, a key quantity in modern *ab initio* excited state calculations. The method has been applied to the study of the optical response of a realistic oxidized silicon surface, including the effects of crystal local fields. The latter are shown to substantially increase the surface optical anisotropy in the energy range below the bulk bandgap. Our implementation in a large–scale *ab initio* computational code allows us to make a quantitative study of the CPU time scaling with respect to the system size, and demonstrates the real potential of the method for the study of excited states in large systems.

3.1 Motivations

The recent developments of experimental techniques for the non destructive study of solid surfaces call for a simultaneous improvement of the theoretical tools: the interpretation and prediction of optical and dielectric properties of surfaces require more and more quantitative and reliable *ab initio* calculations, possibly including many–body effects. Such an improvement of the theoretical description can be achieved, for example, by lifting some of the usual approximations adopted in the calculation of the optical response. However, making less approximations increases the computational heaviness, and is only possible if efficient numerical algorithms can be adopted. A good example is given by the calculation of the independent–

particles dynamical polarizability matrix $\chi^{(0)}(\mathbf{r},\mathbf{r}',\omega)$, which is often required as the starting point in Time-Dependent Density Functional Theory (TDDFT) [23] and in Many-Body Perturbation Theory-based calculations, such as in the GW [42], or GW+Bethe-Salpeter schemes (for a review, see e.g. ref. [3]). Evaluating the full response matrix for realistic, many-atoms systems can be computational challenging, since it requires a computational effort growing as the fourth power of the number of atoms, and the availability of efficient numerical schemes becomes a key issue.
Recently, schemes allowing to decouple the sum-over-states and the frequency dependence have been presented. Miyake and Aryasetiawan [43] and Shishkin and Kresse [44] have shown that methods based on the Hilbert transform can substantially reduce the computational cost of frequency-dependent response functions, making it comparable to that of the static case. In particular the approach presented in [43] has been applied to a linear-muffin-tin-orbital (LMTO) calculation of the spectral function of bulk copper, while in [44], a work focused on the GW implementation using the Projector Augmented-Wave method (PAW [45]), a similar approach is used to compute the spectral function of bulk silicon and materials with d electrons (GaAs and CdS). Another recent work by D. Foerster [46] is focused on the same issue and demonstrates how the use of a basis of local orbitals can reduce the scaling of a susceptibility calculation for an N–atom system from N^4 to N^3 operations for each frequency, but at the cost of disk space.
However, the application of such non-traditional methods to large supercells, such as those involved in real surface calculations, have not been presented so far.
It may be stressed that for a given application the computational burden is determined not only by general scaling law, but also by prefactors. In particular, prefactors determine the crossover where one method becomes more convenient than the other. This crossover has not yet been discussed for the Hilbert transform methods.

In the present work, we demonstrate the application of a scheme -similar to that introduced in [43] and [44]- based on the efficient use of the Hilbert transforms, by performing the calculation of the optical properties of a realistic, reconstructed surface: Si(100)(2×2):O, covered with 1 monolayer (ML) of oxygen.
We provide a *quantitative* evaluation of the computational gain for this calculation of the full dynamical independent-particle polarizability. The latter is constructed from Kohn-Sham eigenvalues and eigenvectors and is then used to compute surface optical spectra, including for the first time the local field (LF) effects on Reflectance Anisotropy (RAS) and Surface Differential Reflectivity (SDR) spectra of this surface.

3.1.1 Local filed effects

The impact of local fields on surface optical spectra has been a controversial issue for decades, specially concerning the so-called *intrinsic* or bulk–originated effects. The latter have been measured, for energies above the bulk bandgap, since the seminal works by Aspnes and Studna [47] showing that the normal incidence optical reflectivity of natural Si(110) and Ge(110) surfaces displays an anisotropy of the order of 10^{-3}. The effect was called intrinsic since it is not due to the existence of surface states, nor to surface reconstruction. Early model calculations by Mochan and Barrera [48] performed for a lattice of polarizable entities and exploiting the Clausius-Mossotti relation pointed out that intrinsic anisotropies could be due to LF effects. A subsequent work by Del Sole, Mochan and Barrera [37] based on Tight Binding (TB) method has shown that the RAS spectra calculated for Si(110):H within this semiempirical scheme did not reproduce well the experimental data, despite the inclusion of surface LF effects. However, more recent calculations based on realistic bandstructures (within DFT-LDA with GW-corrected band gap) [49] have suggested that intrinsic anisotropies at the bulk critical points for the (almost ideally terminated) Si (110):H surface could arise as a consequence of surface perturbation of bulk states, without invoking LF effects. Other tight-binding calculations (see, e.g., ref. [50]) suggested the existence of intrinsic surface optical anisotropies not due to surface local fields.

A substantial advance in clarifying the role of local fields has been achieved only recently by F. Bechstedt and co-workers, who carried out a calculation of the RAS spectra of Si(110):H [51] and monohydride Si(100)(2x1) [52] including self-energy, crystal local fields, and excitonic effects from a fully *ab initio* point of view. In both the considered surfaces, which have no surface states within the bulk bandgap, the LF were found to cause a slight decrease of the optical reflectivity; however, the effect was found to cancel to a large extent in the RAS spectra, being almost identical for the two polarizations of the incident light. The situation may be different in the case of extrinsic optical anisotropies, i.e. those directly related to surface states and surface reconstruction, and appearing below the bulk bandgap. In at least one case substantial effects due to LF have been reported [53]. However, further calculations for a wider class of surfaces are necessary in order to assess this point more precisely. The system we consider here belongs to a widely studied family of surfaces, because of their importance in the understanding of silicon-silicon dioxide interfaces in semiconductor technology. Despite the many experimental [54, 55, 56, 57, 58, 59, 60] and theoretical [61, 62, 63, 64, 65, 66] works appeared in recent years, the debate on the oxidation mechanism of Si(100) is still open. However, the most favorable oxygen adsorption sites in the first stages of (room-temperature) oxidation process have been identified as the dimer-bridge position, and a bridge position on the backbond corresponding to the lower atom of the dimer. This remark is supported by STM experiments [60] and by a first-principles molecular dynamics calculation [66]. From the theoretical point of view, ground and excited state properties of Si(100)(2×2):O at 0.5 and 1ML coverage have been recently studied by some of the authors [67]; however, computational limits prevented till now the inclusion of the local–field effects in the *ab initio* calculation of optical properties.

In the following paragraphs we brefly summarize the theoretical framework and the expression of $\chi^{(0)}$ usually employed in plane–wave based calculations. Then we show how the Hilbert transform (HT) technique can be applied, as a generalization of the Kramers–Kronig relations, in order to decouple the sum-over-states and the frequency dependence in $\chi^{(0)}$. Moreover an estimation of the accuracy and the possible computational gain are presented for a model system.

3.2 Theoretical framework

The starting point of our work is a DFT-LDA ground state calculation performed with the ABINIT code [68] yielding independent-particle eigenvalues and eigenvectors within the Kohn-Sham scheme [1, 2]. Besides to the occupied ones, empty (conduction) states up to an energy of several eV above the Fermi level are obtained by means of iterative diagonalization techniques.

However, in order to study the optical and dielectric response, the level of theory must be brought beyond the ground state one, using, e.g., many–body perturbation theory or TDDFT [23]. The latter is particularly suited for the study of neutral excitations, as those involved in optical reflectivity and electron energy-loss.

3.2.1 Fundamental ingredients

Within TDDFT, it is possible to obtain the retarded density-density response function $\chi(\mathbf{r}, \mathbf{r}', \omega)$ from its non-interacting Kohn-Sham counterpart $\chi^{(0)}(\mathbf{r}, \mathbf{r}', \omega)$ through a Dyson-like equation:

$$\chi = \chi^{(0)} + \chi^{(0)} K \chi \tag{3.1}$$

where the kernel K contains two terms: the Coulomb potential, v_c, and the exchange-correlation kernel, $f_{xc}(\mathbf{r}, \mathbf{r}', \omega)$. An explicit expression for χ is then given by

$$\chi = \chi^{(0)} \left[1 - (v_c + f_{xc})\chi^{(0)} \right]^{-1} . \tag{3.2}$$

Eq.s (3.1) and (3.2) are matrix equations, involving two-points functions such as χ and $\chi^{(0)}$. In the present case, working within a plane-waves expansion, $\chi_{\mathbf{GG}'}(\mathbf{q}, \omega)$ and $\chi^{(0)}_{\mathbf{GG}'}(\mathbf{q}, \omega)$ are matrices in reciprocal space, and $v_c(\mathbf{q} + \mathbf{G}) = \frac{4\pi}{|\mathbf{q}+\mathbf{G}|^2}$ is the Coulomb potential. The exchange-correlation contribution, f_{xc}, is not exactly known. It can be included in an approximate form, e.g. using the LDA functional [5, 7] in the adiabatic approximation (ALDA), or in a more sophisticated approximation such as those described in [69, 70, 71, 72, 73, 74]. In order to compare with optical experiments, the macroscopic dielectric function $\varepsilon_M(\omega)$ must be calculated. The latter is defined as:

$$\varepsilon_M(\omega) = \lim_{q \to 0} \frac{1}{\varepsilon^{-1}_{\mathbf{G}=\mathbf{G}'=0}(\mathbf{q}, \omega)} \tag{3.3}$$

where the inverse dielectric function $\varepsilon^{-1}_{\mathbf{G},\mathbf{G}'}(\mathbf{q}, \omega)$ is linked to the response function χ by:

$$\varepsilon^{-1}_{\mathbf{G},\mathbf{G}'}(\mathbf{q}, \omega) = 1 + v_c(\mathbf{q} + \mathbf{G})\chi_{\mathbf{G},\mathbf{G}'}(\mathbf{q}, \omega). \tag{3.4}$$

When only v_c is included in the kernel K of eq.(3.1) exchange and correlation effects in the response are neglected, while the use of the correct expression (3.3) still consider the LF effects [75]. Already at this level the calculations can become time consuming from the computational point of view when the full $\chi^{(0)}(\mathbf{r}, \mathbf{r}', \omega)$ matrix has to be obtained. In complex systems with large unit cells the only tractable way to proceed is often to neglect local fields, by assuming that $\varepsilon_M(\omega)$ is well approximated by the average of the microscopic dielectric function:

$$\varepsilon_M^{NLF}(\omega) = \lim_{\mathbf{q} \to 0} \varepsilon_{\mathbf{0},\mathbf{0}}(\mathbf{q}, \omega) \tag{3.5}$$

This corresponds to neglecting the off-diagonal elements of ε in reciprocal space [1]. When moreover exchange and correlation effects are neglected, (independent quasi-particle approximation or IP-RPA) the imaginary part of the macroscopic dielectric function ε_M^{NLF} takes the simple Ehrenreich and Cohen [76] form:

$$\mathrm{Im}\varepsilon_M^{NLF}(\omega) = \frac{16\pi}{\omega^2} \sum_{ij} | < \psi_i|\mathbf{v}|\psi_j > |^2 \delta(\epsilon_j - \epsilon_i - \omega) \tag{3.6}$$

---

[1] In real space, this corresponds to assume a dependence of $\varepsilon_M(\mathbf{r}, \mathbf{r}')$ only on the difference $(\mathbf{r} - \mathbf{r}')$

where $\mathbf{v}$ is the velocity operator and i, j stand for occupied and unoccupied states respectively. The substantial simplification obtained in this case explains why most of the calculations of the optical properties of real surfaces are done within the independent quasiparticle approach, neglecting local–field effects. On the other hand, a fast and efficient scheme to compute the full matrix $\chi^{(0)}$ represents a key issue in order to be able to go beyond this approximation, e.g. by including the local fields, as we do in the present work. Moreover, an efficient method giving access to the full $\chi^{(0)}$ is of paramount importance when the screened coulomb interaction $W_{\mathbf{GG}'}(\mathbf{q})$ is needed, such as in ab-initio GW calculations. In the following, we hence concentrate on the expression of $\chi^{(0)}$ itself, i.e.:

$$\begin{aligned}\chi^{(0)}(\mathbf{r},\mathbf{r}',\omega) &= 2\sum_{ij} f_i(1-f_j)\psi_i^*(\mathbf{r})\psi_j(\mathbf{r})\psi_j^*(\mathbf{r}')\psi_i(\mathbf{r}') \times \\ &\quad\times\left[\frac{1}{\omega-(\epsilon_j-\epsilon_i)+i\eta}-\frac{1}{\omega+(\epsilon_j-\epsilon_i)+i\eta}\right] \end{aligned} \tag{3.7}$$

where f_i are occupation numbers (0 or 1 in the present case), η is an infinitesimal and the factor 2 is due to the spin degeneracy. Switching to reciprocal space and focusing on the case of semiconductors, we make valence (v) and conduction (c) bands to appear explicitly, and rewrite this equation as:

$$\chi^{(0)}_{\mathbf{G},\mathbf{G}'}(\mathbf{q},\omega)=\frac{2}{\Omega_0 N_k}\sum_{\mathbf{k}}\sum_{c,v}\left[\frac{\widetilde{\rho}_{vc\mathbf{k}}(\mathbf{q}+\mathbf{G})\widetilde{\rho}_{cv\mathbf{k}}(\mathbf{q}+\mathbf{G}')}{\omega-(\epsilon_{c\mathbf{k}}-\epsilon_{v\mathbf{k}})+i\eta}-\frac{\widetilde{\rho}_{cv\mathbf{k}}(\mathbf{q}+\mathbf{G})\widetilde{\rho}_{vc\mathbf{k}}(\mathbf{q}+\mathbf{G}')}{\omega+(\epsilon_{c\mathbf{k}}-\epsilon_{v\mathbf{k}})+i\eta}\right] \tag{3.8}$$

where Ω_0 is the volume of the unitary cell and we have also introduced the notation $\widetilde{\rho}_{vc\mathbf{k}}(\mathbf{q}+\mathbf{G})$ to indicate the Fourier transform of $\phi^*_{v\mathbf{k}+\mathbf{q}}(\mathbf{r})\phi_{c\mathbf{k}}(\mathbf{r})$. From the numerical point of view the evaluation of these sums for each frequency ω can become very heavy. Indeed, for a realistic system the evaluation of eq. (3.8) involves, for each frequency, the summation over a large number of terms, which for a system of 50 atoms typically is of the order of 10^8.

3.2.2 The Hilbert-transform approach

Since we consider the case of the $\mathbf{q} \to 0$ limit to study optical properties, in the following the label $\mathbf{q}$ will be omitted to simplify the notation. The generalization to the case of finite $\mathbf{q}$ is straightforward. Introducing a simplified notation for band and $\mathbf{k}$-point indexes, we define a single index of transition t to represent the triplet $\{v,c,\mathbf{k}\}$. In this way, ω_t indicates an (always positive) energy difference, $(\varepsilon_{c,\mathbf{k}}-\varepsilon_{v,\mathbf{k}})$.

We also introduce the two complex quantities:

$$Z_{1,t} = \widetilde{\rho}_{vc\mathbf{k}}(\mathbf{G})\widetilde{\rho}_{cv\mathbf{k}}(\mathbf{G}') \tag{3.9}$$

$$Z_{2,t} = -\widetilde{\rho}_{cv\mathbf{k}}(\mathbf{G})\widetilde{\rho}_{vc\mathbf{k}}(\mathbf{G}') \tag{3.10}$$

such that:

$$\chi^{(0)}_{\mathbf{GG}'}(\omega) = \sum_t \left[\frac{Z_{1,t}}{\omega - \omega_t + i\eta} + \frac{Z_{2,t}}{\omega + \omega_t + i\eta}\right]. \tag{3.11}$$

When $\mathbf{G} = \mathbf{G}'$ (diagonal elements) the $Z_{i,t}$ are real, and $Z_1 = -Z_2$. Using

$$\lim_{\eta \to 0^+} \frac{1}{x \pm i\eta} = \mathcal{P}\left(\frac{1}{x}\right) \mp i\pi\delta(x) \tag{3.12}$$

one can rewrite the $\eta \to 0^+$ limit of equation (3.11) as the sum of four terms:

$$\chi^{R1}_{\mathbf{GG}'}(\omega) = \sum_t \frac{Z_{1,t}}{\omega - \omega_t} \tag{3.13}$$

$$\chi^{R2}_{\mathbf{GG}'}(\omega) = i\pi \sum_t Z_{1,t}\delta(\omega - \omega_t) \tag{3.14}$$

$$\chi^{A1}_{\mathbf{GG}'}(\omega) = \sum_t \frac{Z_{2,t}}{\omega + \omega_t} \tag{3.15}$$

$$\chi^{A2}_{\mathbf{GG}'}(\omega) = i\pi \sum_t Z_{2,t}\delta(\omega + \omega_t) \tag{3.16}$$

R and A label resonant and anti resonant contributions, respectively, and the four terms are general complex quantities. In $\chi^{R2}(\omega)$ and $\chi^{A2}(\omega)$ each term Z_t contributes to the function χ only at $\omega = \omega_t$, and has no effect elsewhere. By discretizing the frequency axis, the sums over t appearing in χ^{R2} and χ^{A2} can hence be performed once and for all, at difference with those labeled by R1 and A1 for which the sums should be calculated for each ω. Thanks to the linearity of the Hilbert transform, defined as

$$Hf(t) = \frac{1}{\pi}\mathcal{P}\int_{-\infty}^{+\infty} \frac{f(x)}{x - t}dx, \tag{3.17}$$

one can however directly obtain χ^{A1} and χ^{R1} from χ^{A2} and χ^{R2}:

$$\chi^{A1} = H\left[\chi^{A2}\right] \tag{3.18}$$

$$\chi^{R1} = H\left[\chi^{R2}\right] \tag{3.19}$$

In such a way[2], it is possible to recover the complete $\chi^{(0)}_{\mathbf{G},\mathbf{G}'}(\omega)$ in the spectral range of interest from the knowledge of a single sum performed over the poles

---

[2] In the case of real matrix elements, $Z_{i,n} \in \mathbb{R}$, one recovers the Kramers-Kronig relations linking real and imaginary parts of the response

ω_t. In other words, one can avoid the explicit summation over $t = \{c, v, \mathbf{k}\}$ to be repeated for each frequency. The present procedure for the calculation of the frequency-dependent polarizability matrices is similar to the method of Miyake and Aryasetiawan [43], with the difference that those authors represented δ-functions using Gaussians, instead of bare rectangular functions as in our case [3].

3.2.3 Numerical efficiency for a toy system

Our scheme has been first tested on a model system[4] in order to check both the accuracy and the efficiency of the algorithm. Figure (3.2) shows the results of the test, comparing $\chi^{(0)}(\omega)$ (real part) as obtained in the traditional way (i.e. by evaluating expression (3.8) for several frequencies), and by the Hilbert transform (HT) algorithm. The results are practically indistinguishable on the scale of the plot. The same figure shows the growth of the required CPU time as a function of the number of transitions (number of $\{v, c, \mathbf{k}\}$ triplets). The gain appears to be proportional to the system size. The possibility to achieve such a large gain, at least in principle and for a simple system, was also noticed in the previous works describing efficient algorithms for the calculation of $\chi^{(0)}$ [43, 44].

Alternative approaches for efficient TDDFT calculations have also been suggested. In particular, another promising scheme based on a superoperator approach and allowing to access TDDFT *spectra* in a numerically efficient way has been recently introduced by Walker and coworkers [77]. This approach is however not designed for the calculation of the whole matrix $\chi^{(0)}$, contrary to the method studied here. In order to know the actual CPU requirements for the calculation of $\chi^{(0)}$, and to

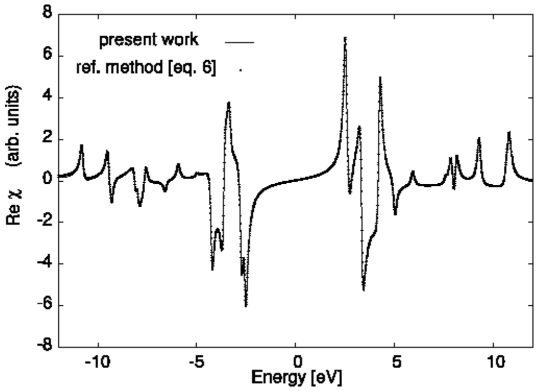

Figure 3.1: Accuracy test for the HT-based algorithm, shown for the real part of $\chi^{(0)}_{\mathbf{G}\mathbf{G}'}(\omega)$ of a model system (see text). The two curves turn out to be indistinguishable on the scale of the plot (maximum error less than 0.5%).

---

[3] Similarly, Shishkin and Kresse [44] used triangular functions

[4] We considered bulk silicon Kohn-Sham energies, increasing the number of transitions to build $\chi^{(0)}$, and randomly redefining the transition matrix elements

explore the possibilities to study complex systems, such as the impurity levels and band offsets mentioned in ref. [44], in practice one has to keep into account the time used to compute the matrix elements (numerators in eq. 3.11), and the time used to perform the Hilbert transforms, which was not explicitly evaluated in previous works. In the following, we hence applied our approach, similar in its essence to that used in [43] and [44], to a large system investigating the actual numerical performances of the algorithm. As it will be shown below, substantial improvements can actually be achieved in such realistic calculations.

Therefore, in the following section, we use our implementation of the HT scheme in the *ab initio* DP code [78] to study a real reconstructed surface: the oxidized Si(100)-(2×2), for which we present the first calculation of its optical reflectivity spectra (RAS and SDR) with the inclusion of local–field effects.

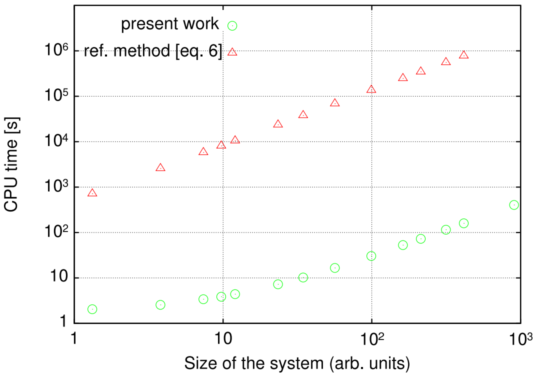

Figure 3.2: Computational load requested to evaluate $\chi^{(0)}_{\mathbf{GG'}}(\omega)$ on a model system, as a function of the number of transitions (which scales as the size of the system), for both the traditional and the HT-based methods.

Finally, we carefully compare the numerical performance of the DP code with and without the use of HTs, and we draw our conclusions.

3.3 Optical properties of oxidized Si(100)-(2×2)

The HT method has been implemented into the large scale, plane–waves *ab initio* TDDFT code named DP, developed by the French node of ETSF [79]. As mentioned in the previous paragraphs, we used it to calculate the optical properties of Si(100)(2×2):O. For this surface we adopt the equilibrium structure for 1ML coverage shown in figure (3.4), which is representative of a situation in which dimer and backbond sites are both occupied by an oxygen atom (structure c3 in ref. [80, 81] and see chapter 5 for further considerations). The surface is simulated with a slab composed by 6 layers, containing 48 Si and 8 oxygen atoms, in a repeated supercell approach. Our structural results agree well with those of previous calculations [62, 82, 80, 81]. We use standard norm conserving pseudopotentials of the Hamann type [21], and an energy cut off of 30 Ry, yielding 15000 plane waves in our unit cell. Eight special (Monkhorst-Pack, [83]) **k**-points in the irreducible Brillouin zone (IBZ) are used for the self-consistent ground state calculation, while a 7×7 grid is used in the evaluation of $\chi^{(0)}_{\mathbf{GG}'}(\omega)$. Kohn-Sham eigenvalues and eigenvectors are obtained for all occupied states (120) and for empty states up to 15 eV above the highest occupied state (top valence). Optical properties are computed through the evaluation of the macroscopic dielectric function with and without the inclusion of local field effects.

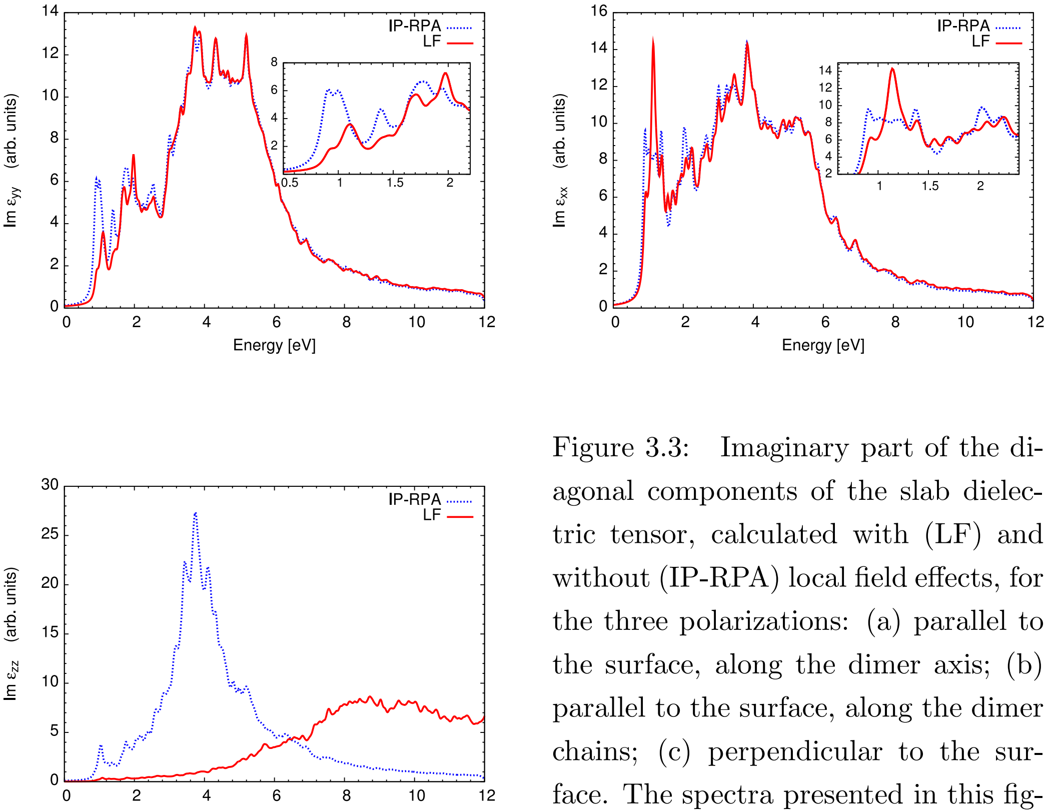

Figure 3.3: Imaginary part of the diagonal components of the slab dielectric tensor, calculated with (LF) and without (IP-RPA) local field effects, for the three polarizations: (a) parallel to the surface, along the dimer axis; (b) parallel to the surface, along the dimer chains; (c) perpendicular to the surface. The spectra presented in this figure are not fully converged in the k-points sampling.

Figure 3.3 shows the imaginary part of the slab dielectric function as a function of the energy. Local–field effects are quite important in the low energy region (0-2)eV, enhancing ε_M for light polarized along the direction of the dimers chains (x direction, see Figure 3.4), and suppressing it for light polarized along the dimers axis (y direction). This goes in the direction of a better description of the microscopic inhomogeneities of the system. In the present case, the extrinsic surface optical anisotropy, as defined in the introduction, is hence found to be visibly affected by

LF. In the case of the third polarization, i.e. the one perpendicular to the surface (not experimentally relevant in the case of normally incident light), local–field effects are huge, and introduce a blueshift of the absorption edge as large as 5 eV. This can be explained by the strong inhomogeneity of the charge distribution in passing from the slab to the vacuum, leading to a classical depolarization effect. Similar behaviors have been found for example in GaAs/AlAs superlattices [84], in graphite [85] and nanowires [86, 87].

Starting from the slab dielectric function, we computed Reflectance Anisotropy (RAS) and Surface Differential Reflectivity (SDR) Spectra [88], with and without inclusion of LF effects. We used theoretical models (see chapter 2 or [33]) linking the RAS and SDR spectra to the dielectric functions evaluated for the bulk crystal (ε_b) and for the slab (ε_{ii}) through the relation:

$$\frac{\Delta R_i}{R_0} = \frac{4\omega}{c}\mathrm{Im}\left[\frac{\varepsilon_{yy}(\omega) - \varepsilon_{xx}(\omega)}{\varepsilon_b(\omega)}\right] \tag{3.20}$$

where ε_{xx} and ε_{yy} are the diagonal components of the surface dielectric tensor. We show our results for RAS and SDR in figures 4.9 and 3.6 respectively.

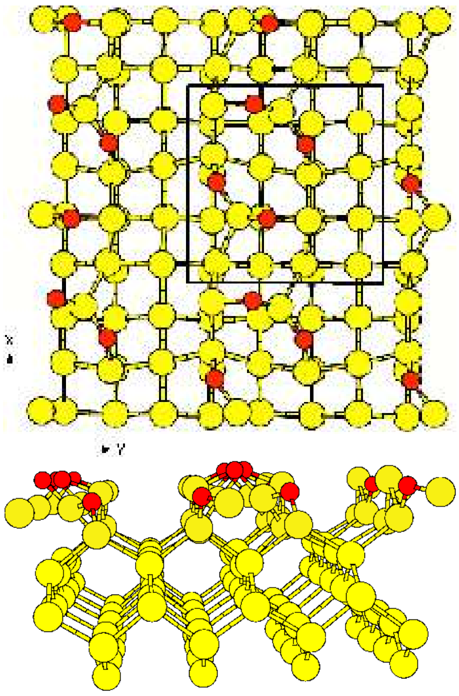

Figure 3.4: Surface structure of Si(100)(2x2):O at 1ML coverage with oxidation of Si dimers and backbonds. oxygen atoms are depicted in dark gray (red), while light gray (yellow) circles represent bulk and surface Si atoms. Dimer chains are oriented along the x direction. (a): top view of the surface (xy plane), with the surface unit cell; (b): lateral view of the half slab (yz plane).

We first discuss the case of RAS. The effects of local fields on the imaginary part of the dielectric tensor are most evident in the low-energy region of the spectrum (below 2 eV), as shown in the inset of Figures 3.3a and 3.3b. In particular, LF are

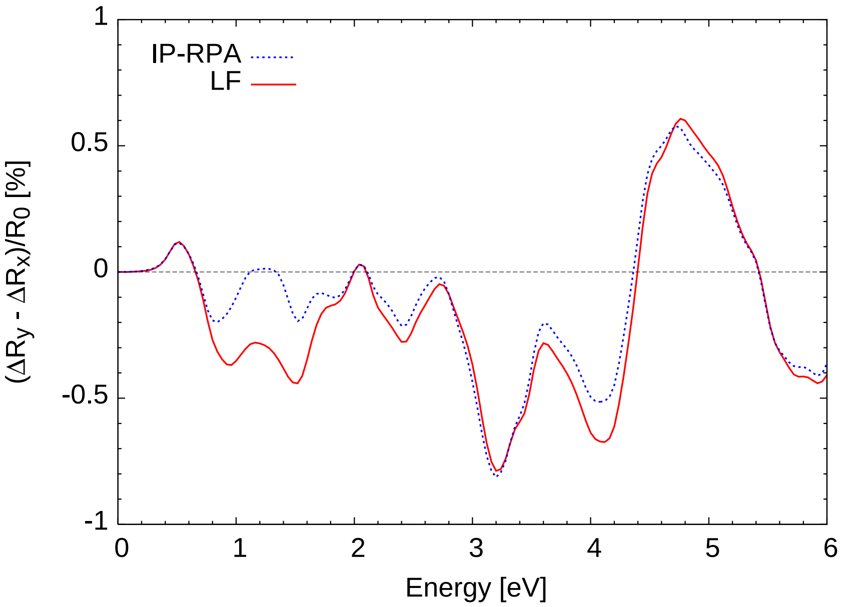

Figure 3.5: Calculated RAS spectrum of Si(100)(2x2):O at convergence, for the structural model shown in figure 3.4. Results including (LF) or neglecting (IP-RPA) the local field effects are very similar, except for the region between 0.8 and 1.8 eV, where the LF effects strongly enhance the RAS signal. The energy scale has been shifted by 0.6 eV to compensate for the neglect of self-energy effects.

found to enhance and sharpen the strong ε_2 peak at about 1.2eV for light polarized along the dimer chains (fig. 3.3b), and to reduce the first three peaks for light polarized along the dimer axis. As a result, LF induce a strong enhancement in the surface optical anisotropy (of the order of 100%) in the region between 0.8eV and 2eV, as displayed in fig. 4.9. This low-energy region (below the direct gap of bulk Si) corresponds to surface-localized states, which are expected to carry the surface anisotropy. The fact that LF evidence this anisotropy is consistent with the fact that dimer chains realize a structure which is geometrically strongly inhomogeneous in the direction perpendicular to the dimer chains (see fig. 3.4). At higher energies (above 2eV) bulk contributions dominate ε_2, and the resulting RAS is mainly due to surface perturbed bulk states. The latter appear to be less affected by local fields than the true surface states, and lead to a RAS spectrum which, above 2.0eV, is almost insensitive to the inclusion of local field effects. This picture is confirmed by the analysis of SDR results. The latter are in fact calculated for unpolarized

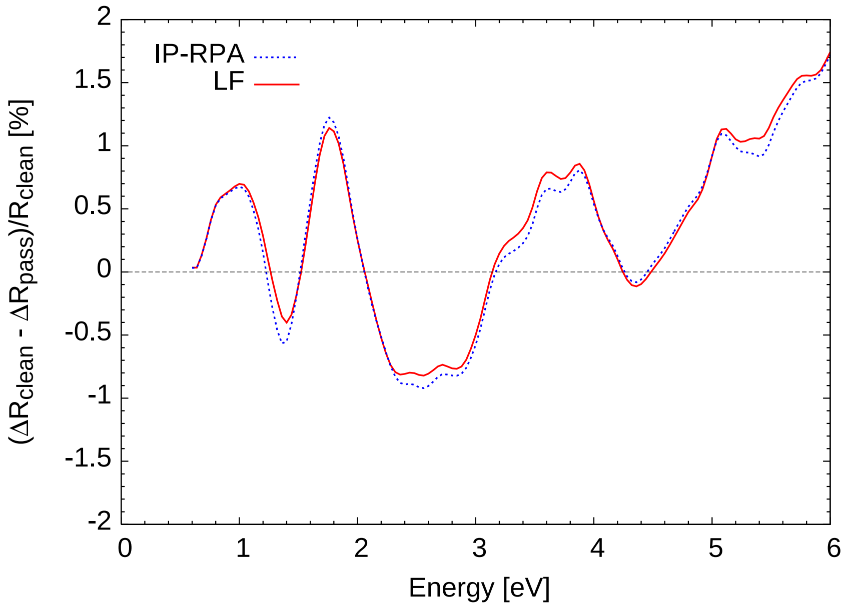

Figure 3.6: Calculated SDR spectrum (unpolarized light) of Si(100)(2x2):O, for the structural model shown in figure 3.4. Results including (LF) or not (IP-RPA) the local fields are almost indistinguishable, showing that the effects visible in the low-energy part of figure 3.3 are canceling each other in the SDR spectrum. The same energy shift as in figure 4.9 has been applied. In *polarized* SDR the local field effects would be of the same size as for the RAS spectra.

light, i.e. by averaging ε_{xx} and ε_{yy}. Since LF enlarge ε_{yy} and reduce ε_{xx}, their effects almost completely cancel out when the average is taken. Our calculated (unpolarized) SDR spectrum, displayed in fig. 3.6, appears in fact to be very little affected by the local fields, in the whole energy range between 0 and 6 eV. However, if a polarized SDR spectrum is computed, then local fields are found to influence the low-energy region ($\leq$ 2 eV), in a way which is very similar to the behavior of the RAS.

Unfortunately, it is not possible to perform here a comprehensive comparison with RAS and SDR experimental data, since this would require the calculation of several possible reconstruction and geometries. In fact, the oxidation mechanism of Si(100) has been shown to be exceedingly complex, with different mechanisms playing their role depending on the oxidation temperature: a barrierless oxidation of the first Si layer [66], or an “active oxidation” involving etching of the surface and penetration of oxygen in a layer-by-layer manner at higher temperature [89, 90, 91]. Recently, the Si(100)(2x1):O surface optical anisotropy has been shown to be sensitive to the structural details of the oxygen adsorption by ab–initio calculations of the atomic geometries and optical response of a large number of Si(100):O structures [92, 93]. An highly structured potential energy surface has been found, with minima at the backbonds of the "down" atoms in Si–Si dimers [93]. Moreover, an appreciable amount of disorder is probably present after oxidation of the first Si monolayer, and the local strain induced by oxygen adsorption is expected to have a sizable impact on the optical anisotropy spectra [92].

However, our findings for LF effects in the single case studied here suggest an important general remark about surface optical spectroscopies. In fact, it is well known that, due to the large penetration depth of visible and UV photons, the surface–specific optical reflectivity signal is very small with respect to the bulk contribution. For materials with an isotropic bulk, the RAS spectroscopy has indeed been developed in order to extract the surface signal, by exploiting its anisotropy. A correct evaluation of the latter has hence the highest priority in theoretical calculations of surface optical spectra. The fact that crystal local fields are potentially able to alter significantly the surface optical anisotropy, at least below the bulk bandgap, should hence be kept in mind, particularly when the anisotropy of electronic states is associated with a large structural anisotropy at the surface, such as in the case of dimer chains on Si(100)(2×1).

3.4 Computational scaling and performances

In this section, we present a quantitative analysis of the numerical performance of the HT-based approach, as implemented in the large scale code DP [78], with respect to the traditional approach. Several calculations have been done by varying the three main convergence parameters: (i) the number of valence–conduction transitions ($N_t = N_{\mathbf{k}} \times N_v \times N_c$); (ii) the number of frequency intervals considered in the spectrum, i.e. the spectral resolution (number of frequencies, N_ω); (iii) the number of plane–waves considered in the response matrix ($N_{\mathbf{G}}$). Optical properties usually converge at an $N_{\mathbf{G}}$ value which can be substantially smaller than the total number of plane waves, N_g, used to describe the wavefunctions.

The calculation of $\chi^{(0)}$ is expected to scale, in the case of the reference approach, as [5]:

$$T_{ref} = N_{\mathbf{k}} \left[\alpha N_v N_c N_g \log N_g + \beta N_v N_c N_{\mathbf{G}}^2 N_\omega \right] + \mathrm{A} \tag{3.21}$$

where $N_{\mathbf{k}}$ is the number of **k**-points, and α and β are prefactors which are independent on $N_v, N_c, N_{\mathbf{G}}, N_{\mathbf{k}}, N_g$, and N_ω. The first term in equation (3.21) is due to the evaluation of the numerators Z_n in equations (3.14) and (3.16) by using FFT, and is present both in the reference and Hilbert approach. The second term stems from to the evaluation of equation (3.11) in the traditional way. The remaining term A keeps into account residual parts of the calculation, as the matrix inversions, which contribute much less to the CPU time than the first two terms.

The expected scaling in the case of the Hilbert-based scheme is instead:

$$T_{new} = N_{\mathbf{k}} \left[\alpha N_v N_c N_g \log N_g + \beta' N_v N_c N_{\mathbf{G}}^2 \right] + \gamma N_{\mathbf{G}}^2 N_\omega^2 + \mathrm{A}' \tag{3.22}$$

In this case, the second term does not contain the factor N_ω anymore, and its prefactor becomes β', due to the calculation of χ^{A2} and χ^{R2} (equations 3.14 and 3.16). The calculation becomes, in this sense, comparable to a static one.

However, the actual evaluation of the Hilbert transforms (equations 3.18 and 3.19) introduces a new term scaling as $N_{\mathbf{G}}^2 N_\omega^2$. Due to the small prefactor γ, the latter term can often be neglected (see, e.g., figure 3 of reference [43]). In the present work, we found that the CPU time spent inside the Hilbert transform itself can be made negligible by an optimized algorithm[6].

Considering an N-atoms unit cell, the number of transitions N_t is clearly the parameter growing fastest with the system size, since it is proportional to N^2. About 22000 transitions per **k**-point, corresponding to the inclusion of about 200 empty bands, are requested to converge the dielectric tensor of the Si(100)(2x2):O slab up to 12 eV. The number of frequency intervals, N_ω, is instead independent on N, but it grows linearly with the required spectral resolution. In the present case, 300 frequencies have been necessary in order to achieve a 40 meV resolution over a spectral range of 12 eV. Finally, $N_{\mathbf{G}}$, i.e. the size of $\chi^{(0)}$ in reciprocal space, depends on the requested real-space resolution needed in the description of the induced density variations. This means that larger $N_{\mathbf{G}}$ will be necessary to describe systems with smaller interatomic distances, or with larger polarizability. The real-space resolution is independent on the system size; however, for a fixed resolution

---

[5] $N_t N_{\mathbf{G}}^2$ leads to the N_{at}^4 scaling mentioned in the introductory section.

[6] Exploiting the fact that the principal value numerical integration routine has to be called $N_{\mathbf{G}}^2$ times, always on the same energy intervals, a substantial gain could be achieved by tabulating the (about 10^6) required values of the complex logarithm once and for all at the beginning of the double loop over the number of **G** vectors in the construction of $\chi^{(0)}$.

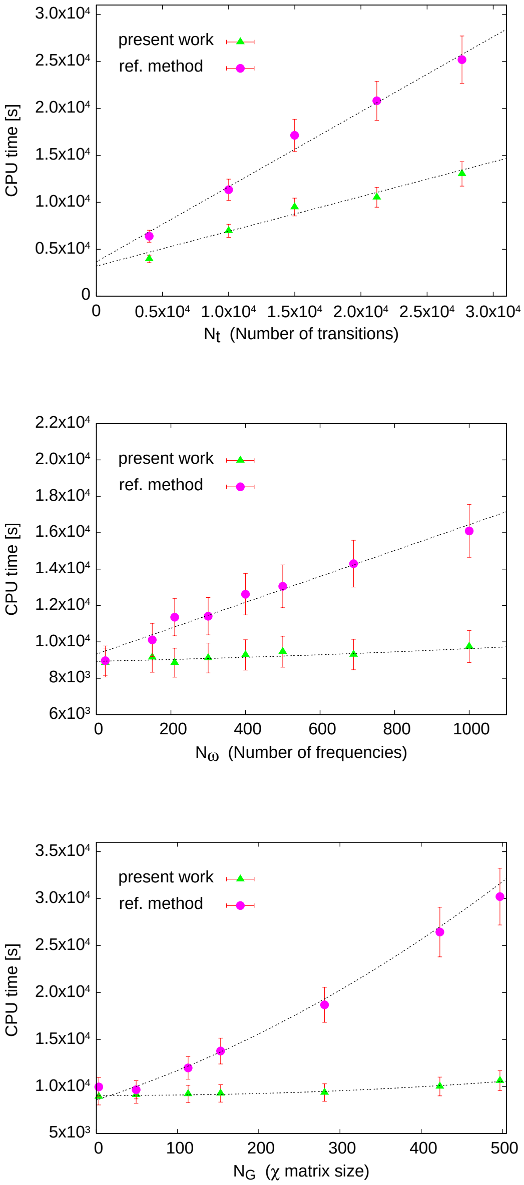

Figure 3.7: Quantitative study of the computational load required to evaluate the $\chi^{(0)}$ matrix for the 56-atoms slab representing a Si(100)(2x2):O surface. The effects of the three main parameters determining the numerical convergence of the theoretical spectra are studied separately. (a): number of valence–conduction transitions, determined by the energy cutoff on the empty (conduction) bands included in eq. (3.8), the number of occupied bands being fixed; (b): number of frequency intervals taken on the ω axis, determined by the requested spectral resolution; (c): size of the $\chi^{(0)}$ matrix in reciprocal space, roughly proportional to the system size (for a fixed real-space resolution).

$N_{\mathbf{G}}$ will grow linearly with the volume of the unit cell in direct space. $N_{\mathbf{G}}$ is hence proportional to the number of atoms (in a bulk system) or to the volume of the supercell (for a finite or semiinfinite system). In our slab calculation, converging the spectra with local field effects requires to consider at least 113x113 matrices (incidentally, we stress that the IP-RPA spectra, requiring just the $\mathbf{G} = 0$, $\mathbf{G}' = 0$ matrix element of $\chi^{(0)}$, do not depend on $N_{\mathbf{G}}$).

The HT algorithm turns out to be clearly advantageous with respect to N_t and $N_{\mathbf{G}}$, as shown in the first and last panels of figure 3.7. Concerning N_ω, despite an unfavorable scaling in the limit of infinite spectral resolution (the CPU time grows quadratically with the number of frequency intervals), one must notice that, due to the small prefactor γ, the HT method is largely convenient in whole range of interest ($N_\omega \simeq 10^3$).

3.5 Conclusions

Two classes of conclusions can be drawn from the presented results. First, the physics: the study of Si(100)(2x2):O has shown that local field effects, although playing only a minor role on the surface optical properties above the bulk bandgap, are able to enhance substantially the surface optical anisotropy in the low–energy end of the spectra. A similar effect can be expected for other surfaces, when the anisotropy of electronic states is associated with a large structural anisotropy, such as in the case of the dimer chains on Si(100)(2x2). Moreover, large local field effects are found for light polarized normally to the surface. Second, the numerics: the computational gain achievable by using the Hilbert transform-based algorithm has been shown to be substantial, both in a model system *and* in a real, physical application. A successful implementation of the Hilbert transform method in the large-scale plane-waves *ab initio* computer code DP [78] allows us to locate the crossover (starting from which the Hilbert transform algorithm becomes convenient) already at medium size systems (less than 50 atoms).

Part III

Applications

Chapter 4

The clean Si(100) surface

Surfaces are complex physical systems that are very important from both the fundamental and technological point of view. One of the most important surfaces of all is the (100) surface of silicon, as it appears in most electronic devices. Nevertheless, in spite of its many applications, a completely unambiguous structural and physical description of Si(100) is lacking. In this chapter we summarize our results about first principles calculations of electron energy loss spectra of the Si(100) clean surface.

4.1 Si(100): which reconstruction?

Due to its enormous technological importance, the Si(100) surface has been the subject of a wide range of experimental and theoretical studies spanning several decades. In fact, quality publications continue to appear regarding the atomic structure and electronic properties of the clean surface. Following early LEED experiments [94], it was understood that Si(100) forms a $p(2 \times 1)$ reconstruction. The classic explanation of the LEED observation is that the surface is composed of rows of Si dimers separated by trenches (Fig. 4.2), as confirmed by various scanning tunnelling microscopy studies [95, 96]. Although some quantum chemistry studies have found that a symmetric dimer structure (causing a metallic surface) forms the global minimum [97], several total energy calculations based on density functional theory [98] have found that dimer buckling induces a small energy gain, such that the dimers adopt an asymmetric configuration and the surface remains semiconducting [99].

Three distinct structures have been proposed for the Si(100) surface: the $p(2\times1)$, whereby all dimers are buckled the same way (see Fig. 4.2(a)); the $p(2\times2)$ structure, where alternating dimers in a row are buckled in opposite directions, and adjacent rows are buckled in phase (see Fig. 4.2(b)); the $c(4\times2)$ phase, being the same as the

$p(2 \times 2)$ but with adjacent rows buckled out of phase (see Fig. 4.2(c)). Total energy calculations have found [98] that the $p(2\times 1)$ reconstruction is prohibitively higher in energy than the other two (at zero K), and that the $c(4\times 2)$ is only slightly favoured over the $p(2 \times 2)$. Which reconstruction occurs on the surface depends critically on the temperature. LEED studies have shown that an order-disorder phase transition occurs at about 200K [100, 101]. Below this critical temperature, a $c(4 \times 2)$ phase is generally observed; above it, a $p(2 \times 1)$ periodicity is seen. Direct observation of the surface structure with STM is complicated by two factors however. Firstly, it is well established now that the experimental measurement itself can influence the result, and drive $c(4\times 2)\rightarrow p(2\times 2)$ phase transitions [102, 103]. Charge injection, or electric fields induced by the STM tip, can cause dimers to flip, according to various experimental [104, 103] and theoretical works [105, 106]. Nevertheless, the general consensus is that the $c(4 \times 2)$ reconstruction is the more stable structure below the critical temperature [103, 107].

Above 200K, STM images appear to show a symmetric dimer configuration. However, at these temperatures the dimer rocking mode is activated, and hence it is believed that the observed symmetric $p(2 \times 1)$ structure is merely a time average of the thermal flip-flop motion of the buckled dimers. Based on molecular dynamics simulation of the dimer motion, it was suggested that the surface consists of simultaneous local presence of asymmetric dimers, and of instantaneously flat symmetric dimers [108]. More recent studies have suggested that the dimers remain short-range correlated (see refs. 32–35 in Ref. [109]). In particular, a two photon photoemission (2PPE) study found minor difference between the surface band dispersion at 90K and at room temperature [110].

Theoretical simulations of the reflectance anisotropy (RA) spectra confirm that the $p(2 \times 1)$ reconstruction does not reproduce correctly the experimental lineshape [111, 112, 113]. On the other hand, both $c(4 \times 2)$ and $p(2 \times 2)$ structures are quite similar to the experiment, with the $c(4 \times 2)$ yielding a slightly better agreement [111], in particular predicting the observed SDR structure below 1 eV. Simulation of the surface differential reflectance also favours the $c(4\times 2)$ surface [114].

In addition to optical techniques such as RAS or SDR, electron energy loss spectroscopy (EELS) in the reflection geometry (REELS or RELS) offers an enhanced surface sensitivity and easy access to a wide energy range (see chapter 2). Although the majority of literature considering REELS of Si(100) has focused on vibrational properties [39], several studies have examined the nature of electronic states at the clean Si(100) surface [115]. Indirect information about surface states was derived from related studies looking at the changes in the REEL spectrum following oxidation [116, 117, 118]. High resolution (HREELS) measurements were carried out by Farrell *et al.* [119] and Gavioli *et al.* [120]. In the latter work, tight binding calculations were performed on the $p(2 \times 1)$ symmetric and asymmetric dimer models, and suggested that a mixture of the two structures was necessary to explain the room temperature EEL spectra. However, the $c(4 \times 2)$ structure was not considered in that work, and therefore some of the conclusions reached are not complete.

In the following sections, we present a computational study of high resolution EELS for the different reconstructions of Si(100): $p(2 \times 1)$, $p(2 \times 2)$ and $c(4 \times 2)$Ẇe consider the energy range that probes the excitation of interband, i.e., about 0–6 eV, and hence connect the experimental observation directly with the atomic structure and microscopic electronic response.

4.2 First principle scheme

We use density-functional theory within the local density approxiation (DFT-LDA), within a plane-wave and pseudopotential framework. The ABINIT [121, 122] and quantum-espresso/PWSCF [123] codes were used for computing the relaxed atomic structures, electronic bandstructures, and Kohn-Sham eigenvalues and eigenvectors required for the evaluation of the optical properties. However, in order to be consistent and since we found only minor differences between spectra computed with the two codes, we report only the final results obtained using the output of PWSCF. For all our calculations we used standard norm conserving pseudopotentials of the Hamann type [21] for both silicon and oxygen generated with FHI98PP package [124] within DFT-LDA (Perdew-Zunger parametrization [7]) framework.

4.3 Geometric structure

Even if a 7.5 Ha kinetic energy cutoff is rasonable in order to treat the case of a clean silicon surface, we used a 15 Ha cutoff throughout, as was previously found to be sufficient for oxidized Si(100) with the same pseudopotential [67]. The effect of the two cutoff is shown in Fig. 4.1 where it is clear that the minimum of the curve is not appreciably different.

Therefore we used the theoretical lattice constant of 5.393 Å, as determined at 15 Ha A standard repeated-slab and supercell approach was adopted in order to model the surface structure.

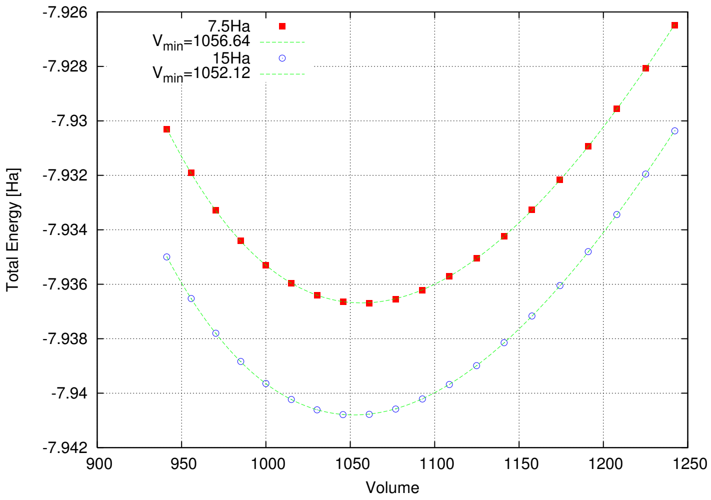

Figure 4.1: Optimization of the lattice parameter of bulk silicon at 7.5 Ha and 15 Ha cutoff energy.

We use relatively thick slabs (16 atomic layers) separated by 8 layers of vacuum

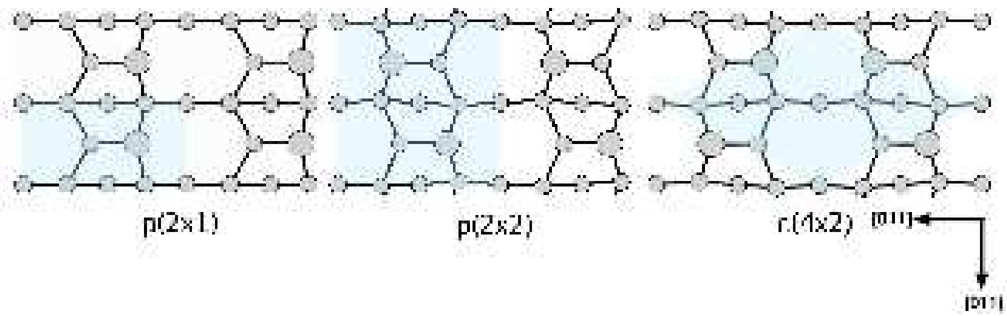

Figure 4.2: Ball and stick model of $p(2 \times 1)$, $p(2 \times 2)$ and $c(4 \times 2)$ surface reconstructions. Large circles indicate “up” silicon dimer atoms. Unit cells are indicated by shaded regions.

(about 10 Å). During the geometry optimization, the central four layers were fixed at the bulk positions and structures were relaxed until the cartesian force components were less than 20 meV/Å. Our obtained structural parameters are similar to those obtained previously for this surface (see for example Ref. [111]) such as a dimer buckling of 0.755 Å and a dimer length of 2.33 Å.

4.4 Computational aspect

Optical spectra and energy loss spectra were calculated using the YAMBO code [125], taking Kohn-Sham eigenvalues and eigenvectors from a non-self-consistent run of the PWSCF code [123]. We carried out convergence tests on the optical and energy loss properties with respect to the number of bands and the number of **k**-points. For the calculation of energy loss we included up to 320 unoccupied bands, corresponding to minimum *e–h* transition energy of ∼ 13.5 eV. Further convergence tests were carried out regarding **k**-point sampling. For the most converged calculations, we used roughly equivalent density sets for the three reconstructions: for the $c(4 \times 2)$, 72 **k**-points in the irreducible Brillouin zone (IBZ), which is equivalent to 1152 points in the (1×1) BZ (for both clean and oxidized cells, see next chapter); for the $p(2 \times 2)$, 64 **k**-points in the IBZ (equivalent to 1024 points in the (1×1) BZ); for the $p(2 \times 1)$, 100 **k**-points in the IBZ (equivalent to 800 points in the (1×1) BZ). All spectra reported in this work were obtained using the non-interacting particle (RPA) level of theory. Many-body effects, including local field and excitonic effects, were compensated for by applying a scissors operator of +0.5 eV to the unoccupied states, following the recipe of Del Sole and Girlanda [37]. In this way we account for the well-known underestimation of the DFT band-gap, and partially include self-energy and excitonic shifts in energy. The value of +0.5 eV was determined in other works on Si(100) as giving best agreement with the experimental RAS [67].

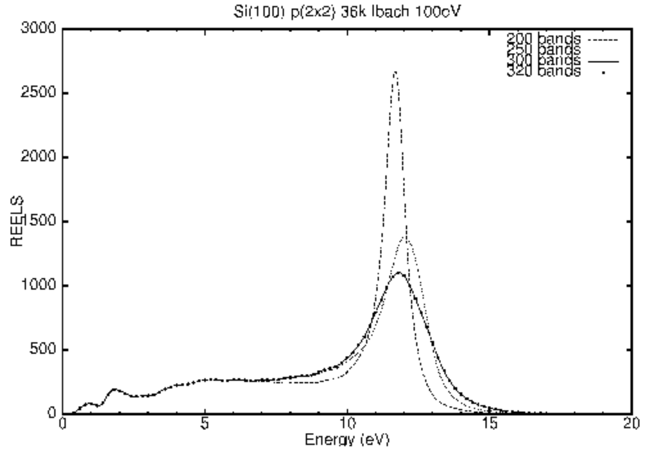

Figure 4.3: EEL spectrum of the clean Si(100)-p(2×2) surface calculated for incident energy E_i=100eV and $\theta = 42$. The height of the surface plasmon peak is mostly affected by the convergence respect to the number of bands.

In the following subsection we present some discussion of major technical tools used in order to compute REELS.

4.4.1 Broadening

Inspection of Eq. 2.28 reveals that the cross section goes as $1/q^3$ as $\omega \to 0$. Hence any features appearing in the loss function Im $g(q_\parallel, \omega)$ at low energy can be dramatically enhanced by the kinematic factor. From the computational point of view this means that unphysical features may appear close to the origin if a Lorentzian broadening is used when calculating the surface dielectric function of a system with a small band gap. We adopt therefore a tiny Lorentzian broadening of $\delta_L = 0.006$ eV when calculating the dielectric function, and afterwards convolute the loss spectra with a Gaussian (FWHM = 0.3 eV) to approach the experimental resolution.

4.4.2 Slicing methods

A crucial adjustable parameter present within the three-layer model of energy loss is the thickness d of the surface layer, as used in Eq. 2.30. According to the model, an electron impinging on the surface feels the potential from this surface layer through its dielectric function ε_s as well as that of the bulk layer ε_b. Obtaining ε_s from the dielectric function of the slab or supercell ε_c is not trivial. However early efforts used a simple subtraction of the computed bulk dielectric function [37]:

$$I(\omega) = (N_b - 2N_s) d_l \varepsilon_b(\omega) + 2N_s d_l \varepsilon_s(\omega) \tag{4.1}$$

where I is the integral of the slab RPA dielectric susceptibility $\varepsilon(\omega, z, z')$ over z and z', d_l is the interlayer spacing, N$_s$ is the number of layers at each surface with dielectric function $\epsilon_s(\omega)$ and N$_b$ is the number of inner layers with bulk dielectric constant $\varepsilon_b(\omega)$. Unfortunatly this approach cannot always guarantee perfect cancellation of the bulklike layers in the supercell, and may lead to unphysical negative loss features. A better approach is to extract ε_s directly using a “cut off” function as described in chapter 2 or in Ref. [38]. Nevertheless, the choice of d remains somewhat arbitrary. In this work we define the lower bound of the surface layer corresponding to the actual penetration depth of the electron for the chosen incident kinetic energy, with the upper bound defined by the maximum extent of the slab charge density or a typical surface state wavefunction (see Fig. 4.5). This turns out to be roughly one atomic layer. We then checked that varying d by an atomic layer did not change the results too much. The dependence of the REEL spectra on the parameter d is illustrated in Fig. 4.5.

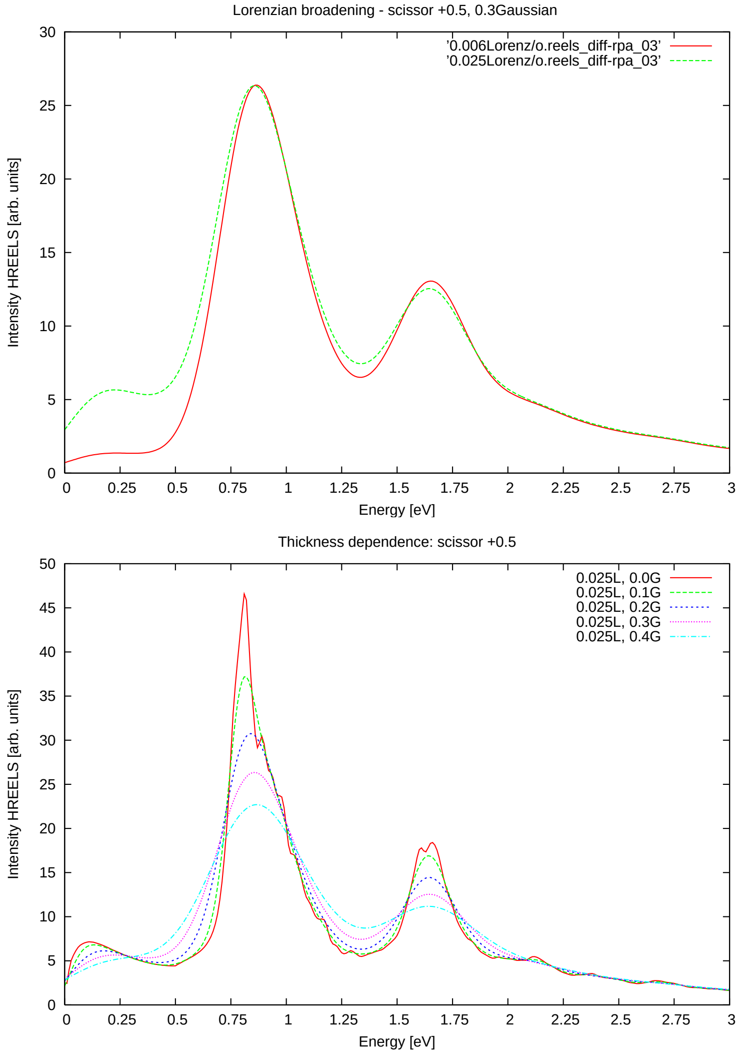

Figure 4.4: Effect of the Lorenzian broadening (top), effect of the gaussian convolution (bottom) on the EEL spectra of a Si(100)-c(4×2) surface (E_i=7 eV and θ =60).

4.4.3 Detector integration

In experimental EEL spectroscopy the detector has a finite acceptance angle for collecting the scattered electrons. Hence, in order to improve the quantitative estimation of the EEL spectra at the surface, we implemented a method to perform a numerical integration over the circular detector. In particular we account better for the finite size of the detector window through a random sampling of the circular

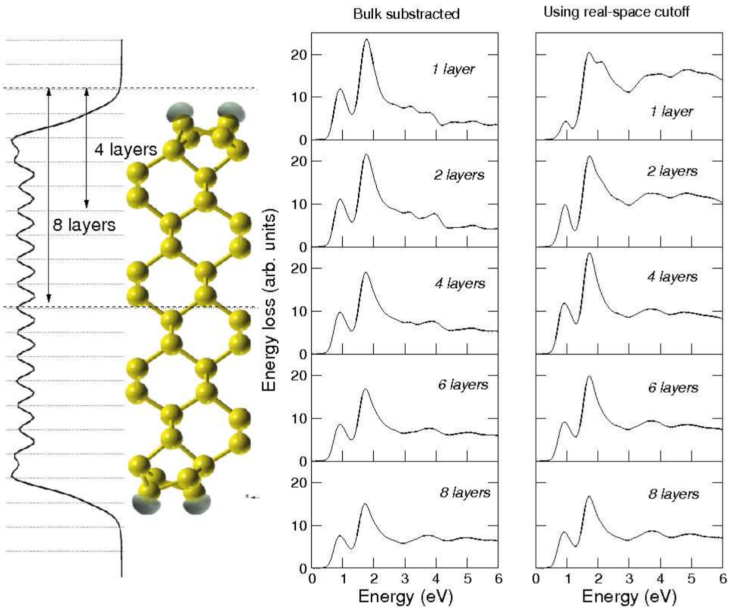

Figure 4.5: Schematic diagram of the Si(100)-$c(4 \times 2)$ slab and calculated layer averaged charge density (left); atomic layers are marked with horizontal lines. Dependence of REELS spectrum on the chosen surface layer (right).

area and in the computation of the following integral:

$$\int A(k,k')\mathrm{Im}g(q_{||},\omega)d\Omega \tag{4.2}$$

We implemented the method in the Yambo code [126], the code we used for all further calculations. In Fig. 4.7 an illustration of the importance of numerical detector

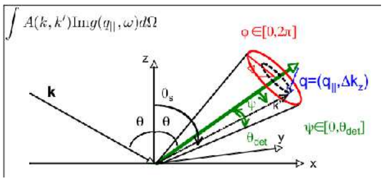
$\int A(k,k')\mathrm{Im}g(q_{||},\omega)d\Omega$
$\varphi \in [0,2\pi]$
$q=(q_{||},\Delta k_z)$
$\psi \in [0,\theta_{det}]$
z
k
θ_s
θ
θ
k'
θ_{det}
y
x

Figure 4.6: Integration geometry.

integration scheme with regard to relative intensity of peaks is shown. A frequently used technique is to approximate the integral by an averaged value of the transferred momentum $\mathbf{q}$.

$$\int d\Omega \rightarrow \int d\mathbf{q}$$

$$\int f(q)d\mathbf{q} \simeq f(\bar{q})$$

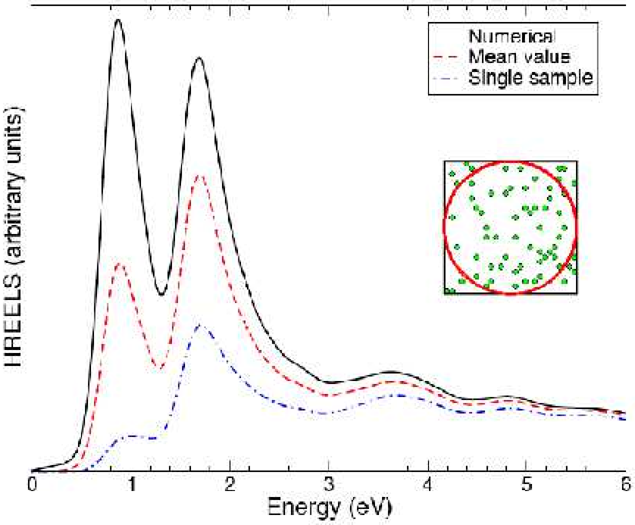

Figure 4.7: Dependence of REEL spectra on detector integration method: numerical Monte Carlo, mean value scheme, and single point sampling. Example shown for $c(4 \times 2)$ surface, $E_0 = 40$ eV; $\theta_0 = 60°$; $\theta_{\text{det}} = 1°$..

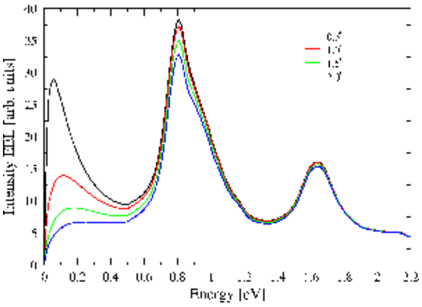

Figure 4.8: Dependence of REEL spectra on the detector size.

A comparaison between the two methods is shown in figure 4.7 where relative intensity of the low energy peaks is corrected with converged numerical integration. We also add a figure showing the effect of the detector size on the EEL spectrum.

4.5 Calculated spectra for Si(100)

A review of the current understanding of the structure of the clean Si(100) surface was given in the introduction and a schematic diagram of the three basic surface reconstructions (the $p(2 \times 1)$, $p(2 \times 2)$and $c(4 \times 2)$) is given in Fig. 4.2. Throughout this work we will refer to the $[01\overline{1}]$ direction as x and the $[011]$ direction as y, with $[100]$ being the surface normal z. Here we present our results concerning optical and electronic spectroscopic study of the clean Si(100) surface.

4.5.1 Reflectivity anisotropy spectra

Several theoretical studies of the RA spectra for the Si(100) surface have previously been carried out, including tight binding calculations [127], discrete-dipole models [128, 129], *ab initio* calculations at the independent particle level [130, 131, 132, 114, 67, 112, 113] as well as more recent studies including many-body effects [133]. Generally it was found that the best agreement with the experimental RA data [36] is obtained when the $c(4 \times 2)$ or $p(2 \times 2)$ models are used in the calculations, while the $p(2 \times 1)$ gives poor agreement.

Since we will use the same optical dielectric functions when computing the energy loss spectra, we show for completeness (in Fig. 4.9) the results of our own supercell calculations for the $c(4\times 2)$, $p(2\times 2)$ and $p(2\times 1)$ reconstructions at the independent particle level. The reflectance anistropy (see chapter 2) is defined as

$$\mathrm{RAS} = \frac{\Delta R_x}{R} - \frac{\Delta R_y}{R}, \tag{4.3}$$

where $\Delta R_i/R$ $(i = x, y)$ is the normalized reflectivity (i.e., relative to the Fresnel reflectivity).

As expected, we find that both $c(4\times 2)$ and $p(2\times 2)$ spectra yield a good agreement with the experimental data.

The $p(2\times 1)$ reproduces the low energy peak at 1.5 eV rather well, but the comparison worsens at higher energy. Unfortunately, no experimental data is available for the RAS of Si(100) in the near-IR range, and is hence limited to >1.1 eV.

4.5.2 Calculated REELS spectra at $E_0 = 40$ eV

We now contrast the RAS results with the theoretical simulation of the HREELS experiment of Farrell *et al.* [119] with incident energy of $E_0 = 40$ eV, which roughly covers the same spectral range as the available RAS data. Experimental results refers to specular geometry with incident angle of $\theta = 60°$.

There exists a one-to-one correspondence between RAS and HREELS that can be justified with theoretical arguemnts when we consider a spectral range below E_1. In fact it can be written that RAS is proportional to $\mathrm{Im}\varepsilon_s$ when $\mathrm{Im}\varepsilon_b$ is close to zero. On the other hand:

$$\mathrm{Im} g(q, \omega) \simeq \mathrm{Im}\left[\frac{1}{1+\varepsilon_s}\right] \simeq \frac{\mathrm{Im}\varepsilon_s}{(1+\mathrm{Re}\varepsilon_s)^2 + \mathrm{Im}\varepsilon_s^2} \tag{4.4}$$

giving a direct proportionality of REEL respect to $Im\varepsilon_s$. This correspondence is evident in Fig. 4.14 where HREEL peaks and $\mathrm{Im}\varepsilon_s$ are represented. The experimental one-to-one correspondance between RAS and HREELS was also previously

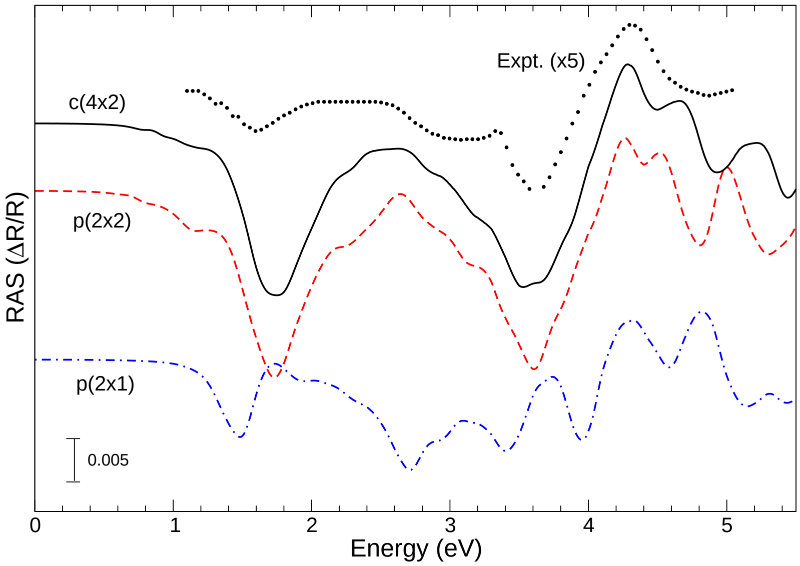

Figure 4.9: RAS spectra of the $c(4 \times 2)$, $p(2 \times 2)$ and $p(2 \times 1)$ reconstructions of clean Si(100), compared with the experimental spectrum of the nominal surface (scaled by a factor of 5). Experimental data are taken from Ref. [36].

illustrated by Arciprete *et al.* [134] for the case of GaAs(001)-$c(4 \times 4)$.
The experimental data, which are reproduced in Fig. 4.10, are characterized by surface-derived soulder at 0.9 eV (S_0) and a broad peak at 1.4-2.0 eV (S_1), and bulk-derived peaks at about 3.5 eV and 5 eV. The latter peaks have also been identified in second-derivative off specular geometry spectra at E_0=100eV by Rowe and Ibach [115] as deriving from the bulk critical points, E_1 and E_2. In the experimental spectrum of Fig. 4.10 we have subtracted a background signal, taken to be that of the monohydride Si(100)-$p(2 \times 1)$:H surface, also reported in Ref. [119].

The results of our first principles calculations of HREELS are shown in Fig. 4.10 for the $p(2 \times 1)$, $p(2 \times 2)$ and $c(4 \times 2)$ reconstructions of Si(100). From the comparison with experiment it is clear that the $p(2 \times 1)$ alone cannot reproduce the experimental signal since the shoulder at 0.8 eV (S_0) is missing from its theoretical spectrum. A similar observation was made by Gavioli *et al.* [120] based on tight binding calculations of the HREEL spectrum.
Moreover we observe that, as in the case of the RAS, it is difficult to distinguish between the $c(4 \times 2)$ and $p(2 \times 2)$ calculations. The S_0 peak appears at a slightly lower energy (by 0.1 eV) in the $p(2 \times 2)$ calculation; however, considering the approximations used in the present calculations (scissors shift), it is not sufficient to

allow us to prefer the $c(4\times 2)$ over the $p(2\times 2)$.

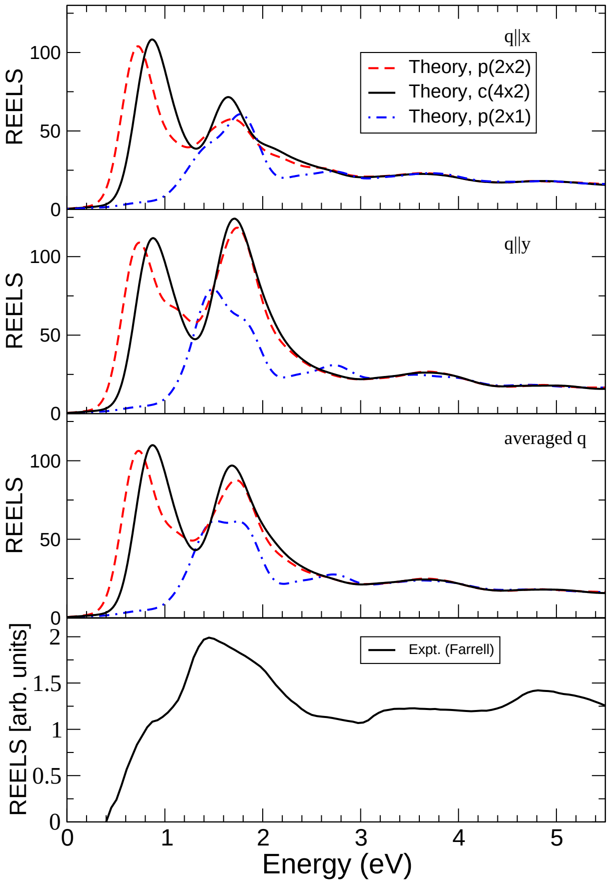

Figure 4.10: REEL spectra of $c(4\times 2)$, $p(2\times 2)$ and $p(2\times 1)$ reconstructions of clean Si(100), and comparison with experiment (Farrell *et al.* [119]): $E_0 = 40$ eV; $\theta_0 = 60°$. The surface thickness is assumed to be d = 8 layers (plus one vacuum), i.e., the half slab. A background signal has been subtracted from the experimental spectrum (see text).

As discussed in Section 2.2.4, the three-layer model of energy loss is based on the assumption that the electron does not penetrate the surface, so that losses occur from scattering off long range potentials above the surface.
In reality, electrons with a 40 eV kinetic energy actually penetrate the surface by several atomic layers before elastic scattering occurs. As a result, features in the loss which arise from scattering within the crystal itself (as occurs naturally in transmission EELS) are missing from our theory. Hence the calculated lineshape differs significantly from the experimental one above 2.5 eV.

To counteract this deficiency of the theory, we augment the reflection loss term with a second loss term that represents the trasmission loss, or "bulk" loss within the subsurface layers:

$$g(q,\omega) = g^{3\mathrm{L}}(q,\omega) + K|q|\frac{-1}{\varepsilon_b} \tag{4.5}$$

The result is shown in Fig. 4.11. Since the three-layer model already accounts well for losses in the surface layer (the spectra presented here actually do not change much if a loss function of the form $-1/\varepsilon_s$ is used), we find we only need to increase the proportion of bulklike losses below the surface to improve the agreement with experiment.

In spite of the agreement reached it is clear from the relative intensity of the S_0 and S_1 peaks that one single reconstruction cannot reproduce the experimental spectra.

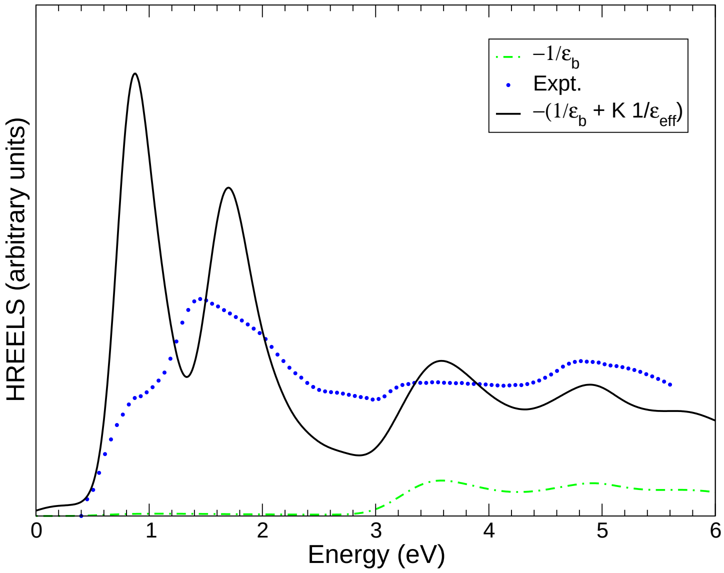

Figure 4.11: REELS spectra of $c(4 \times 2)$ calculated using a mixture of long range reflection and short range transmittion loss functions, compared with experiment (Farrell *et al.* [119]): $E_0 = 40$ eV; $\theta_0 = 60°$.

4.5.3 Calculated REELS spectra at low energy

Although many REEL spectra are present in the literature that study the Si(100) surface, only a few high resolution spectra that probe the interband transitions of Si(100) are available.

We reproduce in Fig. 4.12 the HREELS data for low-energy incident electrons reported by Farrell *et al.* [119] ($E_0 = 7$ eV; $\theta_0 = 60°$ specular scattering; probably at T=300K) and Gavioli *et al.* [120] (for a slightly different experimental setup: $E_0 = 6.8$ eV; $\theta_0 = 62.5°$; T=120–500K).

In both works, two main structures are identified in the spectra below 2 eV. Farrell reports an adsorption edge at 0.4 eV with a peak at 0.75 eV (termed S_0), and a

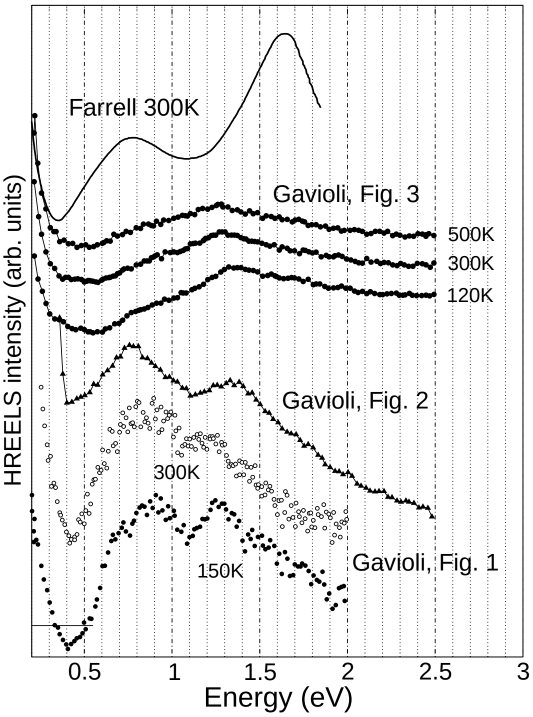

Figure 4.12: HREELS experimental data from Farrell (solid line: $E_0 = 7$ eV; $\theta_0 = 60°$; 300K) and Gavioli (dots: $E_0 = 7.8$ eV; $\theta_0 = 62.5°$; 150K and 300K).

second edge at 1.1 eV with a peak at 1.65 eV (termed S_1). We note that the S_1 peak was identified by Farrell as being the peak observed by Ibach and Rowe [115, 117] at 1.7 ± 0.5 eV and by Maruno *et al.* [135] at about 2.0 eV. In the more recent work by Gavioli *et al.*, various HREELS data were reported at temperatures ranging from 120 to 300 K, and at different analyzer focalizations (see Fig. 4.12). At low temperature a shoulder is found at 0.68 eV, as well as two main structures at 0.9 eV and 1.15–1.35 eV. It is not clear, however, if the latter feature corresponds to the S_1 structures reported elsewhere, as any peaks appearing at around 1.7 eV in Gavioli's data seem to be obscured by the background noise. Note that the main low energy peak occuring in the RAS is at 1.6 eV, as seen in Fig. 4.9, which would appear to agree with the peak positions of Farrell *et al.*. In Fig. 4.13 we report the results of our *ab initio* simulation of this HREELS experiment. As noted for the $E_0 = 40$ eV data, it is clear that the $p(2 \times 1)$ model does not yield the correct lineshape, as the S_0 peak is missing. Both $c(4 \times 2)$ and $p(2 \times 2)$ structures succeed in reproducing the double-peaked structure observed in the experiments. In particular, the S_0 peak is well reproduced by the $c(4 \times 2)$ model, and it is possible that the shoulder observed at 0.68 eV points to the coexistence of some $p(2 \times 2)$ on the predominantly $c(4 \times 2)$ surface. The calculated energetic position of the S_1 peak is in reasonable agreement with the data of Farrell, but not so much with that of Gavioli. However, it is worth

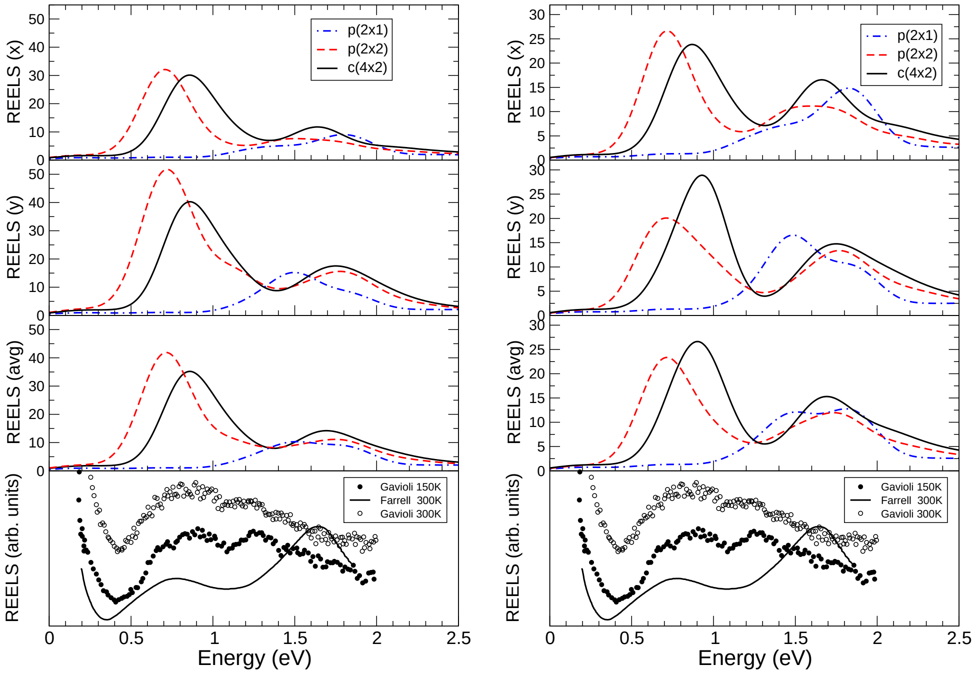

Figure 4.13: REEL spectra of $p(2\times1)$, $p(2\times2)$ and $c(4\times2)$ reconstructions of clean Si(100), for low energy incident beam ($E_0 = 7$ eV; $\theta_0 = 60°$). Left: Surface thickness $d = 4$ atomic layers; Lorenztian broadening $\delta_L = 0.006$ eV; Gaussian broadening of $\delta_G = 0.3$ eV. Right: Surface thickness $d = 2$ atomic layers.

to mention that Farrell's data beyond 1.5 eV can be affected to background and are not completly relible because some fit of experimental data has been performed and in the original paper the dashed line at that energies give us some doubts on the exact position of that peak. For this reason we feel more confident in the more recent Gavioli's data.

4.5.4 Analysis of spectra

In the following two sections we concern ourselves with interpreting the experimental peaks observed in the HREEL spectra below 3 eV for the kinematic setup of Farrell and Gavioli at $E_0 \approx 7$ eV.

Fig. 4.14 compares the calculated surface dielectric function with the calculated HREEL spectra.

It is clear that there is a one-to-one correspondance between peaks in the energy loss and peaks in the imaginary part of the dielectric function. Hence we can analyse ε_2

to characterize peaks in the HREEL spectra. The experimental spectra feature two main peaks, termed S_0 and S_1 in the literature [119]. The microscopic origins of these peaks is now analysed for the $c(4 \times 2)$ reconstruction. Figures 4.15 and 4.16 show the total oscillator strength $\overline{P_E}(\mathbf{k})$, as a function of $\mathbf{k}$, corresponding to an energy window of width 2δ centred around a chosen peak energy E:

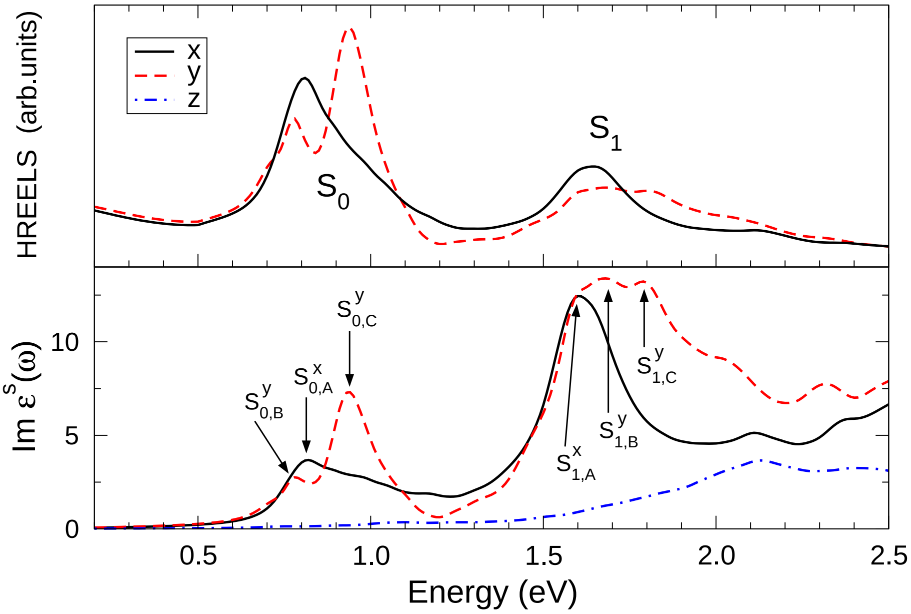

Figure 4.14: HREEL (along x, y) spectra (top) and surface dielectric functions (x, y, z) for $E_0 = 7$ eV, $\theta_0 = 60°$.

$$\begin{aligned} \overline{P_E}(\mathbf{k}) &= \sum_{v,c} |P_{v,c,\mathbf{k}}|^2 \\ \text{for} &\quad E - \delta < E_{c\mathbf{k}} - E_{v\mathbf{k}} < E + \delta. \end{aligned} \tag{4.6}$$

It is clear that S_0 arises from transitions located around the Γ point for both polarizations (see Fig. 4.15) On the contrary S_1 arises mostly from transitions along $\bar{Y}$–$\bar{Y}'$ direction.

The location of these transitions with respect to the surface band structure is shown in Fig. 4.18. Our bandstructure calculation for the clean $c(4 \times 2)$ surface compares well with that previously published by Fuchs [113]. In particular, a surface state is present at about 0.8 eV above the valence band maximum.

Finally, we looked at $|\psi_{n,\mathbf{k}}|^2$ for the valence and conduction band states taking part in the strongest transitions. These are plotted in Fig. 4.17 using Xcrysden package [136]. We found that S_1 derives from transitions between surface states:

dangling bonds and sp^2-hydridized p_z orbitals, or π to π^* orbitals as shown on Fig. 4.17. To have a confirmation of this statement an analysis of Fig. 4.16 and of the band structure (top of Fig. 4.18) is required. In fact, Fig.4.16 shows that the most part of transitions contributing to S_1 comes from k points along $\bar{Y}$–$\bar{Y}'$ path in the SBZ and the band structure clarify which bands are involved. In fact, looking at the band structure in Fig. 4.18 it is clear that S_1 peak comes from transitions between the flat bands in the $\bar{Y}$–$\bar{Y}'$ direction (blue arrows).

On the other hand, S_0 is due to transitions between bulk states at the valence band maximum (in Γ) and unoccupied surface states within the fundamental bulk bandgap. A representative pair of states involved in this kind of excitation is shown in Fig. 4.17 (top). Moreover, with a similar analysis as done for S_1, band structure and Fig. 4.15 (red arrow) give a confirmation of the fact that S_0 is more symetric involving transitions around the Γ point.

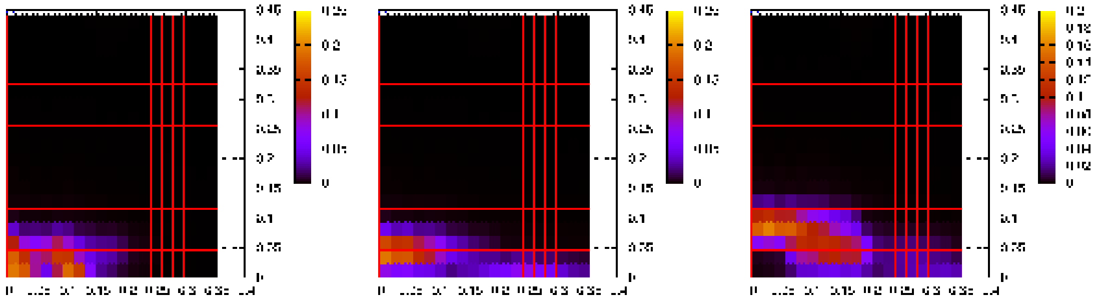

Figure 4.15: Total oscillator strenght $\mathrm{P}_E(k)(\delta E = 0.1eV)$ as a function of $\mathbf{k}$ contributing to S_0 peak. In particular we considered two perpendicular directions of polarization belonging the surface plane: X and Y respectively and we analysed 3 energy windows centred around the position of the peak in the surface epsilon (see Fig.4.14). In particular 0.32eV for x polarization (left) and 0.285eV (center) and 0.44eV (right) for y polarization, namely $\mathrm{S}_{0,A}$, $\mathrm{S}_{0,B}$ and $\mathrm{S}_{0,C}$ respectively.

4.5.5 Discussion

We now show how our HREELS calculations can be used to better understand the structure of the Si(100) surface as a function of temperature. Si(100) exhibits a $p(2\times 1)$ LEED pattern above the order–disorder transition temperature of about 200K. Our findings (Fig. 4.13)—that the $p(2 \times 1)$ surface alone model cannot reproduce the experimental HREELS data—are consistent with current understanding of the

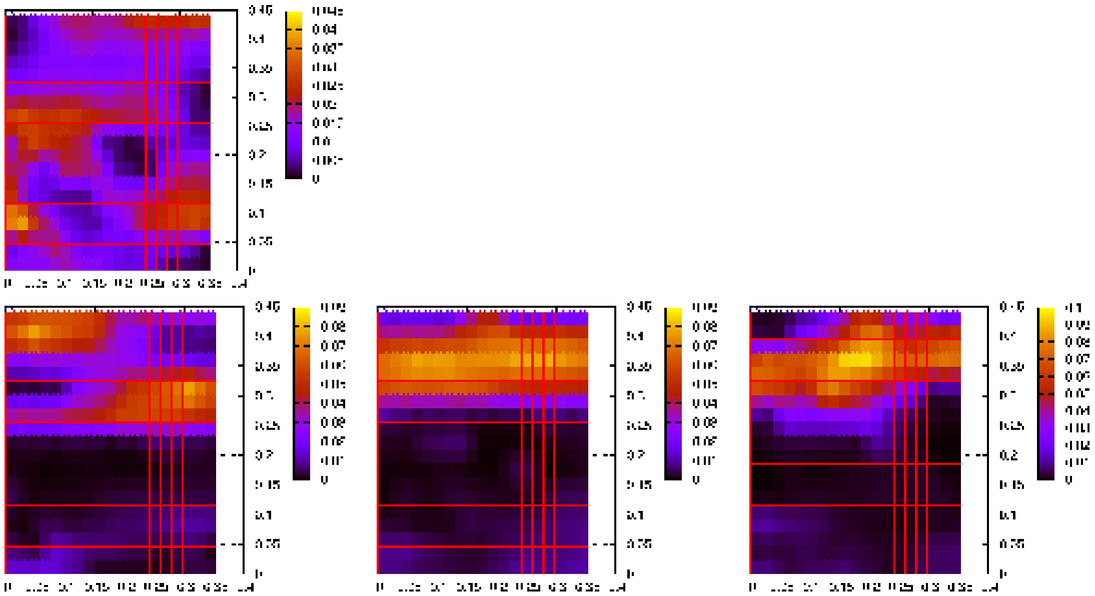

Figure 4.16: Total oscillator strenght $\mathrm{P}_E(k)(\delta E = 0.1 eV)$ as a function of $\mathbf{k}$ contributing to S_1 peak. In particular we considered two perpendicular directions of polarization belonging the surface plane: X (top) and Y (bottom) respectively and we analysed 3 energy windows centred around the position of the peak in the surface epsilon (see Fig.4.14). We considered 3 energy windows centred at 1.11eV (top), for x (left) and y (right) polarization respectively, and at slightly highier energies (bottom) 1.18eV (left) and 1.29eV (right) for y polarization, namely $\mathrm{S}_{1,A}$,$\mathrm{S}_{1,B}$, $\mathrm{S}_{1,C}$ and $\mathrm{S}_{1,D}$ respectively.

surface at this temperature (rapid dimer flipping). At lower temperatures, the surface should be predominantly $c(4 \times 2)$.

The experimental dependence of the HREEL spectra of Si(100) was studied by Gavioli *et al.* [120], and their results are reproduced in Fig. 4.12. In that work, the observed spectrum was explained as being due to a mixture of symmetric and asymmetric $p(2 \times 1)$ structures. However, there is much evidence to show that symmetric dimers do not exist at 150K. Furthermore, they did not consider the $c(4 \times 2)$ structural model, which we find is sufficient to produce a double-peaked HREEL spectrum (Fig. 4.13 and 4.10).

Increasing the temperature, the S_0 peak is found to decrease by 5% and the S_1 peak by 40%. As described previously, we took care to ensure that the calculated relative intensities of the peaks are not artefacts of our calculation, as we checked their con-

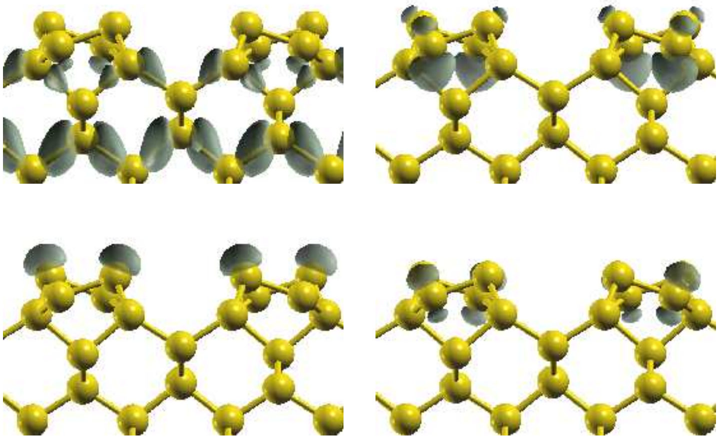

Figure 4.17: Isosurface plots of $|\psi_{n\mathbf{k}}(r)|^2$ for represetative states involved in transitions responsible for peaks in the low energy HREELS peaks S_0 at 0.8 eV (top) and S_1 at 1.6 eV (bottom). Plots are obtained using Xcrysden [136] package.

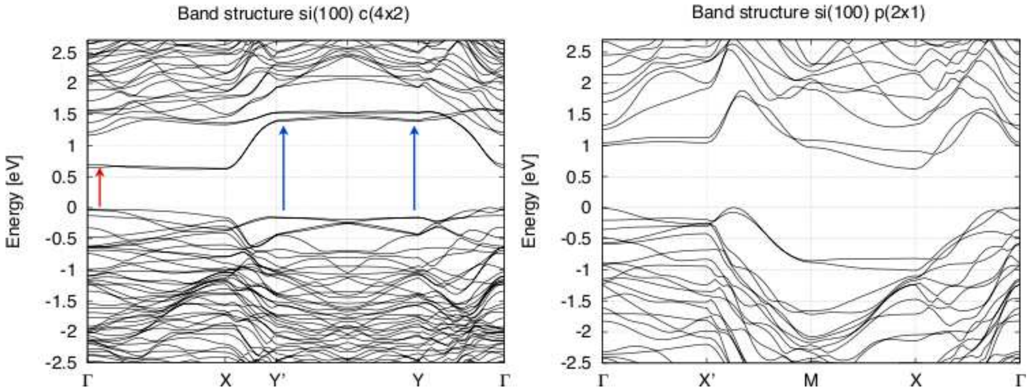

Figure 4.18: Band structure of the $c(4 \times 2)$ (left) with indication of surface peaks. Compare with $p(2 \times 1)$ (right) to show absence of surface band. A rigid scissor shift of 0.5eV has been applied to unoccupied bands.

sistency with respect to the lorentzian and gaussian broadenings, the surface layer thickness, detector integration settings, k-point sampling. We can only conclude, therefore, that the $c(4 \times 2)$ is not the sole reconstruction present at the surface.

Furthermore, we note that the $p(2 \times 1)$ spectrum does not contribute to the S_0 peak, on the contrary $c(4 \times 2)$ and $p(2 \times 2)$ have both some structure at that energies. Moreover, looking carefully at Fig. 4.13, it is possible to link the 0.68 eV shoulder in Gavioli's data at $T = 150°$ to the first peak of the $p(2 \times 2)$ structure and the 0.9 eV peak, present also in the $T = 300°$ curve, to the $c(4 \times 2)$ structure. At the end we mention that the position of the S_1 peak needs a correction in order to predict Gavioli's experimental value between 1.15 eV and 1.35 eV for the $p(2 \times 2)$ $c(4 \times 2)$ and $p(2 \times 1)$ structures. Spectra reported in this work, and the subsequent analysis, were carried out within the approximation of non-interacting particles (RPA), using the DFT-LDA eigenvalues and wavefunctions. A straightforward scheme for incorporating many-body effects is to apply a *scissor* operator to the unoccupied states, following the recipe of Del Sole and Girlanda [37]. In this way we compensate for the well known understimation of the DFT-LDA band gap, and partially account for self energy and excitonic shifts in energy. A scissor shift of +0.5 eV has previously been determined in other works on Si(100) [67] as giving the best agreement with the experimental RA spectra. We also confirm this result from a fit to the experimental data (see Fig. 4.9). Nevertheless, this value may not consistently describe the energetic positions of all surface state features, which generally undergo many body corrections different from bulk ones. In order to determine the correct correspondance between surface-related experimental and theoretical energy loss peak, we performed some preliminary calculations including many body effects on a smaller (12 layers) $c(4 \times 2)$ slab at a lower cutoff (12 Ry). Self energy corrections were computed within the so called GW approximation. Within this approach it is possible to solve self consistently a closed set of five equations (Hedin's equations [137]) connecting the Green function (G), the polarizability (Π), the screened Coulomb and vertex interactions (W and Γ) and the self energy (Σ). with the assumption $\Sigma = iGW$ and $\Gamma = 1$. Excitonic and local field effects were accounted for by means of solving the Bethe Salpeter equation (BSE), connecting the full Π with the non interacting Π^0 via a 4-points kernel.

Details of the approach are beyond the scope of this thesis, and can be found in Ref. [3]. Our preliminary calculations on HREEL spectra below 2.5 eV show in fact that GW+BSE approach give a better agreement with the experimental data of Gavioli *et al.* [120] while the RPA+scissor calculation give a misleadingly good comparison with the S_1 peak of Farrell *et al.* [119]. Thus the combined GW+BSE approach is nowadays the state of the art for computing precise optical spectra, nevertheless it is very expensive from the computational point.

4.6 Conclusions

We studied the RA and REEL spectra of the Si(100) surface modeling the surface with $p(2\times 1)$ $p(2\times 2)$ and $c(4\times 2)$ reconstructions. Our calculations of RA spectra are in agreement with previous works.

REEL spectra has been calculated for two experimental setup according to the available experimental data from Gavioli *et al.* [120] and Farrell *et al.* [119]. We confirmed that $p(2\times 1)$ cannot be the only reconstruction of the real surface because S_0 peak is completely missing in spectra and from a band structure analysis.
The origin of the S_0 and S_1 peaks has been carefully analysed considering the $c(4\times 2)$ model more rapresentative of the surface. We have seen that S_0 arises from transitions involving bulk states around Γ and surface states below the bandgap. On the contrary S_1 involves only surface states.
Moreover the 0.68 eV feature in Gavioli's data suggest some $p(2\times 2)$ present, along with $c(4\times 2)$ but the experimental analysis also suggests that temperature can largely change the structural reconstruction because termal motion can easly induce a flip-flop of the dimers.

In summary, we obtained several informations on the nature of the low energy excitations of the Si(100) surface and the joint theoretical and experimental REEL spectroscopy contributed to clarify the structural composition of this still debated surface.

Chapter 5

The oxidized Si(100) surface

There are two reasons why the investigation of REEL spectra of oxidized Si(100) is important. First of all, studying the changes in the experimental spectrum that occur after absorption of a foreign substance, such as oxygen or hydrogen, is a widely used technique for elucidating the character of spectroscopic features in the *clean* surface. From a theoretical point of view, it is not immediately apparent how spectral features related to surface states are modified following atomic scale modifications.

Secondly, a thorough understanding of the oxidation process on Si(100) at the atomic scale is of huge technological importance for the development of electronic devices and nanodevices [138].

In spite of an extensive study over several decades, including electron energy loss [116, 117] photoemission, RAS [139, 81, 80] and several theoretical investigations [67, 112, 113], there remains some controversy about the reaction pathways, with different works suggesting dimer breaking, insertion of O into dimer backbonds, as well as silanone bound (O)Si=O formation [32, 64].

In the present section we aim to identify "fingerprints" in the REEL spectrum that can help to distinguish between different adsorption sites during the initial stages of oxidation, and to obtain further information about the surface states of the clean surface.

5.1 Atomic structure

Among the vast experimental and theoretical work on oxidized Si(100), a number of recent theoretical studies [67, 112, 113] proposed various possible adsorption sites at low and intermediate coverages, and investigated the optical (RAS) and electronic

Structure	dimer bridge [Å]	dimer backbond [Å]
$c(4 \times 2)$ 1D	1.61	1.61
$c(4 \times 2)$ 1E'	1.78	1.75
Structure	dimer bridge [Å]	Si=O [Å]
$c(4 \times 2)$ 1D Si=O	1.61 , 1.70	1.53
$p(2 \times 2)$ 1D Si=O	1.63 , 1.73	1.55

Table 5.1: Structural lengths of the oxidized Si(100) surface referring to the configurations studied. All calculations are performed in LDA. 1D refers to oxygen in the bridge, 1E′ refers to oxygen in the backbond, Si=O refers to the silanone structure created on the top silicon atom of the dimer.

properties of these systems.

In this work we considered a wide range of oxygen adsorption sites that we can group according to the number of atomic oxygens involved: those with two atomic oxygens in the elementary cell will be referred to as low-coverage (0.5ML) structures; on the other hand, a coverage of 1ML will be described in our model by four oxygen atoms for cell.

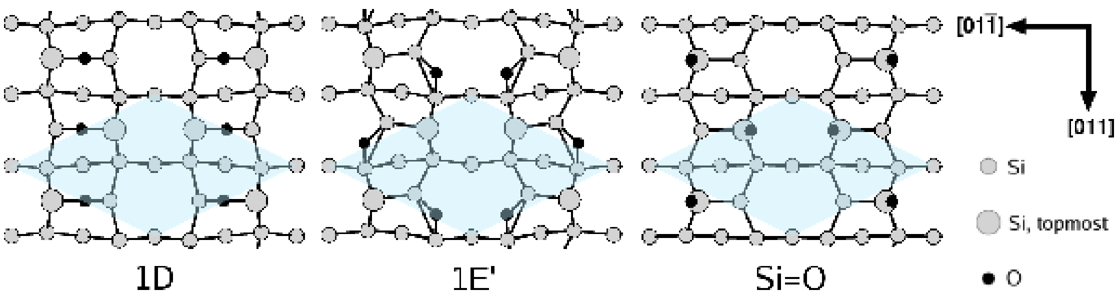

Figure 5.1: Schematic diagram of the 1E′, 1D models of the oxidized Si(100) surface. Large circles indicate “up” silicon dimer atoms; small filled circles are oxygen atoms. The $c(4 \times 2)$ unit cells is indicated by shaded regions.

Among the possible low-coverage structures, we choose to compute the REELS for three characteristic local structural motifs (nomenclature follows that of Ref. [112, 113]): structure 1D, with an oxygen inserted into the surface Si dimer, and structure 1E’, in which oxygen inserts into the dimer backbond and a silanone structure, whereby oxygen is bonded via a double bond to the silicon dimer. A schematic representation of these structures is given in Fig. 5.1. Both surfaces have a low total energy (see Table 5.2 and Refs. [92, 113, 140]) and for this reason they are good candidates to represent the real system. Regarding the silanone structure, we studied a configuration where oxygen is bonded to one silicon atom, as proposed by Hemerick *et al.* in [32] showing a critical formation of silanone species (O)Si=O during initial oxidation. Anyway, we found silanone structures being higher in energy when only two atomic oxygens for cell are considered (see structure "Si=O" with just two oxygens added to the clean $c(4 \times 2)$ base on top of a silicon atom of the dimer in Table 5.2).

Moreover, in the case of 1ML coverage, we considered several structures appeared in litterature, starting from both 1D or 1E' base configuration. First we studied the 1D base adding the oxygen on the backbond, resulting a $c(4 \times 2)$ 1D+1E' structure. Furthemore we considered one oxygen in the bridge and one added in the silanone bound because suggested in Refs. [32, 64], finding a relaxed structure with two silanone species, one free and the second connected to another silicon by a dative bond. We analyzed this "1D Si=O" structure built on both the $c(4 \times 2)$ and $p(2 \times 2)$ bases. The latter case is considered because the two oxygens on silanone bounds of adjacent dimers on the $c(4 \times 2)$ reconstruction are very close (see black circles in the central picture of Fig. 5.2). This is unlikely to occur in nature, because there would be extra strain on the surface since steric interaction pushes away adjacent oxygens. The $p(2 \times 2)$ Si=O structure (see Fig. 5.2) seems to be more reasonable for these reasons.

Table 5.2 shows a summary of the studied structures with corresponding total energies calculated. In order to compare the results, in case of the clean reconstructed surfaces we calculated the surface energy:

$$E_{\text{surf}} = \frac{1}{2S} \left(E_{\text{tot}}(N) - N E_{\text{bulk}} \right) \tag{5.1}$$

where N is the number of atoms in the slab, S is the surface cell area, E_{tot} is the total energy and E_{bulk} the total energy per atom of bulk Si. The surface with the smallest surface energy is the most stable one.

In case of the oxidized surface we reported the adsorption energy, i.e. the energy gain for adsorbing atom at the surface. This quantity is calculated as:

$$E_{\text{ads}} = -\frac{E_{\text{tot}} - E_{\text{clean}} - N_{\text{O}} E_{\text{free}}(O)}{N_{\text{O}}} \tag{5.2}$$

where E_{tot} is the total energy of the slab, E_{clean} is the total energy of the corresponding clean surface, $E_{\text{free}}(O)$ is the energy of the free oxygen and N_{O} is the number of oxygen atoms.

For all structures the inner four layers are fixed to the bulk positions, assuming they are not influenced by the surface distortions. Optimization is hence performed on the outer slab layers using the Broyden-Fletcher-Goldfarb-Shanno minimization (BFGS) [141, 142, 143, 144]. Crosschecks of results have been performed with PWscf and ABINIT codes [123, 122]. Because of complexity, the case of one oxygen in the backbond and one added in the silanone bond on top of the lower silicon atom of the dimer, needs a separate discussion. In spite of the fact that silanone structures have been suggested in the litterature (see Refs. [64, 32]), both from theoretical and experimental grounds, in the present work the total energies founded are relatively high for the structures reported up to now. Hence we tried to identify a low energy structure for a 1ML coverage that contains the silanone motif. Although there are specific techniques for doing such simulations, such as Car-Parrinello molecular dynamics, nudged elastic band simulations or potential energy surface mapping, we was able to identify one such structure by following a straightforward BFGS relaxation, starting from an undimerized Si(100) surface with Si=O bonds in the vertical plane. The eventual purpose is to identify any fingerprints in the REEL spectra that might correspond to such Si=O bonds (see sec. 5.3). In Fig. 5.3 the evolution of the total energy as this fictitious structure relaxes is shown. We started from the undimerized Si(100) with Si-O-Si=O bonds staying in the vertical plane

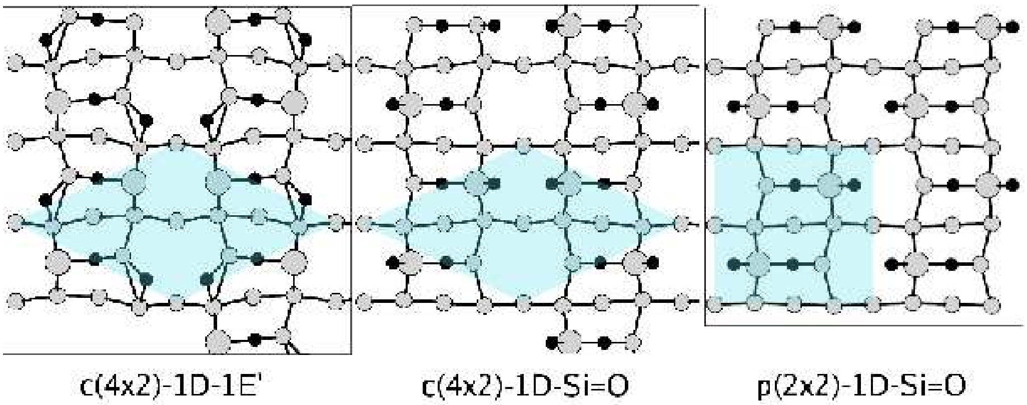

Figure 5.2: Schematic diagram of the Si–O related models of the 1ML oxidized Si(100) considered in this work. Left: $c(4 \times 2)$ with backbond and dative bonded silanone; Middle: $c(4 \times 2)$ bridge bond and silanone; Right: $p(2 \times 2)$ bridge bond and silanone. Large circles indicate "up" silicon dimer atoms; small filled circles are oxygen atoms. The $c(4 \times 2)$ and $p(2 \times 2)$ unit cells is indicated by shaded regions.

base	structure	E_{surf}[eV/Å^2]	N_{e^-}	N_{O}	N_k
$c(4 \times 2)$	clean	0.0903	256	0	6
$p(2 \times 2)$	clean	0.0905	256	0	4
base	structure	E_{ads} [eV]	N_{e^-}	N_{O}	N_k
$c(4 \times 2)$	1D	-7.14	280	2	6
$c(4 \times 2)$	1E'	-7.22	280	2	8
$c(4 \times 2)$	Si=O	-5.73	280	2	2
$c(4 \times 2)$	1D+1E'	-7.17	304	4	2
$c(4 \times 2)$	1D Si=O	-6.76	304	4	2
$p(2 \times 2)$	1D Si=O	-7.04	304	4	4
$c(4 \times 2)$	"A" in Fig. 5.3	-6.74	304	4	2
$c(4 \times 2)$	"B" in Fig. 5.3	-6.82	304	4	2
$c(4 \times 2)$	"C" in Fig. 5.3	-7.45	304	4	2

Table 5.2: A summary of energetics of all stable and metastable configurations found after BFGS relaxation for the oxidized Si(100) surface. Structures are listed with their total energies, each force component is relaxed below the threshold of 0.13 eV/Å.

(perpendicular to the surface). After some BFGS steps, the Si-Si dimers are formed, but the Si-O-Si=O bonds are still both present. In configuration "A" (see Fig. 5.3), one of the Si=O starts to bond the dimer until the metastable structure "B" where there is still the Si-O-Si=O bond in the plane (see blue arrows in Fig. 5.3), but the other oxygen is bonded in a Si-O-Si-O-Si chain, similar to a part of the SiO_2 crystal lattice. Leaving this structure to relax we found the configuration "C" without any silanone bonds and characterized by a silicon atom bonded to 3 oxygens. In this last configuration Si(100):O (1ML) reaches the lowest total energy.

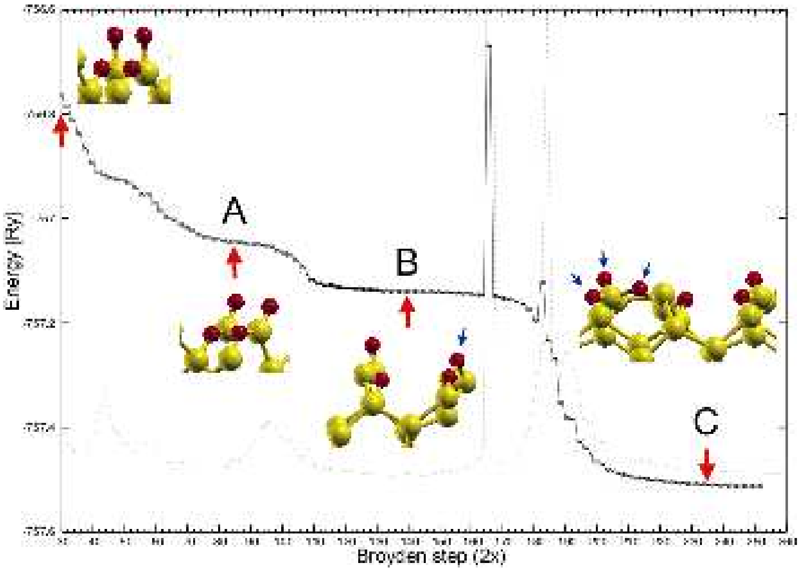

Figure 5.3: Total energy of configurations generated by relaxing Si(100) with one oxygen on the backbond and one oxygen on top of the higer silicon atom of the dimer.

5.2 Electronic structure and the effect of oxidation

We present here the computed Kohn-Sham band structure of three models of oxidized Si(100). The electronic structure of the 1D and 1E' surfaces is shown in Fig. 5.4 along a standard path in the surface brillouin zone: Γ-$\bar{X}$-$\bar{Y}'$-$\bar{Y}$-Γ (see Fig. 2.2 in chapter 2). Mostly, modifications respect to the clean Si(100)–c(4×2) concern a change of surface states inside the bandgap. In fact, comparing Fig. 4.18 to Fig. 5.4, it is evident that oxygens move the surface states visible in the Γ-$\bar{X}$ direction, states that are responsible of the S_0 EEL peak of the clean surface, (see Fig. 4.13 and Fig. 4.12 in Chapter 4). The oxygen adsorbed modifies also bands in the $\bar{Y}'$-$\bar{Y}$ path. Moreover, we present in Fig. 5.5 the computation of the electronic states for the surface including a silanone (O)Si=O bound. In Fig. 5.5 it is possible to see the flat bands in the $\bar{Y}$'-$\bar{Y}$ path due to the presence of oxygen doubly bonded to the top silicon of the dimer. Furthermore we performed a test on the $p(2 \times 1)$ structure to better analyse the effect of the isolated Si=O bond. For this system we report the bands compared to that of the clean $p(2 \times 1)$ surface (see Fig. 5.6). The bandgap typical of a semiconductor is closed by the presence of oxygen, hence the system is metallic.

All calculations are performed within the DFT-LDA and a scissor shift of +0.5 eV

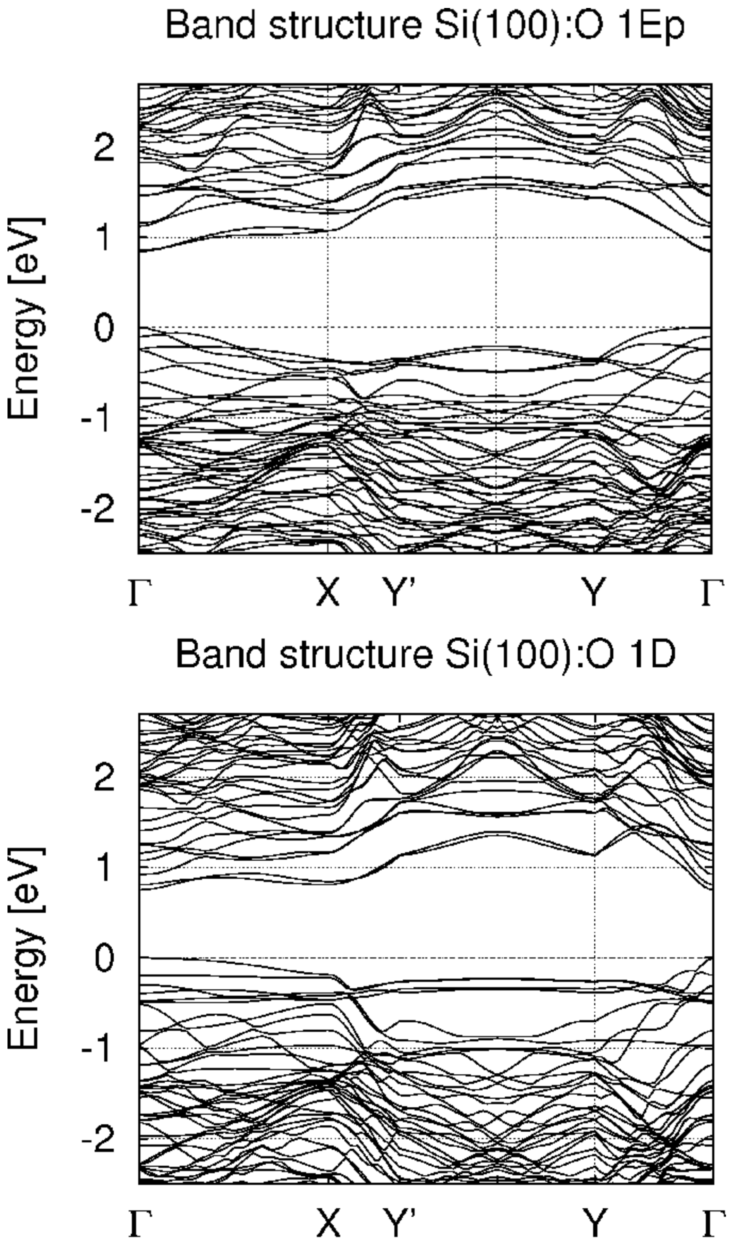
Band structure Si(100):O 1Ep

Band structure Si(100):O 1D

Figure 5.4: Band structures of the 1E′ (top), 1D (bottom). models of the oxidized Si(100) surface. A rigid upward shift +0.5eV (scissor shift) has been applied to the unoccupied bands.

(see sec. 4.5.5) has been applied to the unoccupied bands in order to mimic the many body effects. Band structure calculations are performed with the ABINIT

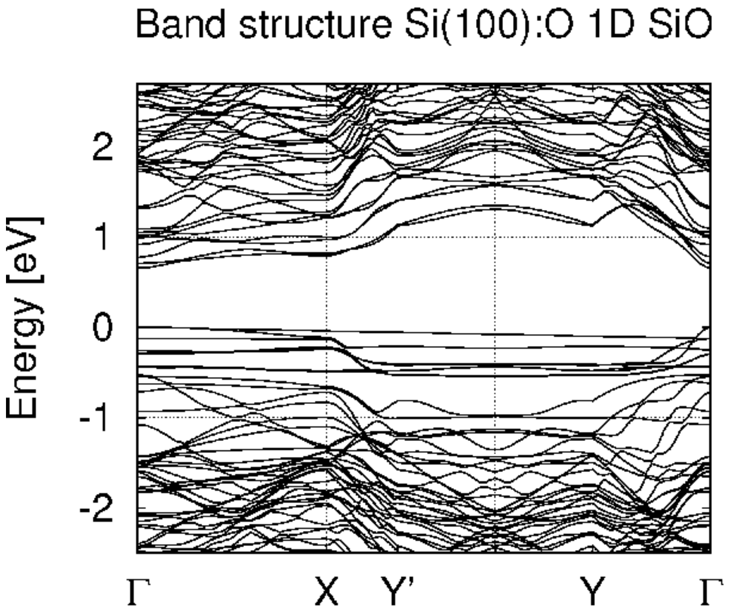

Figure 5.5: Bandstructure of the 1D Si=O model of the oxidized Si(100) surface. A rigid upward shift +0.5eV has been applied to the unoccupied bands. Flat bands along the $\bar{Y}$'-$\bar{Y}$ direction are due to the presence oxygen double bonded to the top silicon in the dimer.

package [122].

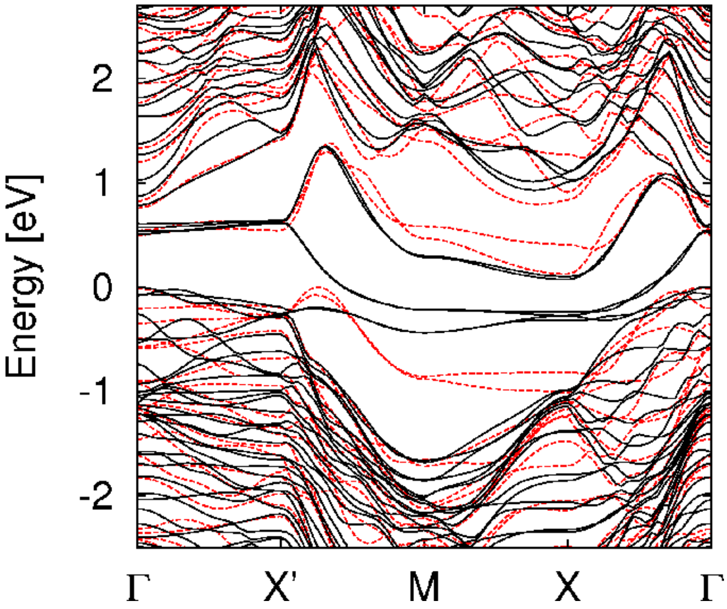

Figure 5.6: Bandstructure of the clean Si(100)-p(2×1) (black line) compared with the ones of $p(2 \times 1)$ Si=O (atomic oxygen) (red dashed line).

5.3 Experimental energy loss data

Experimental EEL spectra of the oxidized Si(100) surface are not so numerous in litterature, at least in the range of energy we are studying (i.e in general up to ≃8-10 eV and in particular up to ≃3 eV). In this work we are refering to not-so-recent data from Ibach *et al.* [116, 117] and at the subsequent paper of Ludeke *et al.* [118] where experimental REELS are reported in terms of the second derivative of the spectrum respect to the energy in order to cut the large contribution of the elastic peak and evidence spectral features.

In Fig. 5.7 all experimental data are collected. The spectra from Ibach *et al.* are reported for the clean (black circles) and oxidized (red circles) surface. In particular, Ibach used high incident energy of the electrons, (E_i=100 eV) and an off specular geometry with normal incidence and collecting electrons at 42.5° respect to the perpendicular direction to the surface plane.

From the analysis of Ibach's data we can conclude that there are two features that seems to be due to the oxygen adsorption: a peak at around 7 eV, which appears in the oxidized surface, and the surface plasmon at around 12 eV which is splitted in two. Moreover, the bulk plasmon, appearing at 17 eV in the clean

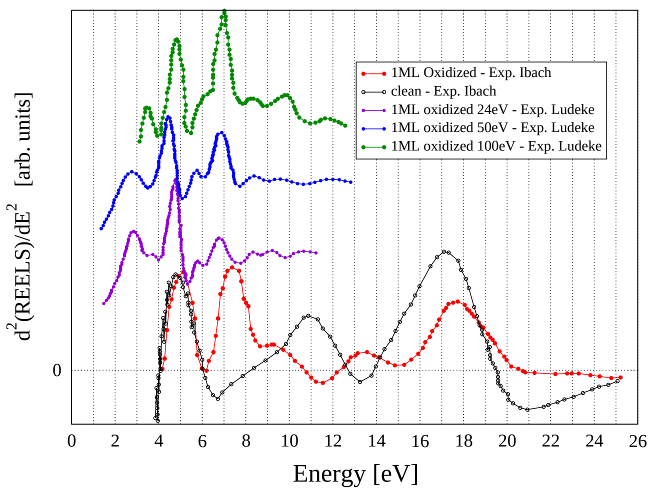

Figure 5.7: Experimental data from Ibach *et al.* and Ludeke *et al.* for the clean (black) and oxidized (red and blue) Si(100) surface.

surface, is lowered and slightly blueshifted.

The other experimental data reproduced in Figure 5.7 are from Ludeke *et al.* [118] (green, blue and violet circles in Fig. 5.7) and refer to specular scattering geometry: backscattered electrons are detected and analyzed. The three sets refers to different incident energies: 24 eV (violet), 50 eV (blue) and 100 eV (green). Peaks at 3 eV and 5 eV (E_1 and E_2 respectively) appear in all those sets of data. From the comparison of the three sets it is possible to conclude that the two main peaks around 5 eV and 7 eV are in agreement with Ibach's results. Moreover the 7 eV peak increases with increasing incident electrons energy and is interpreted by Ludeke *et al.* as an excitation of the SiO or SiO_2 molecules [145, 146] in the Schumann region. We will comment this assignement in the following paragraphs, where we will show that our results do not support it.

5.4 Theoretical energy loss spectra

In the following paragraphs we present REEL spectra calculations of the oxidized Si(100) surface using the code YAMBO [126].

5.4.1 Clean versus oxidized Si(100): the low-energy part of the spectrum

REEL spectra are often presented in literature in terms of the second derivative of the energy loss. Moreover we start presenting here our computed bare REEL spectra for the clean and oxidized Si(100). In particular we considered the clean and the 0.5 ML oxygen-covered surfaces with oxygen inserted into the bridge (1D) or the backbond (1E′). We compare the REEL spectra computed for the experimental setup of Farrell (Ref. [119]: specular scattering at 60° with incident energy E_i=40 eV) with measured spectra for the clean Si(100). All results are shown in Fig. 5.8 where theoretical spectra for x and y polarization directions are also presented separately. In the bottom panel of Fig. 5.8 a comparison of the (unpolarized) experimental data with computed spectra averaged over the two polarization directions is shown.

It is evident that the two main peaks, namely the S_0 shoulder at 0.8 eV and the peak S_1 at 1.3 eV in the experiments, appear also in the calculated spectra for both the clean (black line) and the oxidized 1E′ configurations (blue line). On the contrary, oxygen in the bridge position (1D structure-red line) completely kills the first peak of the spectrum. Unfortunatly we did not find experimental data for this surface at low oxygen coverage in the low energy range ($<$ 3 eV), but a similar behaviour is shown in the case of a coverage of H_2O in Ref. [119]. In conclusion of this section we can say that REEL provide a useful tool able to distinghuish between oxidized surface configurations, in particular in the low energy spectral region.

5.4.2 Clean versus oxidized Si(100): REEL spectra in a wider spectral reagion

In this section we present computed REEL in terms of the second derivative spectrum. In Fig. 5.9 (top panel) we show the bare REEL spectra for the clean, the 1D and 1E′ structures (0.5 ML coverage) computed for the experimental setup used by Ibach and Ludeke in their works [116, 118] (i.e. incident energy E_i=100 eV with slightly different geometry scattering[1]). In the middle panel of Fig. 5.9 we show the computed second derivative spectrum. Neglecting oscillations for energies below 3 eV, and except for the intensity of the surface plasmon peak calculated around

---

[1] Ibach used off specular experimental geometry instead of backscattering geometry form a normal incident beam of electrons used by Ludeke *et al.* in Ref. [118]. However, at this level of approximation we did not find appreciable differences in case of spectra calculated with specular or off specular geometry.

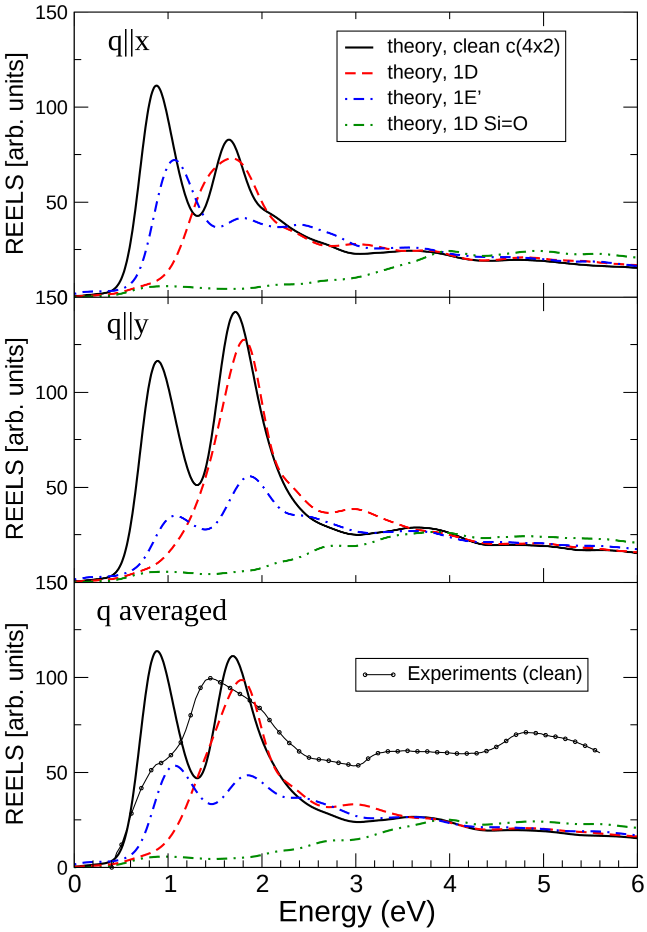

Figure 5.8: Experimental and computed REELS at $E_0 = 40$ eV for clean Si(100)-$c(4 \times 2)$ is compared with the calculated spectra of 1D, 1E$'$ and 1D Si=O oxidized reconstructions. Experiments for the clean are taken from Farrell *et al.* in Ref. [119].

15 eV, the clean and the other two oxidized surfaces do not show any important differences. This is in contrast with experiments (bottom panel of Fig. 5.9) where a peak centred at around 7 eV appears after oxidation. In order to understand the origin of this peak, we analysed the EEL spectra of all configurations presented in Section 5.1. Following arguments presented in Ref. [118] about the origin of the 7 eV peak, we show theoretical results for surfaces including a silanone bond on the $c(4 \times 2)$ and $p(2 \times 2)$ reconstructions of the clean Si(100) and an oxygen inserted in the dimer bridge (Fig. 5.10). We found slight differences with respect to the

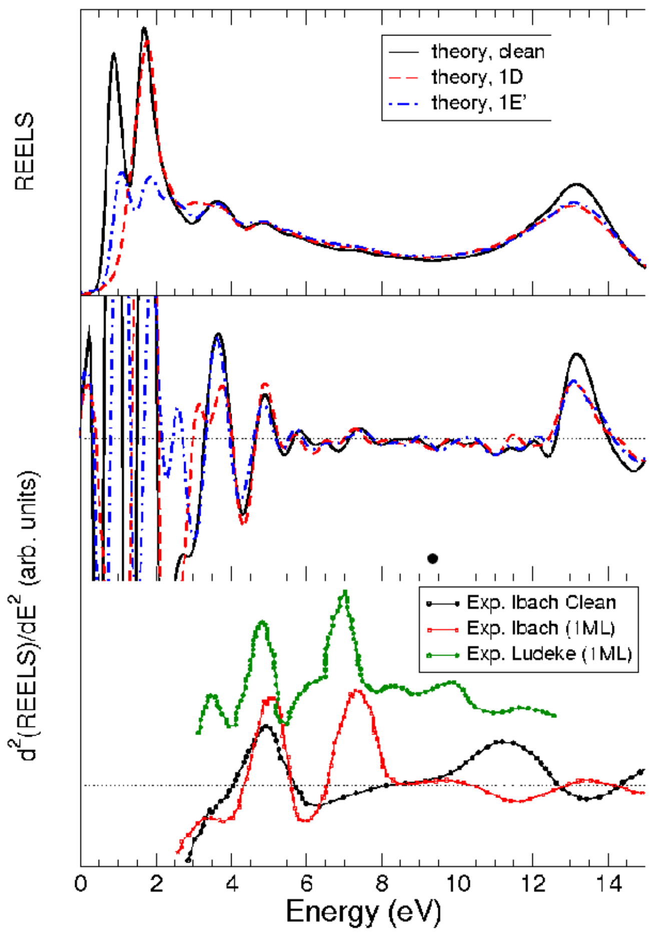

Figure 5.9: Computed bare REEL spectrum (top panel) for clean Si(100)-$c(4\times2)$ compared with the 1D (oxygen in the bridge) and 1E' (oxygen in the backbond) oxidized reconstructions. Calculated negative second derivative spectra of the same surfaces (middle panel) shows slight differences in the spectral region above 3 eV. Experimental data (bottom panel) are also reported from Refs. [117] and [118] showing an important peak at around 7 eV, beyond the main peaks at 3 eV and 5 eV, interpreted as the E_1 and E_2 bulk silicon transitions. The 7 eV peak is absent in the experimental spectrum of the clean (black circles) and is hence interpreted as due to oxidation (red and green circles).

previous calculations: the 7 eV peak still does not appear and the spectral features are similar for the clean and the oxidized surfaces. Unfortunatly, large differences between $c(4 \times 2)$ and $p(2 \times 2)$ structures appear in the low region of the spectrum where experimental data are not available. However we can observe that the surface plasmon is slightly lowered and blueshifted when a silanone bound is included in the surface configuration. Moreover we report in Fig. 5.10 (left) the results concerning the stable "C" structure and his metastable precursor "B" containing one (O)Si=O

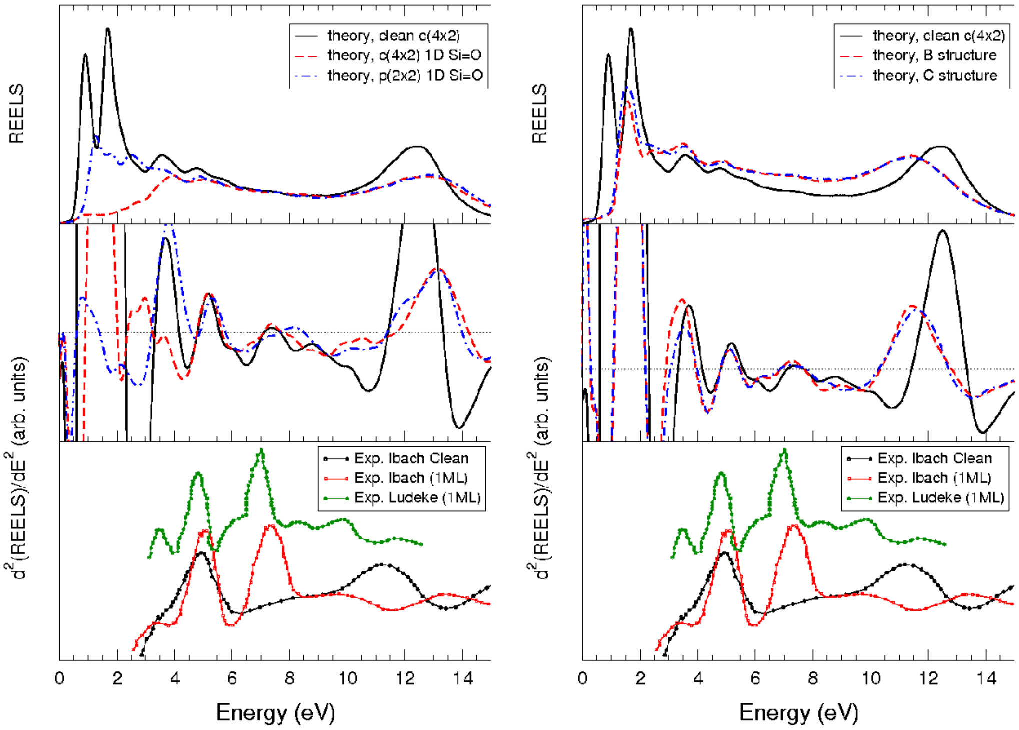

Figure 5.10: Left:REELS for clean Si(100)-$c(4\times2)$ compared with the 1D Si=O and the $p(2\times2)$ 1D Si=O reconstructions. Right: REELS for clean Si(100)-$c(4\times2)$ compared with the B structure (metastable precursor) and C structure For comparison, experimental data from Refs. [118, 117] are reported.

bound depicted in Fig. 5.3[2].

Once more we can see that no features at 7 eV comparable to the experimental peak appears in our calculations, and even if Hemerick *et al.* [32] suggests similar structures on small clusters as energetically favorable, we can not conclude that silanone bond or siloxane structures on Si(100) are representative of the real surface. Moreover, Ludeke *et al.* guessed that the 7 eV peak was related to molecular excitations of Si=O bond or silicon monoxyde molecule. Calculations performed in the present work, however, rule out Si=O structures bonded to the surface.

---

[2] For $c(4\times2)$ silanone structures we used 72k points in the IBZ and 450 bands, corresponding to minimum e–h transition energy of 13.27 eV $p(2\times2)$ required 64k points and 500 bands, corresponding to 15.09 eV, for the “B” and “C” structures 72k points and 500 bands, corresponding to 15.09 eV, have been considered in order to fully converge.

It can be worth to mention that, taking as a reference the surface plasmon peak of the clean Si(100) (represented by the black continuous line in Figs. 5.9, 5.10), oxygen added into 1D and 1E$'$ positions lowers the peak (see Fig. 5.9), while oxygen added into the silanone bonds lowers and redshifts the position (see Fig. 5.10 left panel). Conversely, calculated spectra for B or C configuration show a shift of the peak position to the opposite direction (see Fig. 5.10 right).

At this point, several speculations can be done in order to explain the origin of the peak measured at 7.0 eV, which does not appear in theoretical spectra for the considered structures. From the point of view of calculations we must underline that they are performed only at the RPA level. A further analysis could call for the use of approximations beyond RPA in order to describe eventually strong excitonic effects. Moreovoer, we mention that the oxidation process of Si(100) is still under debate, for example, we can not exclude the formation of clusters of SiO_2 during oxidation. In addition, looking at the intensity dependence of the peak, increasing with the energy of the incident electrons (see Fig. 5.7), we could interpret the peak as due to transitions from states originating from structures below the surface level, in fact, higher energy electrons are expected to penetrate deeper in the sample. Within these hypotesis the present theory could not be adeguate to treat, for example, multiscattering processes. In addition we note that the experimental data are old and it is not clear how well characterized and clean the surfaces are. However we conclude that our calculations does not support Ludeke's interpretation about the origin of the 7 eV peak, because does not appear in all the considered model surfaces (including Si=O or O-Si-O bonds).

5.5 Conclusions

In the present section we draw a summary of the previous analysis, and some conclusions. We calculated the relaxed atomic position of several oxidized si(100) surface reconstructions at 0.5ML (1D and 1E') of coverage. Moreover we analyzed 1ML coverage structures with a silanone bund and an oxygen in the bridge of the dimer (1D Si=O), with a $p(2 \times 2)$ and a $c(4 \times 2)$ base. Finally we found a structure “B” characterized by a silanone bond and Si-O-Si-O-Si chains, to be the metastable precursore of the “C” structure, the most stable, with one silicon atom bonded to three oxygens (see Fig. 5.3).

We calculated the bare REEL spectrum in the cases of the oxydized Si(100) previously considered. We have been able to relate the change in the spectra with the changes in the band structure in the case of both prototypical configuration (oxygen in the bridge and oxygen in the backbond). Furthermore we calculated the second derivative spectra thanks to the implementation of the SG method in the YAMBO code [126]. This allowed us to compare EELS results with the experimental data. We have shown that the excitation at 7 eV can not be related to a molecular excitation of Si=O or O-Si-O, as suggested by Ludeke *et al.*, because the configuration with an oxygen on top of the higher silicon atom in the dimer does not reproduce that structure. At the moment we are not able to give an alternative explanation for the origin of this spectral feature, but we can confirm that the reconstruction studied in this paper (including the most stable structures 1D, 1E$'$, 1D Si=O $p(2\times2)$ and $c(4\times2)$ "C" and the metastable precursor with Si–O and Si=O molecule) do not reproduce this peak. Still, recent works by Hemerick *et al.* and Chabal *et al.* have pointed out the critic presence of silanone bonds during the oxidation process. We can only guess that including many body effects in the calculations could provide more accurate theoretical results, taking into account self-energy and excitonic effects, in order to help in shedding light on that problem.

Chapter 6

Subtleties in electronic excitations of open shell molecules

In this chapter we present a theoretical study of BeH, a simple heteronuclear diatomic molecule with an unpaired electron. We considered BeH molecule as the simplest exemple of an isolated open shell system for which the ground state is expected to be spin polarized. We present calculations of energy levels and density of states. Convergence studies and problems arising up in order to correctly describe excitation spectra are also underlined. At the end some excitation energies calculated for this system are compared to available experimental data and the agreement is discussed.

6.1 Brief review of TDDFT for isolated systems

In this section we briefly review the Casida's approach to treat the molecular excitation of isolated systems. This framework is a reformulation of the TDDFT in the configuration space and the details can be found in Ref. [147, 148]. In fact all the observables are represented using the DFT–KS eigenvectors in such a way that the non–interacting response function results to be diagonal.
We note that in case of isolated systems the physical quantity we deal with is the polarizability of the system $\alpha(\omega)$ that is defined when an external perturbation $\delta V^{ext}(t) = z\delta E_z(t)$ is applied to the system. In this case the x component of the dipole momentum is defined by: $\delta d_x = -q\delta x$ where q is the charge of the electron

and $\delta x = \int d^3x \delta\rho(x,t)x$.
Hence, the polarizability is defined by:

$$\alpha_{xz}(\omega) = -\int d^3x \frac{q\delta x}{E_z(x)} \tag{6.1}$$

and using the Lehmann representation it can be written by:

$$\alpha_{xz}(\omega) = \sum_I 2(E_I - E_0)\frac{\langle\Psi_0|\widehat{x}|\Psi_I\rangle\langle\Psi_I|\widehat{z}|\Psi_0\rangle}{(E_I - E_0)^2 - \omega^2} \tag{6.2}$$

Where E_I, E_0, Ψ_I, Ψ_0 are the energies and the many body wavefunctions of the excited and ground state respectively. Using the basis set of operators $\{\widehat{a}^\dagger_{n\sigma}, \widehat{a}_{m\sigma}\}$ we can define the quantity:

$$P_{ij\sigma}(t) = \langle\Psi^{KS}|\widehat{a}^\dagger_{i\sigma}(t)\widehat{a}_{j\sigma}(t)|\Psi^{KS}\rangle \tag{6.3}$$

corresponding to the density in the configuration space, for which the following relations held:

$$\delta P_{ij\sigma}(t_1) = \int dt' \chi^{KS}_{ij\sigma,hk\tau}(t_1 - t_2)\delta V_{hk\tau}(t_2) \tag{6.4}$$

$$\delta P_{ij\sigma}(t_1) = \int dt' \chi_{ij\sigma,hk\tau}(t_1 - t_2)\delta V^{ext}_{hk\tau}(t_2) \tag{6.5}$$

where the KS response function is written over this basis set:

$$\begin{aligned}\chi^{KS}_{ij\sigma,hk\tau}(\omega) &= \sum_I \frac{\langle\Psi^{KS}_0|\widehat{a}^\dagger_{j\sigma}\widehat{a}_{i\sigma}|\Psi^{KS}_I\rangle\langle\Psi^{KS}_I|\widehat{a}^\dagger_{h\tau}\widehat{a}_{k\tau}|\Psi^{KS}_0\rangle}{\omega - (E_I - E_0) + i\eta} \\ &- \frac{\langle\Psi^{KS}_0|\widehat{a}^\dagger_{h\tau}\widehat{a}_{k\tau}|\Psi^{KS}_I\rangle\langle\Psi^{KS}_I|\widehat{a}^\dagger_{j\sigma}\widehat{a}_{i\sigma}|\Psi^{KS}_0\rangle}{\omega + (E_I - E_0) + i\eta}\end{aligned} \tag{6.6}$$

In case of independent particles and applying the $\widehat{a}$ and $a^\dagger$ operators we obtain the reduced expression for the response function:

$$\chi^{KS}_{ij\sigma,hk\tau}(\omega) = \delta_{\sigma\tau}\delta_{jk}\delta_{ih}\frac{f_{j\sigma} - f_{i\sigma}}{\omega - (\varepsilon^{KS}_i - \varepsilon^{KS}_j)} \tag{6.7}$$

Hence, in the configuration space the TDDFT equation held the form (see Ref. [147, 148]):

$$\sum_{kl\tau}^{f_{k\tau}-f_{h\tau}\neq 0}\left[\delta_{\sigma\tau}\delta_{jh}\delta_{ik}\frac{\omega - (\varepsilon_{h\tau} - \varepsilon_{k\tau})}{f_{k\tau} - f_{h\tau}} - K_{ij\sigma,hk\tau}(\omega)\right]\delta P_{hk\tau}(\omega) = \delta V^{ext}_{ij\sigma}(\omega) \tag{6.8}$$

This equation can be reorganized and written as a matrix equation (see Ref. [147, 148] for mathematical details) exploiting the hermitian nature of the kernel $K_{ij\sigma,hk\tau}$.

Moreover assuming that the KS orbitals and the kernel are real quantities (infinite lifetime of the excitations) and after some algebra we can write:

$$\left[\begin{pmatrix} A(\omega)+B(\omega) & 0 \\ 0 & A(\omega)-B(\omega) \end{pmatrix} - \omega \begin{pmatrix} 0 & -C \\ -C & 0 \end{pmatrix}\right]$$

$$\begin{pmatrix} \mathrm{Re}\,\delta P(\omega) \\ -i\mathrm{Im}\,\delta P(\omega) \end{pmatrix} = \begin{pmatrix} \mathrm{Re}\,\delta V^{ext}(\omega) \\ -i\mathrm{Im}\,\delta V^{ext}(\omega) \end{pmatrix}$$

where:

$$A_{ij\sigma,hk\tau}(\omega) = \delta_{\sigma\tau}\delta_{ih}\delta_{jk}\frac{\varepsilon_{h\tau}-\varepsilon_{k\tau}}{f_{hk}-f_{k\tau}} - K_{ij\sigma,hk\tau}(\omega) \tag{6.9}$$

$$B_{ij\sigma,hk\tau}(\omega) = -K_{ij\sigma,kh\tau}(\omega) \tag{6.10}$$

$$C_{ij\sigma,hk\tau}(\omega) = \frac{\delta_{\sigma\tau}\delta_{ih}\delta_{jk}}{f_{h\tau}-f_{k\tau}} \tag{6.11}$$

and the polarizability as:

$$\alpha_{xz}(\omega) = 2\vec{x}^{\dagger}S^{-1/2}(\Omega(\omega)-\omega^2)^{-1}S^{-2}\vec{z} \tag{6.12}$$

where $S(\omega) = C(A{-}B)^{-1}C$ and $\Omega(\omega) = S^{-1/2}(A{+}B)S^{-1/2}$. Finally, comparing this last expression (6.12) with eq. (6.2) it is possible to write the eigenvalue equation:

$$\Omega(\omega_I)F_I = \omega_I^2 F_I \tag{6.13}$$

where:

$$\begin{aligned}\Omega(\omega_I)_{ij\sigma,hk\tau}(\omega) = {} & \delta_{i,h}\delta_{j,k}\delta_{\sigma,\tau}(\varepsilon_{k,\sigma}-\varepsilon_{h\sigma})^2 + \\ & +2\sqrt{(f_{i\sigma}-f_{j\sigma})(\varepsilon_{j\sigma}-\varepsilon_{i\sigma})}K_{ij\sigma,hk\tau}\sqrt{(f_{h\tau}-f_{k\tau})(\varepsilon_{k\tau}-\varepsilon_{h\tau})}\end{aligned} \tag{6.14}$$

Eq. (6.13) is called Casida equation (see Ref. [147, 148]) and allows to map the problem of finding the excitation spectrum of a system too an eigenvalue problem for the matrix $\Omega(\omega)$.

6.2 Closed and open shell systems: the problem of the correct counting of excitations

We divide now the discussion to the case of closed and open shell systems. In the first case the approach presented in the previous section predicts, in principle, the correct excitation energies. However, in the second case some problem limits its straightforward applicability. In the next paragraphs we present the problem with an example.

6.2.1 Closed shell systems

Let us start with the case of the closed shell systems, i.e. systems having the same wavefunction for the two spin channels. In this case it is possible to diagonalize the Ω matrix, presented in the previous section, exploiting the symmetries resulting from the adiabatic approximation. Let us consider a three levels system consisting of two electrons (see Fig. 6.1), the ground state is characterized by two coupled electrons both occuping the i level, two additional unoccupied levels j and k are available to the excitations. A spin–unpolarized ground state is expected and the Ω matrix has important symmetry properties, so that its eigenvectors will be either symmetric or anti-symmetric with rispect to spin flip. Assuming the adiabatic approximation, the Ω matrix, can be written as:

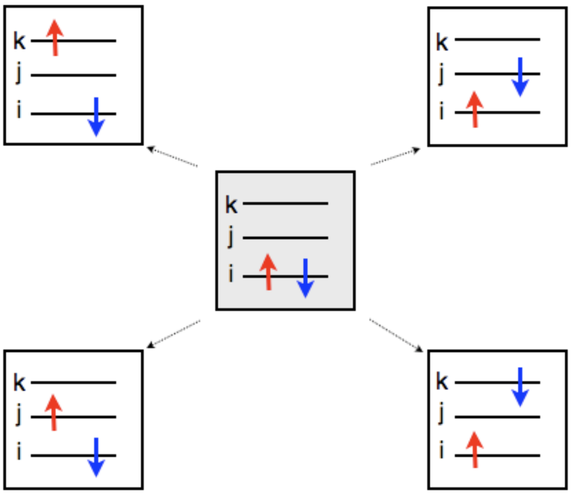

Figure 6.1: Schematic representation of the possible excitations generated in a 3 levels system with 2 electrons with opposite spins.

$$\begin{pmatrix} \Omega_{\uparrow\uparrow} & \Omega_{\uparrow\downarrow} \\ \Omega_{\uparrow\downarrow} & \Omega_{\downarrow\downarrow} \end{pmatrix}$$

such that :

$$\Omega_{\uparrow\uparrow} = \Omega_{\downarrow\downarrow} \quad \text{and} \quad \Omega_{\uparrow\downarrow} = \Omega_{\downarrow\uparrow}$$

The eq. (6.13) is decoupled in:

$$F_{I\uparrow} = F_{I\downarrow} \quad , \quad (\Omega_{\uparrow\uparrow} + \Omega_{\uparrow\downarrow})F_{I\uparrow} = \omega_I^2 F_{I\uparrow} \tag{6.15}$$

$$F_{I\uparrow} = -F_{I\downarrow} \quad , \quad (\Omega_{\uparrow\uparrow} - \Omega_{\uparrow\downarrow})F_{I\uparrow} = \omega_I^2 F_{I\uparrow} \tag{6.16}$$

In case of eq. (6.15) for a given electron–hole pair, both spin channels interfere constructively, TD total charge changes, but not the TD magnetization (Spin-singlet excited state). Conversely in case of eq. (6.16) both spin channels interfere destructively, no TD total charge change, TD magnetization change (Spin-triplet excited state). In this case the resulting eigenvectors are written in the form:

$$\begin{pmatrix} 1 \\ 1 \end{pmatrix} \quad , \quad \begin{pmatrix} 1 \\ -1 \end{pmatrix}$$

Hence, summarizing, it is possible to group the results in two kind of excitations:

$$\phi_0^{1/2} = \frac{1}{\sqrt{2}}\left(|j\uparrow i\downarrow\rangle + |i\uparrow j\downarrow\rangle\right) \qquad \text{singlet} \tag{6.17}$$

and

$$\phi_{-1}^{1} = |i\uparrow j\downarrow\rangle \tag{6.18}$$

$$\phi_0^{1} = \frac{1}{\sqrt{2}}\left(|j\uparrow i\downarrow\rangle - |i\uparrow j\downarrow\rangle\right) \qquad \text{triplet} \tag{6.19}$$

$$\phi_1^{1} = |i\downarrow j\downarrow\rangle \tag{6.20}$$

This states are simultaneous eigenvectors of H^{KS}, S^2 and S_z.

6.2.2 The problem of the open shell systems

The simplest case of a system with spin–polarized ground state consists of three electrons that can be arranged within three levels. Fig. (6.2) describe the ground state configuration and the possible spin–collinear excitations. In this case the Ω matrix does not have the same symmetries presented in the previous section. This time it contains the elements related to the excitations $jk\uparrow$, $ij\downarrow$, $ik\uparrow$ and $ik\downarrow$ resulting with 4×4 dimension. Moreover any symmetry does not allow to divide by blocks the whole Ω. However the selection rules allow to group the excitations in two sets: conserving the spin $\Delta S = 0$ and those for which $\Delta S = 1$.

Diagonalizing H^{KS}, S^2 and S_z simultaneously we obtain the following doublet for the ground state:

$$\phi_0^2 = |\bar{i}ij\rangle$$

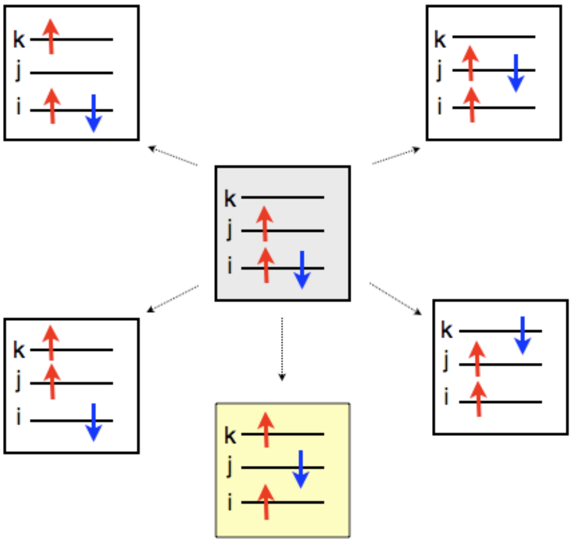

Figure 6.2: Schematic representation of the possible excitations generated in a 3 levels system consisting of 3 electrons. The yellow square represents the double excitation missed by the casida's framework.

and the excited states (doublet):

$$\phi^2_{1/2} = |i\bar{i}k\rangle \tag{6.21}$$

$$\phi^2_{1/2} = |i\bar{j}j\rangle \tag{6.22}$$

$$\phi^2_{1/2} = \frac{1}{\sqrt{2}}\left(|\bar{i}jk\rangle + |ij\bar{k}\rangle\right) \tag{6.23}$$

$$\phi^2_{1/2} = \frac{1}{\sqrt{6}}\left(|\bar{i}jk\rangle + |ij\bar{k}\rangle - 2|i\bar{j}k\rangle\right) \tag{6.24}$$

and the quadruplet:

$$\phi^4_{1/2} = \frac{1}{\sqrt{3}}\left(|\bar{i}jk\rangle + |ij\bar{k}\rangle + |i\bar{j}k\rangle\right) \tag{6.25}$$

where we adopted the notation $\bar{i}$ to indicate the $\downarrow$ spin occupation of the i state. The double excitation $|i\bar{j}k\rangle$, represented by the yellow square in fig. 6.2, is present because the eigenvectors must be simultaneous solutions of the eigenvalue problem for H^{KS} and S^2. The excitations of this system present states with three half occupied levels (see Fig. 6.2) that are mixed by the S^2 operator with similar states with inverted spins.

It is worth to note that this kind of excitations are missing when we attempt to build the eigenstates of H^{KS}, S^2 and S_z starting from the single particle excitations. In this case we obtain three doublet:

$$\begin{aligned}\phi^2_{1/2} &= |i\bar{i}k\rangle &(6.26)\\ \phi^2_{1/2} &= |i\bar{j}j\rangle &(6.27)\\ \phi^2_{1/2} &= \frac{1}{\sqrt{2}}\left(|\bar{i}jk\rangle + |ij\bar{k}\rangle\right) &(6.28)\end{aligned}$$

and a triplet:

$$\phi^3_{1/2} = \frac{1}{\sqrt{2}}\left(|\bar{i}jk\rangle + |ij\bar{k}\rangle\right) \tag{6.29}$$

As the theory is exact and the sole quantity requiring an approximation is the kernel the lack of the excitations description is due to the adiabatic assumption. The research of an improved kernel able to correctly describe the missed excitations is beyond the scope of this thesis.

However, in the following paragraphs an application to the case of the calculations of the excitation energies of the BeH molecule is presented.

6.3 A simple open shell molecule: BeH

A BeH molecule consists of five electrons, four due to Beryllium and one to Hydrogen. Configuration of the Beryllium atom (^{4}Be: $1s^2 2s^2$) suggests his divalent nature, in fact usually the two electrons in the $1s$ level are not involved in chemical bonds. Therefore we describe the joint effect of the core and the inner electrons of Beryllium with a suitable pseudopotential. In particular we used a Troullier–Martins LDA pseudopotential available in the on line repository of the ABINIT code [68, 122]. Following this recipe, only three valence electrons of the molecule are involved in DFT calculations and are expected to determine the main properties of BeH, including the spin polarization of its ground state.

Bond length between Beryllium and Hydrogen is assumed to be $\mathrm{R}_{eq} = 1.3426\text{Å}$ (see Ref. [149]) and the cubic supercell is centred in the middle point of the line joining the centers of the two atoms. A schematic representation of the molecule is depicted in Figure 6.3 where the active electrons (blue and red circles) are underlined and distinguished respect to the spectator electrons (white circles). Spin variable is also shown in order to evidence that spin is not compensated. In the following paragraphs we will show our results about spin resolved calculations performed with the ABINIT package [68].

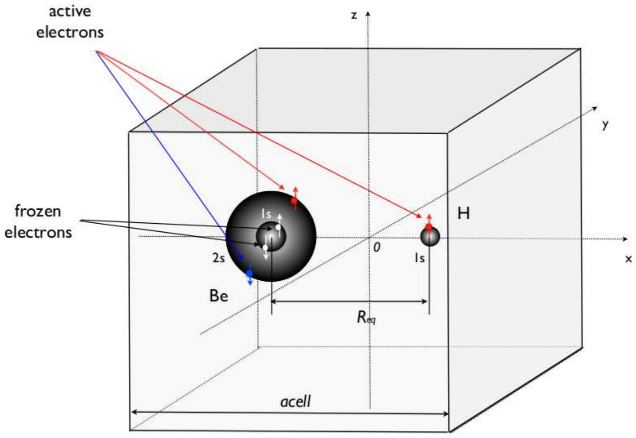

Figure 6.3: Schematic view of the atoms in the cell used to represent the BeH molecule (acell is not on scale). Red and blue circles represent active electrons, white circles represent Beryllium 1*s* electrons. The effect of these core electrons is described by a suitable pseudopotential (see text).

6.4 Energy levels and density of states

In order to obtain converged energy levels and the spin resolved density of states of BeH, we performed total energy minimization within DFT in local spin density approximation.

We obtained the theoretical energy levels (see Fig. 6.4) imposing a convergence tolerance of 10^{15} Ha^2 for the largest squared residual defined by: $\langle nk|(H-E)^2|nk\rangle$, where $E=\langle nk|H|nk\rangle$. In order to establish reliable results we performed convergence tests on the supercell size (see Sec. 6.4.1). Here we comment the results summarized in Table 6.1. We compared our results with theoretical calculations reported in Ref. [149] and experiments from Ref. [150]. We obtained a satisfactory agreement of the Kohn and Sham energy of the highest occupied orbital with respect to calculations performed in Ref. [149] with localized basis orbital.

Even if there is not analogous of the Koopmans theorem, providing a physical interpretation of the Hartree Fock eigenenergies, for the KS eigenvalues, it is possible to interpret the highest occupied molecular orbital (HOMO) energy calculated within DFT as the ionization energy of the system (see ref. [151]).
However in the present case of the BeH molecule, if we assume that the $\mathrm{E}_{3\sigma_\uparrow}$ energy referred to the vacuum should be the ionization energy of the system, we face with

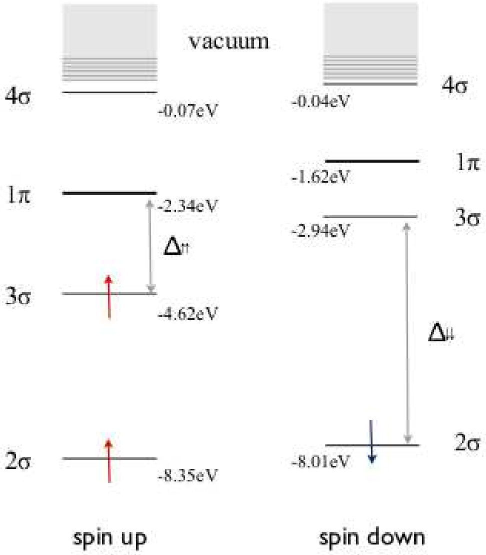
vacuum
4σ
-0.07eV
-0.04eV
4σ
1π
-1.62eV
1π
-2.34eV
-2.94eV
3σ
Δ↑↑
3σ
-4.62eV
Δ↓↓
2σ
-8.35eV
-8.01eV
2σ
spin up
spin down

Figure 6.4: Spin resolved Kohn-Sham energy levels for the BeH molecule calculated within DFT–LSDA. Energy levels are calculated for a 55 Bohr cubic unit supercell with a plane–wave cutoff energy E_{cut}=18 Ha and 20 Kohn–Sham states..

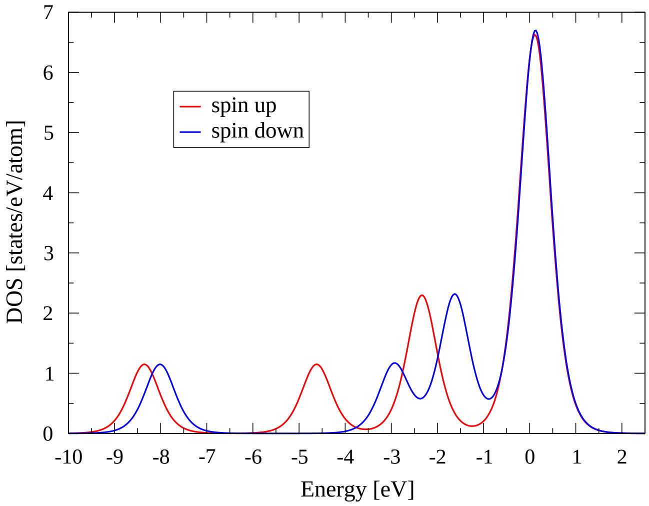

Figure 6.5: Spin resolved density of states for BeH calculated within DFT–LSDA with the code ABINIT [68]. Red and blue lines represent the spin up and down components. A smearing of 0.008 Ha is applied and a 55 Bohr length unit cell is considered.

a discrepancy with respect to the experimental value reported in Ref. [150]. In fact, the experimental value of 8.21 eV disagrees with $-\epsilon^{\mathrm{HOMO}} = 4.62$ eV, calculated within DFT-LSDA, and also with 4.60 eV obtained in Ref. [149]. This discrepancy is due to the inadequacy of the LDA exchange and correlation potential (see Ref. [152, 153]) that does not have an asymptotic $-1/r$ required behaviour. This fact lead to the lack in the description of the levels staying close to the vacuum region and the excitation energies of the molecule involving these levels.

Figure 6.5 represents the distribution of the density of states obtained after convergence tests, discussed in detail in Sec. 6.4.1 and, in Figure 6.5, we report the density of states (DOS) calculated within the same approximations. When spin symmetry is broken, BeH molecule shows an asymmetric distribution of DOS (see Fig. 6.5) with respect to the two spin channels. We considered a cutoff energy $\mathrm{E}_{\mathrm{cutoff}} = 18$ Ha and a cell size $\mathrm{a}_0 = 55$ Ha as converged values. The first three peaks, centred at -8.35 eV, -8.01 eV and -4.62 eV represent the occupied states, also depicted in Fig. 6.4, moreover $3\sigma_\downarrow$ and 1π orbitals are shown, in particular the height of peaks related to 1π orbitals is doubled with respect to the σ orbitals bacause of their degenerancy giving contributions to the DOS peak coming from a double number of states. A smearing of 0.008 Ha is applied to both distributions.

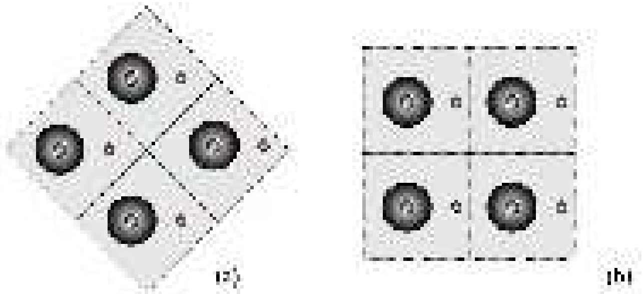

Figure 6.6: Top view of the BeH molecule (black circles) inside a cubic cell, grey zone represents the vacuum region around the molecule (cell is not on scale). As an exemple we report a comparison between two possible choices of the molecule placement inside the cell: distance between atoms of the replicas is larger in case (a) than (b).

6.4.1 Convergence issues

Convergence tests have been performed respect to two quantities: (i) the cutoff energy E_{cut} determining the number of plane wave of the basis set and (ii) the supercell dimension *acell*.

In order to determine a suitable value for E_{cut} we checked the values of the KS-eigenvalues: $\mathrm{E}_{2\sigma_\uparrow}$, $\mathrm{E}_{2\sigma_\downarrow}$ and $\mathrm{E}_{3\sigma_\uparrow}$, corresponding to the occupied states (see Figure 6.4 and Table 6.1). Since we used a Troullier–Martin (TM) pseudopotential for Be, we found a resonable converged value of E_{cut} = 18Ha (corresponding to 36Ry) see Table 6.1 and Fig. 6.4. However we verified that E_{cut} = 10 Ha can be considered a converged value in order to calculate the first excited states of the molecule, in fact, the HOMO–LUMO distance for each spin channel does not change significantly. Table 6.1 summarize the converged values for $\Delta_{\uparrow\uparrow} = 1\pi_\uparrow - 3\sigma_\uparrow$ and $\Delta_{\downarrow\downarrow} = 3\sigma_\downarrow - 2\sigma_\downarrow$, that distances are also evidenced in Fig. 6.4. Moreover, a set of tests with respect to the cell size have been performed in order to find the best compromise between accuracy and practical feasibility of calculations. In fact, a large vacuum region around the molecule is required in order to obtain the correct behaviour of continuum states above the vacuum level (see Fig. 6.7) and to avoid spurious interactions between replicas, however this request can increase significantly the computational workload.

It is worth to mention that a good choice of the cell shape (see Fig. 6.6) can slightly optimize the numerical convergence. We considered the molecule placed in the

Level	present work	Ref. [154]	Ref. [149]	Exp. Ref. [150]
$2\sigma_\uparrow$	-8.35	-8.35	-	-
$2\sigma_\downarrow$	-8.01	-7.99	-	-
$3\sigma_\uparrow$	-4.62	-4.63	-4.60	8.21
HOMO–LUMO	present work	Ref [154]		
$\Delta_{\uparrow\uparrow}$	2.28	2.29		
$\Delta_{\downarrow\downarrow}$	5.07	5.16		

Table 6.1: Theoretical spin resolved energy levels and HOMO-LUMO distance for BeH molecule calculated within DFT-LDA using the code ABINIT [68]. A 55 Bohr cell, E_{cut} =18 Ha and 20 bands have been used and considered converged values.

middle of a cube of length a_0 (*acell*) with the straight line joining Beryllium and Hydrogen atoms parallel to one face of the cube (Fig. 6.6(b)).

We performed several tests increasing a_0 for a fixed cutoff energy and number of bands. In Fig. 6.7 a summary of the results is depicted: in the actual range of a_0 considered, occupied states slightly change because of the dimension of the supercell, on the contrary the unoccupied levels are strongly influenced and require a large cell size ($a_0 > 50$ Bohr). This fact can be important if we want to calcuate excited energies involving higher energy levels. In Fig. 6.4 we can distinguish discrete unoccupied states ($1\pi, 3\sigma, 4\sigma$) and a thick serie of states above the vacuum level (grey region). In fact, increasing the cell size, the upper levels become closer and closer with each other (see Fig. 6.7) and a continuum of states, in the limit case of an infinite supercell. In conclusion we assumed that a cell size of 55 Bohr is required in order to correctly calculate the three lowest eigenvalues. On the contrary, for excited states calculations, involving higher energy levels in the vacuum, a larger cell is recommended. Our conclusions are in agreement with a slightly different treatment discussed in Ref. [154].

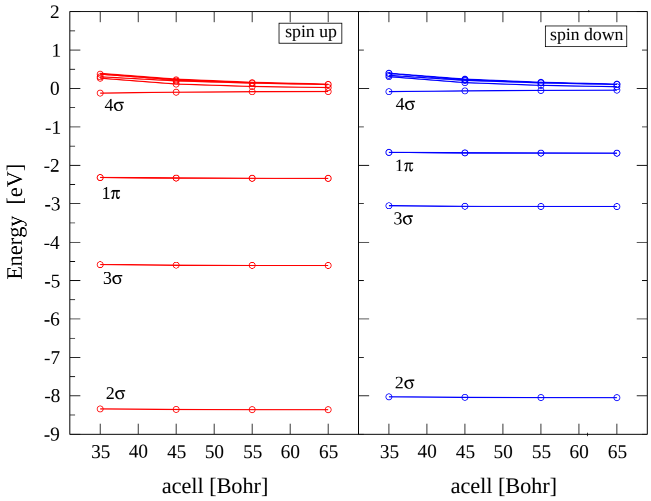

Figure 6.7: Energies of the molecular orbitals of BeH as a function of the cell size. Spin up (right panel, red circles) and down (left panel, blue circle) are distinguished. Unoccupied states are strongly influenced to the cell size and require $a_0 > 50$ Bohr. Tests are performed with a cutoff energy of 10 Ha.

6.5 Excitation energies

In this section we report results concerning excited state calculations within the TDLSDA formalism. For that we used a recent implementation of the method in the ABINIT software [68, 122, 154]. In Table 6.2 we summarize the results about the main excitation energies calculated. We did not consider excitations involving continuum states because they are extremely influenced by the countour conditions. However, in order to have more reliable results we used a larger supercell with respect to the case of ground state calculations, in particular a 70×70×70 Bohr cubic cell is considered with a cutoff energy of 10 Ha and 50 bands.

Even if the ionization energy disagrees with respect to experimental data making a shorter distance between occupied states and vacuum level, our first calculated excitation energy Π connecting the spin-collinear states $3\sigma \rightarrow 1\pi$ is comparable with experimental value reported in Ref. [155]. The TDLSDA theoretical value (2.39 eV) understimates the experimental measure (2.48 eV) but improves the DFT-LSDA HOMO-LUMO distance (2.27 eV) calculated as a bare difference between Kohn-Sham eigenvalues (see Table 6.1 and 6.2).

However we observed that every excitation involving states higher than the 4σ

Excitation	elec. conf.	this work	Ref. [149]	Ref. [156]	Exp.^{a}	Exp.^{b}
$\Pi : 3\sigma_\uparrow \rightarrow 1\pi_\uparrow$	$2\sigma^2 1\pi^1$	**2.37**	2.391	2.2479	2.56	2.48
$\Sigma : 3\sigma_\uparrow \rightarrow 4\sigma_\uparrow$	$2\sigma^2 4\pi^1$	4.51	4.593	4.5103	5.51	-
$\Sigma : 3\sigma_\uparrow \rightarrow 5\sigma_\uparrow$	$2\sigma^2 5\sigma^1$	4.62	-	4.6300	5.61	-
$\Pi : 3\sigma_\uparrow \rightarrow 2\pi_\uparrow$	$2\sigma^2 2\pi^1$	4.70	-	4.7047	6.31	6.317
$\Sigma : 2\sigma_\downarrow \rightarrow 3\sigma_\downarrow$	$2\sigma^1 3\sigma^2$	**5.41**	5.129	4.8049	-	-
$\Pi : 2\sigma_{\uparrow\downarrow} \rightarrow 1\pi_{\uparrow\downarrow}$	$2\sigma^1 3\sigma^1 1\pi^1$	5.66	-	5.1685	-	-
$\Pi : 2\sigma_{\uparrow\downarrow} \rightarrow 1\pi_{\uparrow\downarrow}$	$2\sigma^1 3\sigma^1 1\pi^1$	**7.15**	-	-	-	7.46
$\Sigma : 2\sigma_\downarrow \rightarrow 4\sigma_\downarrow$	$2\sigma^1 3\sigma^1 4\sigma^1$	8.01	-	-	-	-

Table 6.2: Theoretical excitation energies for BeH molecule calculated within the TDDFT framework and ALDA approximation using the code ABINIT [68]. Energy values are reported in eV. Converged results are obtained with a cutoff energy of E_{cut}=10 Ha, 70×70×70 Bohr and 50 bands. We compare our results with calculated values within two TDDFT implementations in the code DeMon2K (see Ref. [149, 156]). Exp.^{a} are reproduced from Tab. I of Ref. [157] and Exp.^{b} from Ref. [155].

level are strongly influence by the cell size. For this reason we evidenced with bold carachter in Table 6.2 the more reliable results, i.e. excitations excluding states above 4σ. Moreover we underline that the Π excitations, involving three half occupied states ($2\sigma^1 3\sigma^1 1\pi^1$), appear at two excitation energies (5.66 eV and 7.15 eV) and with the same orbital configuration. These Π-excitations are distinguished by their total spin, i.e. S= 1/2 in one case and higer total spin in the other. Thanks to the Hund's rule we can identify the excitation with S= 1/2 with higer energy (7.15 eV), and this lead us to discard the 5.66 eV excitation. A different argument leads Casida *et al.* to reject the same excitation identifying the same excitation we discarded as *spin contaminated*. Comparison with experiments available in Ref. [155, 157] are satisfactory, in particular with respect to the case of $\Pi : 3\sigma_\uparrow \rightarrow 1\pi_\uparrow$ and $\Pi : 2\sigma_{\uparrow\downarrow} \rightarrow 1\pi_{\uparrow\downarrow}$ excitations. Discrepancy about $\Pi : 3\sigma_\uparrow \rightarrow 2\pi_\uparrow$ excitation is due to the problem previously underlined: in fact 2π states are higer than 4σ level.

Comparison with results obtained in Ref. [149, 156] are also aligned with our conclusions.

6.6 Conclusions

We studied the BeH molecule as the simplest exemple of open shell system. In our pseudopotential approach only three valence electrons are involved in the eigenvalue problem, for this reason total spin is not compensate and the electronic ground state is spin polarized.

Spin resolved density of states and energy levels have been computed within DFT–LDA approach. Convergence tests with respect to the supercell size have shown the sensitivity of the unoccupied states above the vacuum level to the cell dimension. Moreover we found a discrepancy between the energy of the HOMO orbital calcualted (in agreement with others theoretical works, see ref. [149] and [156]) and the ionization energy measured. This is due to the well known inadequacy of the asimptotic behaviour of the LDA exchange and correlations potential.

In conclusion we calculated the first excitation energies of the molecule using TDDFT within the adiabatic approximation. We compared our reliable results with experimental data finding a satisfactory agreement even if a part of the excitations can not be reproduced by frequency–independent kernels such as the ALDA one.

Chapter 7

A paradigmatic case for semicore and spin-polarization effects in electronic spectra of solids: bulk iron

Semicore states of transition metals such as iron are outside the reach of “standard” pseudopotential of DFT which, even when *non linear core corrections* are adopted, include them in the frozen atomic core. In this work we present an analysis of several pseudopotentials for iron generated in the Troullier Martins and Hamann scheme assuming both local density and generalized gradient approximations (LDA, GGA) for the exchange–correlation functional and considering core-valence partitions with and without including semicore orbitals among valence states. Non linear core corrections are considered and the pseudopotential transferability has been checked. We calculate structural and electronic properties of the α phase of iron and we present a comparison between calculated optical conductivity and experimental data.

7.1 Pseudopotentials for iron

Pseudopotentials (PP) are a well-established tool in *ab initio* structure calculations of solids. A review of the topic can be found in literature ranging from the most influential works [10, 11, 12, 13, 14, 15, 16, 17] to other important but less fundamental papers [18, 19, 20, 21]. Important advantages of the pseudopotential approach can be summarized in the following two points: first, by replacing the atom by a pseudoatom, the number of orbitals which have to be calculated is reduced, and, second, using plane waves, the size of the basis set can be substantially reduced, because the pseudo-wavefunctions are smoother than their all-electron counterparts.

However in all cases where an overlap between valence and core wave functions exists, the *frozen core* approximation underlying the construction of all pseudopotentials is not well satisfied. One way to overcome this problem is the inclusion of a core correction considering the non linear contribution of the core charge to the exchange-correlation potential (NLCC). Another more straightforward solution is the explicit inclusion of the semicore electrons into the valence shell.

In this work we considered both these approaches in order to build pseudopotentials for the specific case of iron. Such pseudopotentials are used to calculate the structural and electronic properties of the α phase of bulk iron. In conclusion we report our results for the optical conductivity compared with experimental data. The $3d$ wavefunctions of iron are strongly localized and show a significant overlap with the $3s3p$ orbitals, although the latter are much lower in energy. Looking at Fig. 7.1, it is evident that the separation of the electronic system into well-isolated core and valence shells is ambiguous, because of the large overlap between $3s$ and $3d$ states. For this reason, we considered two electronic configurations: one with 8 ($3d^6 4s^2$ states) and the other with 16 ($3s^2 3p^6 3d^6 4s^2$ states) valence electrons. We used two schemes for pseudopotential generation, referring to Hamann [21] and Troullier–Martins [20] works respectively. In the former scheme a fixed cutoff radius $\mathrm{r_{cl}}$ by an exponential function $\exp[-(r/r_{\mathrm{cl}})\lambda]$, in the latter scheme wavefunctions are built with a parametric form $r^{l}\exp[\rho(r)]$ below $\mathrm{r_{cl}}$, where $\rho(r)$ is a polynomial of order six in r^2.

In the case of a standard pseudoatom with 8 valence electrons we verified the importance of including non linear core corrections (NLCC) to correct GGA pseudopotentials presenting fake wiggles in the $\mathrm{r} \to 0$ limit due to the gradient dependence of the exchange-correlation approximation.

In the case of a 16 electrons pseudoatom we could not generate a transferable pseudopotential in generalized gradient approximation, neither in the Troullier-Martins nor in the Hamann scheme. The only pseudopotential with good transferability was generated within the local density approximation following the Hamann scheme.

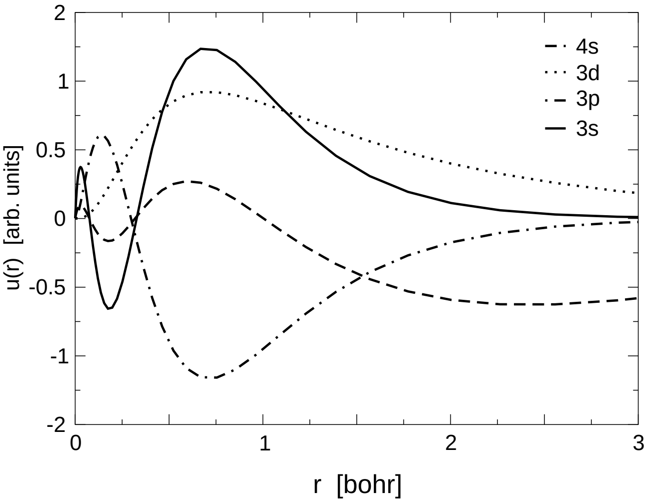

Figure 7.1: Wave functions of $3s3p3d$ and $4s$ level of iron can be distinguished by their different localization. The not-negligible overlap between $3d$ and $3s$ leads to an ambiguity in the definition of core and valence states and to the need of corrections to the frozen core approximation.

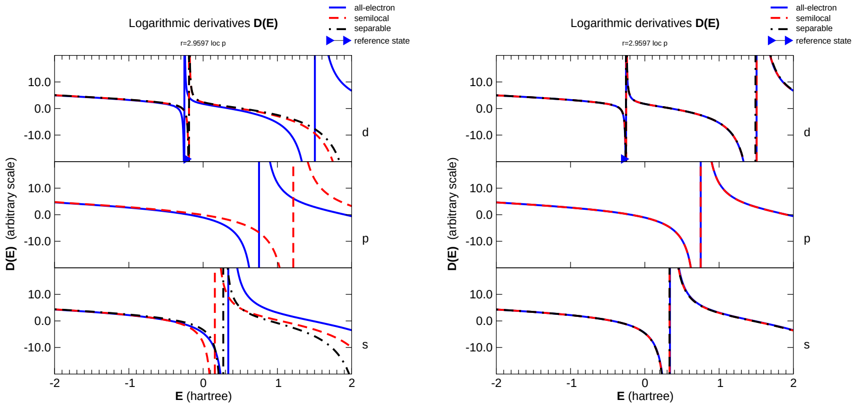

Figure 7.2: Logarithmic derivatives in the case of a 16 electrons pseudoatom. Left: Pseudopotentials generated according to the Troullier-Martins scheme show discrepancies between the differents curves, and are less transferable. Right: Pseudopotentials generated within the Hamann scheme are more transferables and consequently more accurate in reproducing scattering properties.

In order to check the pseudopotential transferability we studied logarithmic derivatives and compared them to the their all-electrons counterpart.
Figure 7.2 shows logarithmic derivatives in case of Troullier–Martins (left) and Hamann (right) pseudopotentials respectively. Hamann pseudopotential are clearly more transferable, and therefore more accurate in describing scattering properties. However we should be aware that Hamann pseudopotentials are usually much more expensive in terms of plane waves required for convergence than the ones generated within the Troullier Martins scheme. As a general rule, depending on the specific system and properties we want to describe, a compromise between accuracy and efficiency should guide the choice of the suitable pseudopotential.

7.2 Properties of bulk iron

In this section we report the results of DFT calculations of structural and electronic properties of bulk iron. We also show a Time Dependent DFT calculation of the optical conductivity, and we compare our results with experimental data.

7.2.1 Structural properties

An useful comparison between the generated PP can be based on the evaluation of physical quantities. In particular we calculated the lattice parameter a_0 of iron. We considered iron in his α phase, the most stable at normal temperatures, where the metal presents a body centred cubic (BCC) crystal structure.

The optimized value of a_0 has been obtained by an estimation of the minimum of the Birch–Murnaghan [158, 159] equation of state for solids:

$$E(V) = \frac{B_0 V}{B_0'(B_0'-1)}\left[B_0'\left(1-\frac{V_0}{V}\right)+\left(\frac{V_0}{V}\right)^{B_0'}-1\right] \tag{7.1}$$

where B_0 is the bulk modulus and V_0 is the cell volume at the minimum. We used the ABINIT package [68, 122] to compute converged total energy for different values of the cell parameter a_0, and we fitted the obtainted points with Eq. 7.1 (see Fig. 7.3). In Tab. 7.1 we report a summary of the lattice parameters and bulk moduli obtained with the fitting procedure. Moreover Fig. 7.3 shows a comparison between LDA and GGA results, confirming a well known understimation of the experimental value by LDA, that can be partially corrected using GGA.

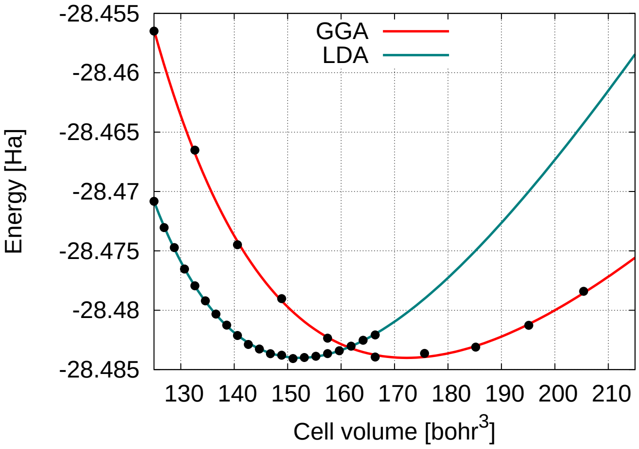

Figure 7.3: Birch–Murnaghan fit of DFT total energy calculations for iron (8 valence electrons) performed within local density (continuous line) and generalized gradient (dotted line) approximations. Lattice parameter calculated within LDA are lower than the experimental value, and GGA partially correct this understimation.

Pseudopotential	a_0 [Bohr]	B_0 [GPa]	μ [μ_B]
8e- TM GGA NLCC	5.56	67.86	2.47
8e- TM LDA NLCC	5.34	106.31	2.11
16e- H LDA NLCC	5.27	101.23	2.19
Exp.$^{(a)}$	5.42	168	2.22

Table 7.1: Comparison of lattice parameter for iron calculated with different pseudopotentials. Exp.$^{(a)}$ are experimental data reproduced from Ref. [160, 161].

7.3 Electronic properties

7.3.1 Electronic properties

We present here our results for the density of states (DOS) around the Fermi energy and the electronic band structure including semicore states. These calculations have been performed with the ABINIT package [68] in local spin density approximation (LSDA). We verified that a random sampling of **k** points in the Brillouin Zone (BZ) is more efficient than the use of a regular grid, in fact with 5000 **k** DOS is converged. In Fig. 7.4 two curves represent converged DOS where the two spin channels show an asymmetric distribution allowing to identify the majority and minority component. The corresponding band structure is presented in Fig. 7.5, where

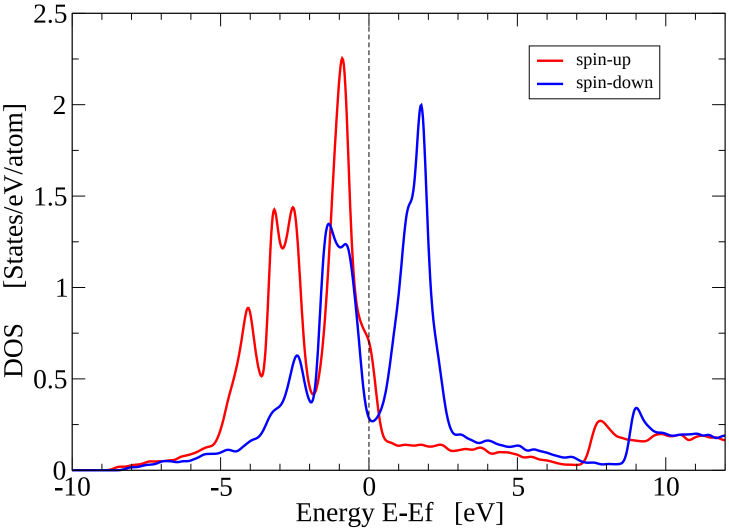

Figure 7.4: Spin resolved density of states of BCC iron calculated within DFT–LDA with ABINIT [68]. Majority (red line) and minority (blue line) spin channels are presented. The Fermi energy is set to zero for clarity.

high symmetry crystallographic directions are chosen in agreement with previous literature [162, 163, 164]. We used Hamann LDA pseudopotentials generated including semicore states in order to describe the core bands $3p$ and $3s$ bands. We obtain band energies of Fe-3s (85 eV) and Fe-3p (52 eV) as depicted in Fig. 7.5. In the same figure we show the effect of the spin on the electronic properties, removing most of the accidental degenerancies of band structure and splitting the flat core states. In addition we report in Fig. 7.6 (top panel) a comparison between bands calculated within LDA or GGA, concluding that the GGA corrections do not change dramatically the electronic structure making LDA a satisfactory approximation for our scope. Even the use of semicore PP (bottom panel in Fig. 7.6) do not influence considerably the estimation of valence states, therefore it is possible to conclude that our approximations are reasonable in order to predict correctly the optical properties of bulk iron.

On the contrary, the case of $3p$ levels is more subtle. In fact, because the angular momentum $\vec{l}$ is not zero for p levels (i.e. l=1), the total quantum number $\vec{j} = \vec{s} + \vec{l}$ must be considered, and the spin orbit coupling can influence the exact degenerancy and position of the bands. Even if this case will not be treated in the present work,

state	$\Delta E_{\uparrow\downarrow}$ [eV]	Dispersion [meV]	$\Delta E_{\uparrow\downarrow}^{exp.}$ [eV]
$3p$	3.03	360 (at N)	-
$3s$	3.15	120 (at Γ)	4.9

Table 7.2: Calculated splitting of the core states compared with available experimental data and calculated dispersion.

because beyond the aim of the thesis, it is worth to mention that a fully relativistic approach is required in order to obtain reliable results for this kind of states. Conversely, the $3s$ states are correctly predicted within the DFT–LSDA approach and the up–down splitting $\Delta_{\uparrow\downarrow} = 3s_\uparrow - 3s_\downarrow$ is comparable with the available experimental data [161]. For completeness, we report in Tab. 7.2 the calculated splitting and dispersion of both the $3s$ and $3p$ levels.

In conclusion we also report an analysis of the relation between total magnetization μ of iron and the $3s$ splitting. It was suggested in the past [165, 166] that s core-level splitting could be used to monitor the magnetic moment or the hyperfine field, because the splitting should vary linearly with the spin state of the unfilled inner shell. X-ray photoelectron spectroscopy (XPS) measurements for nonmetallic transition metal compounds, on rare-earth metals and ionic compounds [165, 166, 167] are compatible with this scheme.

However, Fe-$3s$ XPS splitting studied in crystalline and amorphous alloys have shown a poor correlation between the $3s$ splitting and the magnetic moment of the solid (see Fig. 3 in Ref. [161]). Our calculations show a linear relation of such a splitting with respect to the total magnetization of bulk iron (see Fig. 7.7 top panel), giving some basis to better investigate the apparent disagreement with experimental data.

We calculated the total magnetization defined as the difference between the majority and minority spin density integrated over the unit cell $\mu = \int_\Omega \rho_\uparrow(r) - \rho_\downarrow(r)$. This quantities has been evaluated for several lattice parameter values of bulk Fe, centred around the experimental one (5.42 Bohr). Changes of the lattice parameter influence the local distance between atoms, reproducing the effect of a change of pressure. Moreover changes on lattice geometry affect total magnetization. The dependence of the splitting with respect to the pressure is shown in Fig. 7.7 bottom panel.

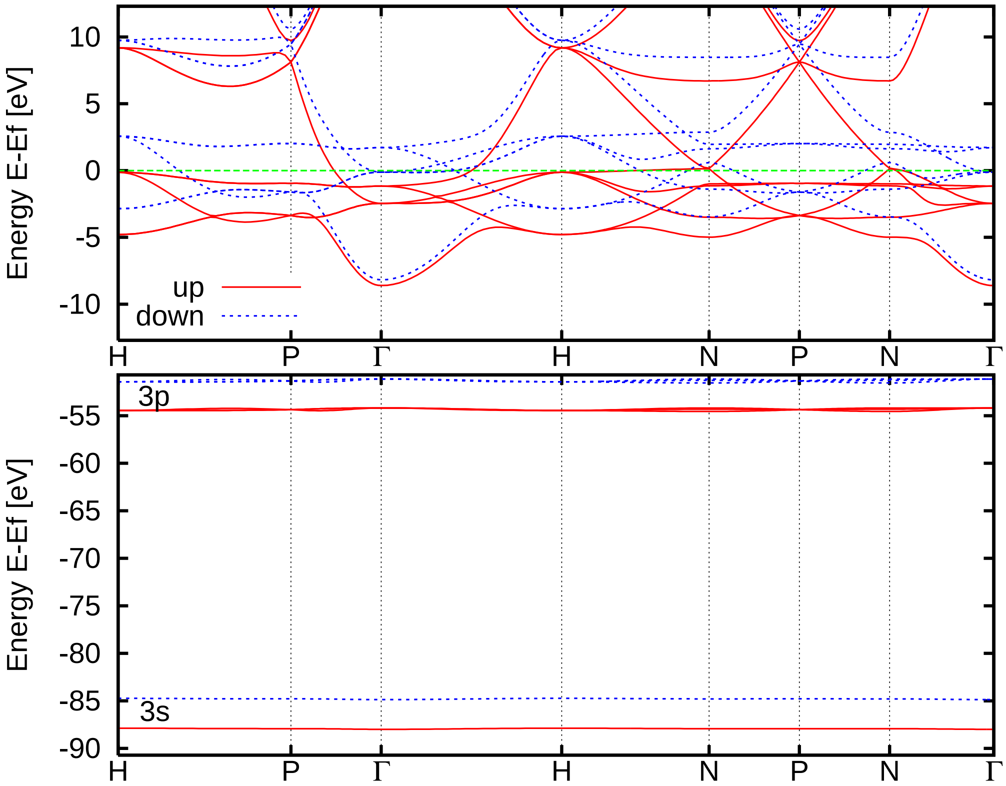

Figure 7.5: Spin resolved band structure of BCC iron along standard high symmetry directions of the Brillouin zone, calculated in LDA approximation with the ABINIT [68] code. Valence (top) and semicore (bottom) states are distinguished in different panels in order to evidence energy scales.

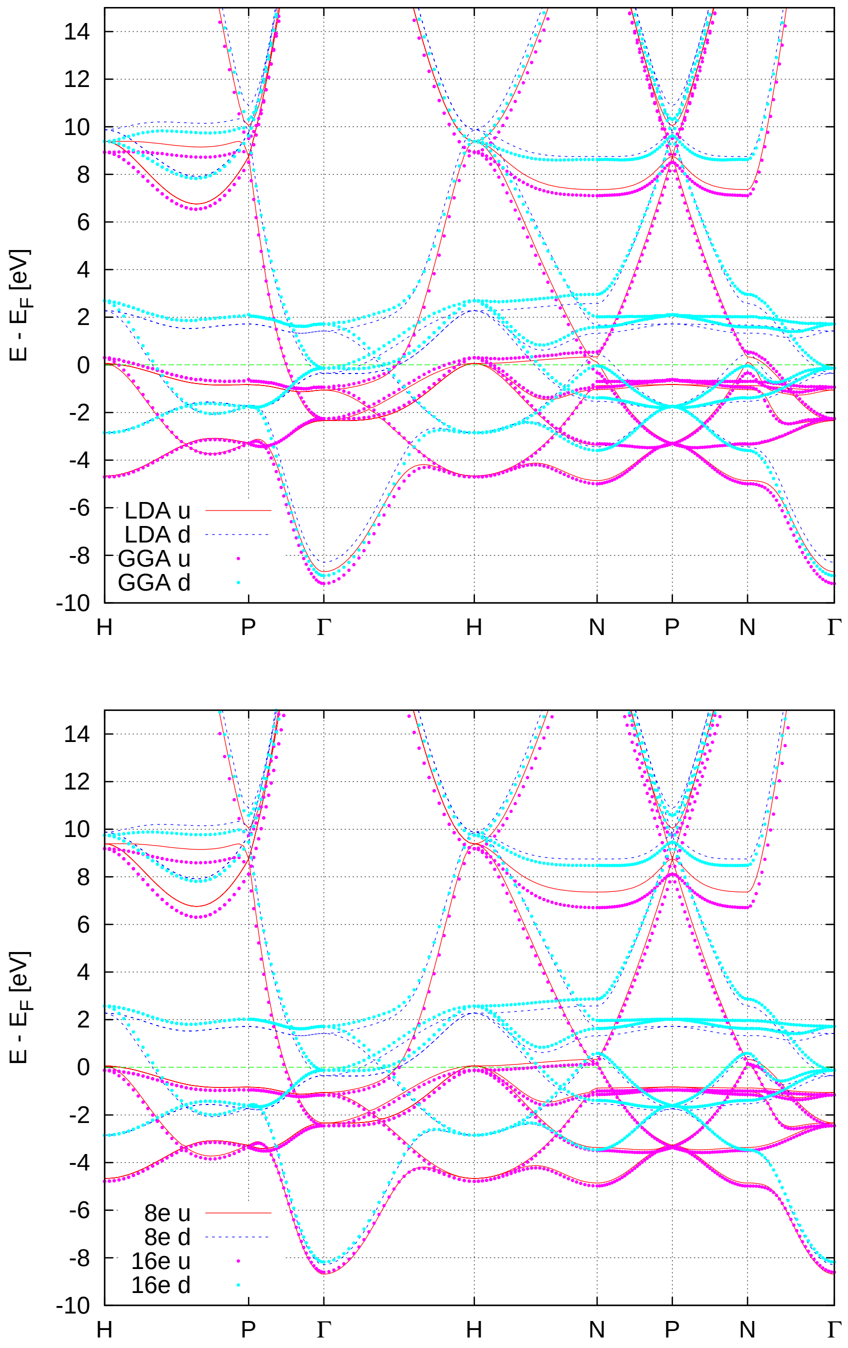

Figure 7.6: Spin resolved band structure (valence states) of BCC iron calculated at the experimental lattice paramter. Top: comparaison between GGA and LDA calculation; Bottom: comparaison between LDA calculations with and without semicore states.

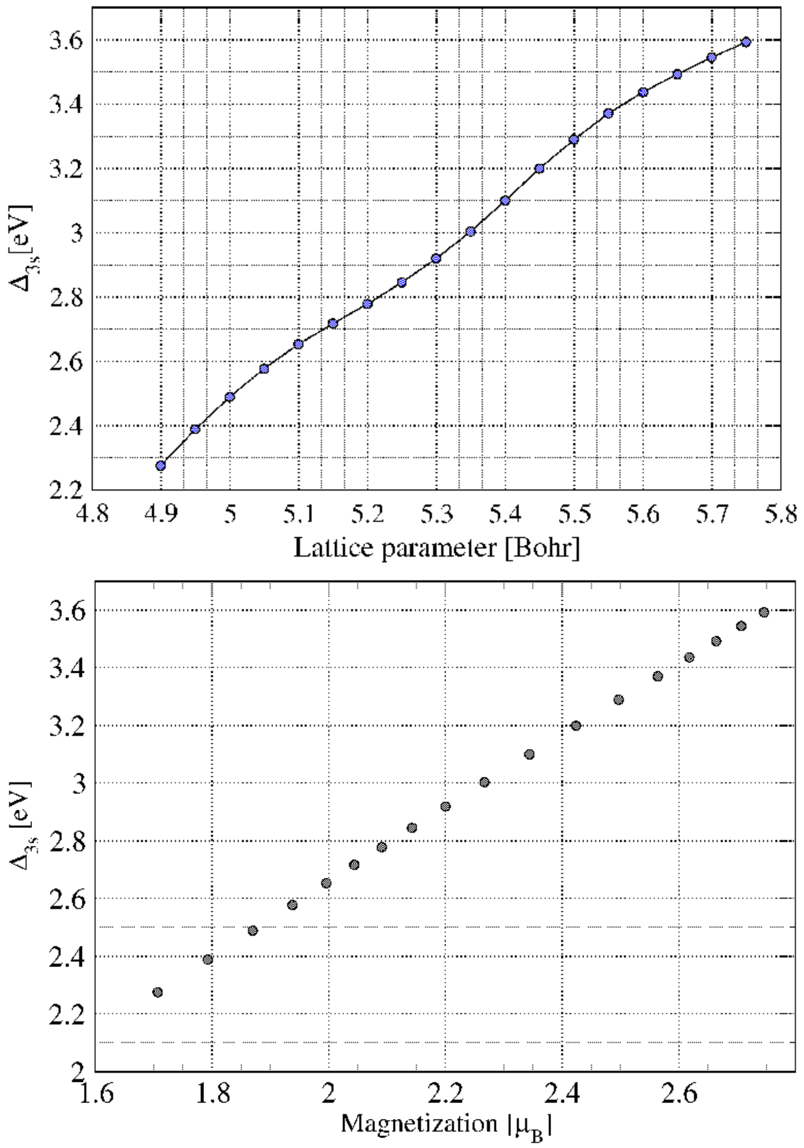

Figure 7.7: Splitting of 3s levels as a function of the lattice parameter (top panel) and the magnetization (bottom panel).

7.4 Optical conductivity

In this last section we report the calculations of the dielectric function ($\varepsilon = \varepsilon_1 + i\varepsilon_2$) obtained within the indipendent particle random phase approximation (IP-RPA) and including crystal local fields effects (RPA-LF). This quantity is closely related to the electronic structure and follows straightforward from theory, however experiments are often presented in terms of the optical conductivity ($\sigma = \sigma_1 + i\sigma_2$, see Refs. [168]). However, ε and σ are connected by the well known relations:

$$\sigma_1 = \frac{\varepsilon_2\omega}{4\pi} \tag{7.2}$$

$$\sigma_2 = \frac{(1-\varepsilon_1)\omega}{4\pi} \tag{7.3}$$

In Fig. 7.8 we show the optical conductivity of bulk iron calculated with the DP code [78]. There is a nice agreement between the calculated curves and the experimental data reported in Ref. [168] with respect to the general shape and the position of the maxima. We have not included any intraband contribution in our calculation and this is the reason why the sharp structure in the low–energy region of the experimental spectra is not reproduced (Fig. 7.8). We report, for comparison, a recent calculation of the optical conductivity including the Drude peak (see Ref. [169] for details about the treatment of the intraband transitions), in order to show that only the low energy part of the spectum is affected by this approximation.

Spin flip is also not allowed and this bring us to conclude that the maximum of the computed conductivity near 2.5 eV results from transitions between collinear spin states, in particular between states of the majority spin channel. It is easy to identify these excitations looking at Fig. 7.4: transitions connect occupied states and the unoccupied states just above the Fermi energy for the same spin channel (dashed line). Crystal local fields have negligible effects, and this is in agreement with the cases of others metals. As shown in Fig. 7.8 by the red and blue lines.

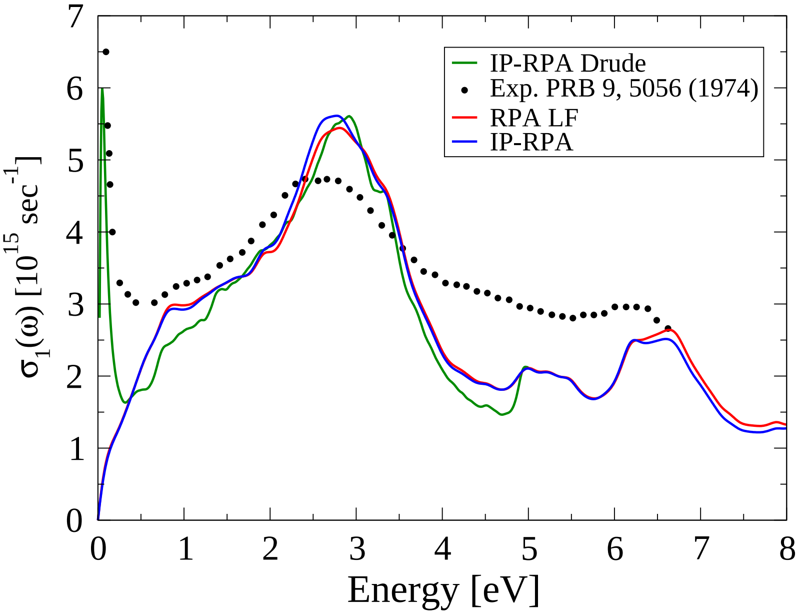

Figure 7.8: Comparison between optical conductivity experimental data from Refs. [168] and RPA calculation performed with the DP code [78]. Results with and without the inclusion of crystal local field effects (LF) are shown by the red and blue lines, respectively.

7.5 Conclusions

We succeeded in generating a set of pseudopotentials for iron, a prototypical transition metal for which an obvious separation between core and valence orbitals does not exist.

Semicore states have been either explicitly included in the valence set, or treated within the usual *non linear core corrections* scheme. Our set of PP has been tested against structural and electronic properties of BCC bulk iron, including the lattice constant, spin resolved density of states, band structure.

We also reported an analysis of the Fe-3s splitting with respect to the total magnetization. We found a linear dependence between these two quantities and between splitting and the lattice parameter. This results support the use of the s core-level splitting as a monitor of magnetization, and are compatible with a similar behaviour presented by non metallic transition metal compounds, rare earth metals and ionic compounds. Moreover we found that the 3s splitting calculated at the experimental value of the lattice parameter substantially agrees with XPS core level measurements reported in Ref. [161]. However the linear trend theoretically predicted is in apparent disagreement with experimental results where 3s XPS peak splittings do not correlate with the Fe magnetic moments.

Concerning the optical conductivity good agreement between RPA results and the experimental data is found. This allows one to conclude that the main spectral feature are well reproduecd by spin-collinear excitations.

Chapter 8

Iron, cobalt and nickel pyrites

Transition-metal pyrites form a series of compounds with a large variety in electrical, magnetic and optical properties. In particular, recently there has been a renewed interest in iron, cobalt and nickel disulfides because of their potential in future technological applications. Iron and nickel-controlled doping of CoS_2 gives rise to a tunable source of highly spin-polarized electrons [170]. This property is extremely interesting to design new devices exploiting the spin character of the electrons in addition to their charge. In fact the essence of the current focus area termed *spintronic*, or *spin-electronics*, is to use the electron's spin, as well as its charge in creating new devices or enhancing the functionality of the existing ones [171, 172].

In this section we will present structural, magnetic and electronic properties of FeS_2, CoS_2 and NiS_2 calculated within the density functional theory framework. A comparison of our results with respect to experimental data and to previous calculations is also discussed.

8.1 Motivations

The rapid developement of spin valve-based magnetic read heads and the emergence of spintronic [171, 172] has thrown up a need for a better understanding of spin-polarized materials [173].

Spintronic is based on the up or down spin of the carriers rather than on electrons or holes as in traditional semiconductors electronics. In particular spin-polarized transport will occur naturally in any material for which there is an imbalance of the spin populations at the Fermi level. This imbalance is present in ferromagnetic metals where the density of states for spin up and down electrons are shifted in energy with respect to each other. Commonly in these materials there is an unequal

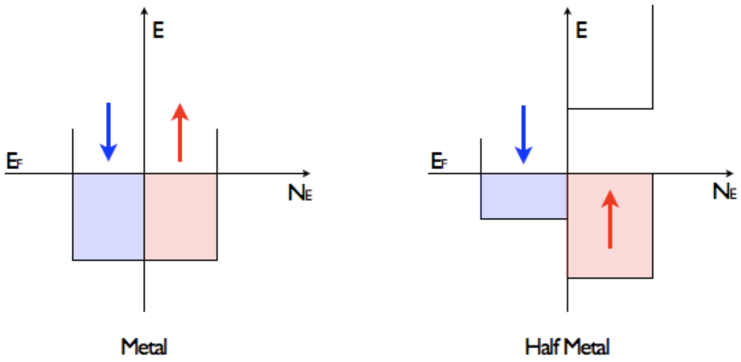

Figure 8.1: Schematic representation of the density of states in case of a metal (left) and an half metal (right).

filling of the bands, which is the source of the net magnetic moment, and causing the up and down carriers at the Fermi level to be different in number, character, and mobility. This inequality produces a net spin polarization but the sign and magnitude of that polarization depends on the specific material. Materials having at the Fermi level only one occupied spin band are usually called *half metals* (see Fig. 8.1).

A fundamental component in any spintronic device is a ferromagnetic electrode which is used as a source of polarized electrons, and an high value of spin polarization $P=(N_{\uparrow}-N_{\downarrow})/(N_{\uparrow}+N_{\downarrow})$ at the Fermi level can provide significant benefits. When the spin polarized electron current crosses a sample having a non zero total magnetization the only states that are available to the carriers are those for which the spins of the carriers are parallel to the spin direction of those states at the Fermi level. If the magnetization of the material is reversed, the spin direction of those states also reverses. Thus, depending on the direction of magnetization of a material relative to the spin polarization of the current, a material can be either a conductor or an insulator for electrons of a specific spin polarization (see Fig. 8.2).

The largest effect is generally seen for the most highly polarized currents, therefore, there are continuing efforts to find 100% spin-polarized conducting materials. However, partially polarized materials (such as Fe, Co, Ni and their alloys), are adequate to develop technologically useful devices and can show unexpected properties. For example, transition metal compounds have beed attracting extensive attention for that reason. Among them, FeS_2, CoS_2 and NiS_2 have been

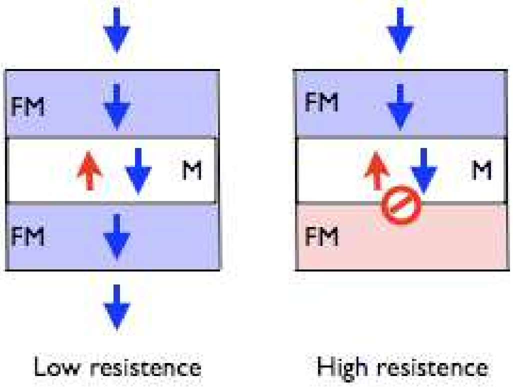

Figure 8.2: Schematic representation of spin polarized transport from a FM material to a metal and a FM material again. According to the reciprocal configuration of the spins, transport is allowed or forbidden.

studied from the experimental [174, 175, 176, 177] and theoretical [178, 179, 180] point of view. Moreover these compounds have been used to build and to study $Co_{1-x}Fe_xS_2$ and $Ni_{1-x}Co_xS_2$ compounds, recently predicted to be tunable half metals (see Refs. [181, 177, 182, 183, 184] for a review of works on $Co_{1-x}Fe_xS_2$ and Ref. [185] for $Ni_{1-x}Co_xS_2$).

In the following sections we will focus on structural and magnetic properties of FeS_2 and CoS_2, as a first step to be able in the future to describe more complex compounds.

8.2 Structural and magnetic properties

All transition metal disulfides (MS_2 with M a $3d$–transition metal atom), crystallize in a cubic pyrite structure of space group $T_h^6(Pa3)$ in which metal atoms are located in face-centred postions. Structure can be considered as an NaCl-like grouping of metal and chalcogen atom pairs (sulfurs). In Fig. 8.3 the atoms arrangement is shown from three perpendicular views. Every metal atoms (dark grey circles) is surrounded by six nearest-neighbour sulfurs in a distorted octahedral environment, while each sulfur (light grey circles) bonds to one sulfur (S-S bond) and three metals in a distorted tetrahedral arrangement. Distance of sulfur–sulfur pairs (S–S) is short because of a covalent bond. The formation of S–S pairs is characteristic feature of these structures.

In particular metal atoms are located at the positions (0,0,0), (0,1/2,1/2), (1/2,0,1/2) and (1/2,1/2,0), the eight sulfur atoms instead are located at position $\pm(u, u, u)$, $\pm(u + 1/2, 1/2 - u, \bar{u})$, $\pm(\bar{u}, u + 1/2, 1/2 - u)$, $\pm(1/2 - u, \bar{u}, u + 1/2)$. The values of u and a (the lattice parameter) are taken from Wyckoff [186], in particular we used $u = 0.386$ and $a = 5.407$ Å in case of FeS_2, $u = 0.389$ and $a = 5.524$ Å in case of

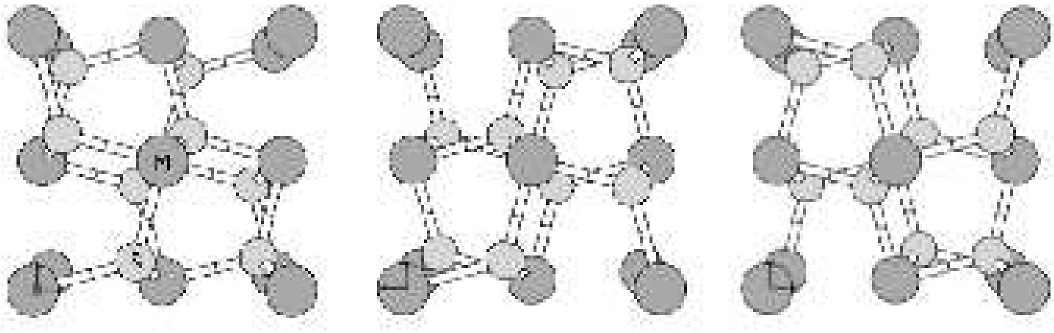

Figure 8.3: Atoms rearrangement in pyrite structure along three orthogonal directions. Dark grey circles represent metal atoms, smaller light grey circles depict sulfur atoms. Graphs are generated with Xcrysden package [136].

System	a_0 [Å] Ref. [186]	S–S [Å] this work	S–S [Å] from Ref. [178]	μ/at. [μ_B] this work	μ/at. [μ_B] Ref. [174, 181]
FeS_2	5.407	2.18	2.14	$\simeq 0$	$\simeq 0$
CoS_2	5.524	2.29	2.12	0.98	0.9
NiS_2	5.677	2.06	2.06	0	-

Table 8.1: Optimized S–S distances calcluated for FeS_2, CoS_2 and NiS_2 are compared with values reported in Ref. [178]. The calculated ground state magnetization per metal atom is compared to experimental values reproduced from Ref. [174, 181]

CoS_2 and $u = 0.395$ and $a = 5.677$ Å in case of NiS_2.

We performed a geometric optimization using the BFGS algorithm [141, 142, 143, 144] with the ABINIT [68] code. The optimized S–S distances of FeS_2, CoS_2 and NiS_2 are reported in Tab. 8.1, and compared with values reported in Ref. [178]. All the ground state calculations have been performed within the DFT-GGA framework (Perdew-Burke-Ernzerhof (PBE) parametrization [9]) with a cutoff energy $E_{\text{cut}} = 34$ Ha. The geometry relaxation is performed by setting a tolerance of 0.02 on the ratio of differences of forces to maximum force, reached twice successively, will cause a self consistent cycle to stop. The agreement of the computed S–S distance with respect to previous calculations is reasonable, as listed in Tab. 8.1. Moreover, Figure 8.4 shows the electronic density distribution for a suitable value of the chosen isosurfaces in order to evidence the formation of the characteristic S–S

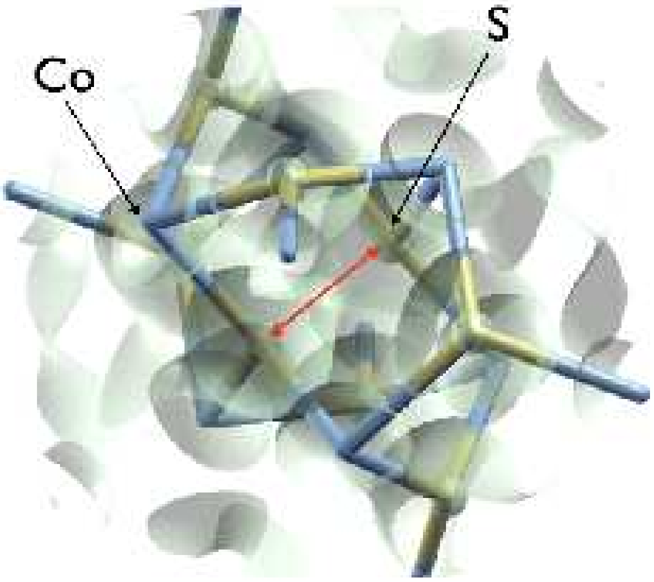

Figure 8.4: Isosurfaces of electronic density (grey regions) around the atoms of CoS_2. Cobalt atoms (light blue) and sulfur atoms (yellow) are represented inside the crystal structure. The point of view is chosen in order to evidence the characteristic S–S bond in the center of the crystal (red arrows). Graphs are generated with the Xcrysden package [136].

bond in the center of the crystal structure.

The magnetic character of the electronic ground state of all the compounds has been also analyzed. The values of total magnetization per metal atom are reported in Tab. 8.1 with experimental reference values reproduced from literature.
The three compounds display different behaviours: FeS_2 presents a total magnetization close to zero, CoS_2 has a ferromagnetic ground state with total magnetization per cobalt atom close to 1 μ_B, and NiS_2 is non–magnetic. Experimental studies on transition metal disulfides (see Ref. [174]) revealed the non magnetic nature of all this class of compounds, except for the case of CoS_2. Experiments indicate that FeS_2 as well as NiS_2 are paramagnetic semiconductors. In addition, at low temperature NiS_2 presents a transition to an antiferromagnetic phase.
Our calculations predict correctly this behaviour. In particular for CoS_2 we find a ground state electronic configuration with a total magnetic moment μ =0.98 μ_B per cobalt atom at T=0° K, which is close to the experimental value μ =0.9 μ_B (see Ref. [174]).

In addition we report in Fig. 8.5 the electronic density isosurfaces that evidences the distribution of spin up and spin down components. In the case of FeS_2 the spin up and down charge distributions are located at the same positions without any

motif distinguishig between the two components. On the contrary, in case of CoS_2 it is possible to appreciate a regular ordering of the electronic density distribution according to the two spin components (red and blue respectively in Fig. 8.5). The maxima of the distributions are located at the metal sites of the crystal and the up-down spin density is alternated in adiacent sites.
NiS_2 still presents a regular ordering of the spin density distributions but, as the total magnetization is found to be zero, suggests an antiferromagnetic character. Even if the study of NiS_2 is beyond the scope of this thesis, we notice that this result is in agreement with Ref. [174].

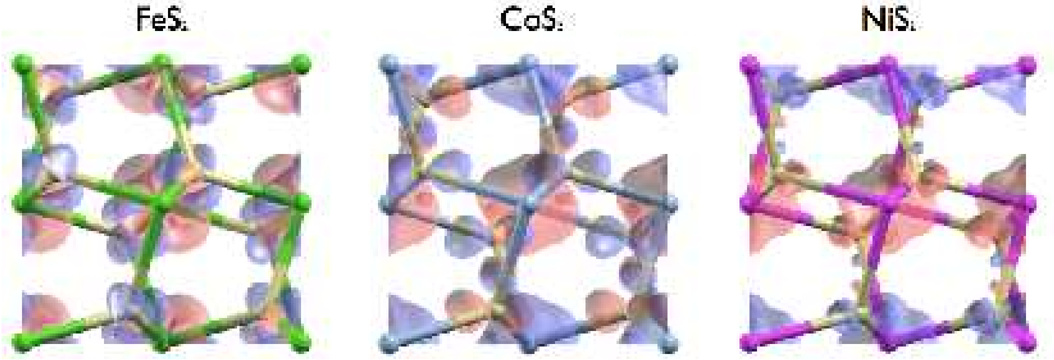

Figure 8.5: Electronic density isosurfaces for the up (red) and down (blue) spin component for FeS_2 (left), CoS_2 (center) and NiS_2 (right). Graphs are generated with the Xcrysden package [136].

8.3 Electronic properties

In order to analyze the electronic properties of FeS_2, CoS_2 and NiS_2 we calculated the spin resolved density of state (DOS) within DFT-GGA (PBE parametrization). The software ABINIT [68] has been used in order to perform convergence study and calculate the final distribution. For FeS_2 we used a Monkorst Pack [83] grid of $12 \times 12 \times 12$ $\mathbf{k}$ points in the Brillouin zone (BZ), corresponding to 76 $\mathbf{k}$, applying a rigid shift of 0.5 in the three spatial directions. For CoS_2 the grid consisted of $10 \times 10 \times 10$ $\mathbf{k}$ points and $6 \times 6 \times 6$ for NiS_2. A thermal broadening (cold smearing) $tsmear = 0.007$ Ha is applied to simulate the metallic occupation of levels following

the recipe of Ref. [187][1].
Density of states are calculated using the tetrahedron method giving a faster convergence over the number of **k** poins required with respect to the standard integration over the Brillouin zone.

In Fig. 8.6 the DOS of FeS_2, CoS_2 and NiS_2 are shown. The three compounds present a similar density of states but different electronic behaviour. We discuss now our results that are in general agreement with experimental works [175, 176, 188] and theoretical calculations based on linear combination of atomic orbital (LCAO) or semiempirical and self-consistent tight-binding (TB) approach [178, 179, 189].
The first two lowest energy bands are associated with bonding and antibonding pairs of orbitals of the sulfur atom dimers (sσ and sσ^* orbitals). The following complex structure is due to sulfur $3p$ and the metal $3d$ orbitals. Then the crystal field of the disulfide anions (sulfurs) splits the cation (metal) $3d$ non–bonding orbitals into three low-lying $3d(t_{2j})$ and two higher-energy $3d(e_g)$ levels (see Fig. 8.6).
All the disulfides studied have completely filled $3d(t_{2j})$ orbitals, and as the atomic number increases the additional electrons (none for iron, one for cobalt and two for nickel) fill in the $3d(e_g)$ orbitals. The different filling of these bands determine the electronic nature of the three compounds studied.

In particular, our calculations predict FeS_2 as a small band gap semiconductor, in agreement with experiments (optical and conductivity measurements [176] and X–ray photoemission spectoscopy [175, 190]) and theoretical works [178, 179]. From our calculations the value of the FeS_2 band gap turns out to be 1.2 eV and 0.98 eV for the spin-up and spin-down components respectively (Fig. 8.6, top panel). Even if a more detailed analysis including band structure calculations is required, we can already conclude that the calculated values are close to the experimental ones ranging from 0.9 eV to 1.2 eV (see Ref. [176]) and for which there is no general consensus. Difficulties in the exact experimental determination of the band gap of FeS_2 could rise because of a large difference between the indirect and direct gap as pointed out by Zhao *et al.* [179]. In fact in that work all calculations in the local density approximation lead to a minimum indirect gap $E_{ig} = 0.59$ eV and to a smallest direct gap $E_{dg} = 0.74$ eV.

Concerning CoS_2, we found similar structures for low-energy states with respect to FeS_2, but shifted to lower energies (see Fig. 8.6, central panel). Moreover our DFT-GGA calculations confirm the half metallic nature of CoS_2, where the two spin components present density of states characteristic of a semiconductor (red line) or a metal (blue line). In Fig. 8.6 the Fermi energy is set to zero for clarity.

---

[1] The smeared delta function is defined by: $\delta_s = \frac{1}{\sqrt{\pi}} e^{-x^2} \left(ax^3 - x^2 - \frac{3}{2}ax + \frac{3}{2} \right)$ where $a = -0.5634$, this choice minimizes the bump.

It is worth to mention that half–metallicity of CoS_2 has been recently discussed in literature from both the experimental and theoretical points of view. Direct measurements of spin polarization and magnetotransport [170] show that CoS_2 is not completely polarized (i.e. $P = \frac{N_\uparrow(E_F)+N_\downarrow(E_F)}{N_\uparrow(E_F)-N_\downarrow(E_F)}$ is not large). On the contrary, the temperature variation of the electronic structure, studied by means of optical reflectivity measurements confirms the half metallicity of the compound. From the theoretical point of view Shishidou *et al.* [180] presented a detailed comparison between LDA and GGA electronic structure calculations within density functional, full potential linearized augmented plane waves calculations. In that work the authors conclude that GGA greatly modifies the LDA band structure from metallic to half metallic. These conclusions are in agreement with our finding displayed in Fig. 8.6.

In the case of NiS_2 the spin density of states presents a symmetric behaviour that

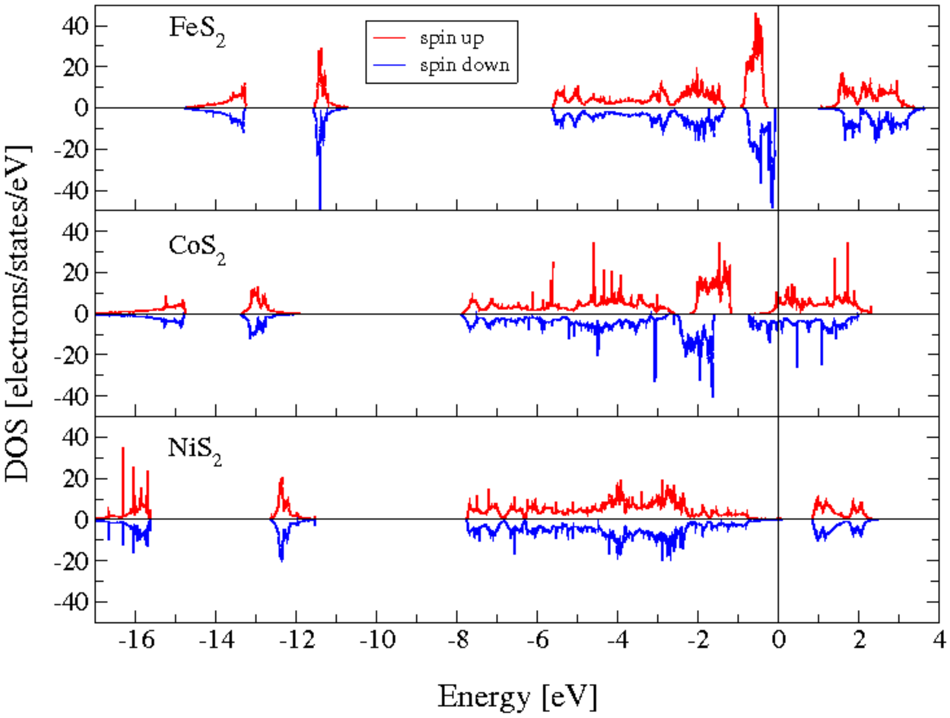

Figure 8.6: Spin resolved density of states of FeS_2, CoS_2, NiS_2 calculated with tethraedron method with the software ABINIT [68].

confirm the apparently non magnetic nature of that compound and the zero total magnetization obtained from our calculations (see sec. 8.2). However, as underlined preivously, NiS_2 presents a local regular ordering of the spin density distribution justifying its antiferromagnetic nature (see Refs. [191]). Among the transition metal disulfides, NiS_2 is considered to be a Mott-Hubbard insulator [192]. For that reason more specific theories are required in order to correctly describe NiS_2 properties.

8.4 Conclusions

We presented a systematic study of structural, magnetic and electronic properties of FeS_2, CoS_2 and NiS_2, three examples of 3d-transition metal sulphides with cubic pyrite structure. As anticipated in the introduction of this chapter, the interest on these systems is recenlty renewed, due to the great potential of such systems for spintronic applications.

From our calculations we obtained the S–S relaxed distance, characteristic of these compounds, the ground state total magnetization and the spin resolved density of states. We correctly predict that CoS_2 is the sole magnetic system of this class of compounds, with a total magnetization per metal atom μ =0.98μ_B, in agreement with experimental values. On the contrary FeS_2 and NiS_2 do not show any total magnetization, the former being non–magnetic and the latter presenting locally a regular arrangement of the two spin components of the electronic density distribution, typical of an antiferromagnetic material. Moreover DOS calculated for CoS_2 is typical of an half metal, while FeS_2 and NiS_2 typical of small band gap semiconductors.

All these results are in nice agreement with experimental data and previous theoretical calculations.

These results now open the way to study also the optical properties of such compounds.

In conclusion, as anticipated in the introduction of this chapter, the interest on these systems is recenlty renewed due to the great potential for the emerging spintronic technological applications. In fact, when CoS_2 is doped with iron or nickel in a solid solution like $Co_{1-x}Fe_xS_2$ or $Co_{1-x}Ni_xS_2$. the metal to semiconductor transition can be tuned increasing the iron or nichel concentration. Moreover the spin polarization can be controlled generating an highly polarized electron source [177, 181, 182, 183, 184, 185].

Conclusions

This thesis is devoted to *ab initio* calculations of ground state and excited state properties of realistic systems within the density functional theory (DFT) and its Time Dependent generalisation (TDDFT).

We used *theoretical spectroscopy* tools in order to study several systems with different dimensionality (surfaces, molecules, bulk crystals). Starting with the dielectric function $\varepsilon(\omega)$, obtained by the response function in linear regime, we calculated the anisotropy reflectivity (RA) spectra and the reflectance electron energy loss (REEL) spectra for the Si(100) clean and oxidized surfaces. In the case of the clean surface, we considered three surface reconstructions $p(2 \times 1)$, $p(2 \times 2)$ and $c(4 \times 2)$. Thanks to the comparison between experiments and numerical simulation, we were able to rule out the $p(2 \times 1)$ reconstruction and to define the origin of the REEL peaks without ambiguity.

In the second part of the work, we evidenced the problem of the correct description of excitation spectra of open shell molecules within DFT–LDA. We calculated the energy levels and the first excitation energies for the BeH molecule in the TDDFT framework. These calculations have been a first step in order to approach the case of magnetic metals and half metals. In fact, this part of the work was dedicated to the study of optical properties of magnetic iron alloys, that are very interesting materials for new applications in the spintronic domain.

In this framework we evaluated ground state properties and conductivity of the bcc crystal phase of iron in order to validate the theoretical approach comparing the results with experimental data.

Finally we studied the ground state properties of some $3d$–transition metal disulfides, i.e. FeS_2, CoS_2 and NiS_2, having a commun cubic pyrite structure but different electronic and magnetic properties. Starting from these compounds it is possible to create more complex systems such as iron or nickel doped CoS_2 alloys, that are interesting for the design of new technological devices based on spin electronics.

From the numerical point of view, we implemented an original method in the large scale ab initio code DP in order to calculate the indipendent particle dynamical response function $\chi^0(\mathbf{r}, \mathbf{r}', \omega)$, built from the eigenvalues and eigenvectors of the Kohn and Sham hamiltonian. We have demostrated that the method, based on the Hilbert transform, is efficient for large size systems, as in the case of surfaces. Moreover, we have generalized the code to spin variable in order to study magnetic properties of realistic applications.

Milano, December 2008

Scientific contributions

List of papers

- L. Caramella, G. Onida, F. Finocchi, L. Reining and F. Sottile *Optical properties of real surfaces: Local-field effects at oxidized Si(100)(2×2) computed with an efficient numerical scheme*, Phys. Rev. B **75**, 205405 (2007).
  (See chapter 3)
  It has been published also in "Virtual Journal of Nanoscale Science & Technology", 14 May 2007,Volume 15 issue 19.

- L. Caramella, G. Onida and C. Hogan, *Dielectric response and electron energy loss spectra of an oxidized Si(100)(2×2) surface*, in Epioptics-9, The Science and culture, ed. by A. Cricenti, World Scientific, Singapore 2008, Vol. 29, p. 62.
  (See chapter 4)

- L. Caramella, D. Tavella and G. Onida *Norm conserving pseudopotentials for iron with semicore states* sumbitted (2008).
  (See chapter 7)

- L. Caramella, C. Hogan, G. Onida and R. Del Sole *Calculation of High Resolution EEL Spectra of reconstructed Si(100) surfaces*, to be submitted (2008).
  (See chapter 4)

- C. Hogan, L. Caramella, G. Onida and R. Del Sole *Electron energy loss of the oxidized Si(100) surface*, in preparation (2008).
  (See chapter 5)

- L. Caramella, D. Sangalli, G. Onida *et al.* *Subtleties in electronic excitations of open shell molecules*, in preparation (2008).
  (See chapter 6)

- L. Caramella *et al.* *Optical properties of* FeS_2 *and* CoS_2, in preparation (2008). (See chapter 8)

Selected oral contributions to conferences

- International School of Solid State Physics - Epioptics-10, 20–27, June 2008, Erice (Italy): *Ab initio calculation of loss function of clean and oxidized silicon surfaces.*
- 5th Nanoquanta Young Researchers' Meeting, 20–23, May 2008, Modena (Italy): *Quantitative predictions of Electron Energy Loss Spectra at the Si(100) surface*
- 4th Nanoquanta Young Researchers' Meeting, 15–18, May 2007, San Sebastian (Spain): *Optical properties of real surfaces: local field effects at oxidized Si(100)(2×2) computed with an efficient numerical scheme*
- Réunion Général du GDR DFT ++, 27–30, March 2007, L'Escandille, Autrans (France):*Optical properties of real surfaces: local field effects at oxidized Si(100)(2×2) computed with an efficient numerical scheme.*
- APS March Meeting, 5–9, March 2007, Denver (Colorado):*Optical properties of real surfaces: local field effects at oxidized Si(100)(2×2) computed with an efficient numerical scheme.*
- International School of Solid State Physics - Epioptics-9, 20–26, July 2006, Erice (Italy):*Application of an efficient numerical scheme for the computation of response functions to study the optical properties of the oxidized Si(100)(2×2) surface.*
- 10th Nanoquanta General Meeting, 12–15, September 2005, Bad Honnef (Germany):*A Hilbert transform–based scheme for the efficient computation of response functions and its application to study the optical properties of the oxidized Si(100)(2×2) surface.*

Appendix A

Determination of second derivative spectra

We implemented a Savitski–Golay (SG) smoothing algorithm [193] in order to compute the derivative spectra.
The SG algorithm fits the EEL curve with polynomials preserving spectral features:

$$g_i = \sum_{n=-n_L}^{n_R} c_N f_{i+N} \tag{A.1}$$

where g_i represents the smoothed function, and c_N the coefficients obtained by the coefficient matrix of polynomial of degree M by the relation:

$$c_N = (A^T A)^{-1}(A^T e_n)_0 \tag{A.2}$$

where $A_{ij} = i^j$ is the coefficient matrix of polynomial of degree M and e_n is the unit vector. Then SG algorithm returns the derivative of k-degree of the smoothed curve. When $k > 1$ the coefficients in equation A.1 have to be normalized replacing c_N with $c_N k!$.
Smoothing step is required to correctly identify the physical EEL peaks, in fact, derivative can dramatically enhance the noise of the EEL spectra due to the discrete k point sampling. See Fig. A.1 for an example of the method.

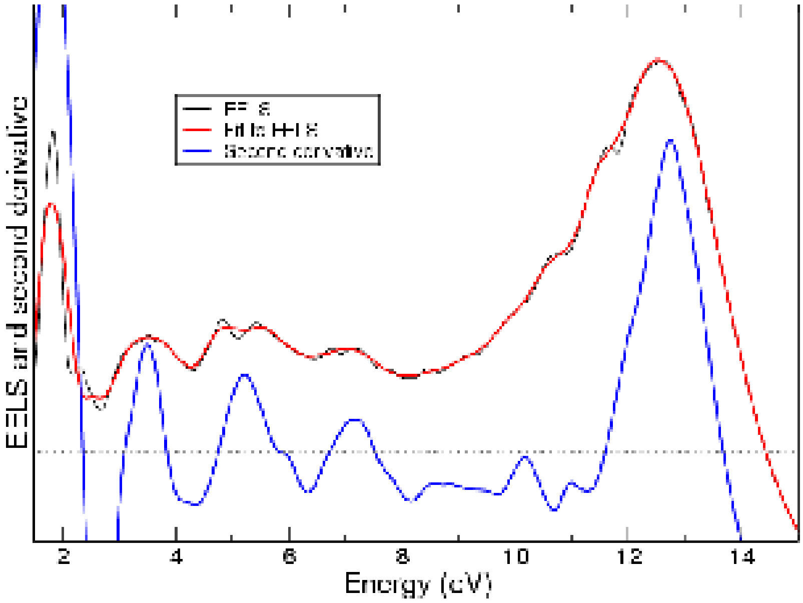

Figure A.1: Computation of the second derivative spectra (blue line) of a typical EEL spectrum. The bare EEL spectrum (black line) and the resulting fit with polynomials (red line) are also shown.

Bibliography

[1] W. Kohn and L. J. Sham *Phys. Rev.*, vol. 140, p. A1113, (1965).

[2] P. Hohenberg and W. Kohn *Phys. Rev.*, vol. 136, p. B864, (1964).

[3] G. Onida, L. Reining, and A. Rubio *Rev. of Mod. Phys.*, vol. 74, p. 601, 2002.

[4] G. Gross and G. Pastori Parravicini, *Solid State Physics.* Academic press, London UK, 2000.

[5] D. M. Ceperley and B. J. Alder *Phys. Rev. Lett.*, vol. 45, p. 566, (1980).

[6] D. M. Ceperley and B. J. Adler *Phys. Rev. Lett.*, vol. 45, pp. 566–569, 1980.

[7] J. P. Perdew and A. Zunger *Phys. Rev. B*, vol. 23, p. 5048, (1981).

[8] J. P. Perdew, K. Burke, and Y. Wang *Phys. Rev. B*, vol. 54, p. 16533, 1996.

[9] J. P. Perdew, K. Burke, and M. Ernzerhof *Phys. Rev. Lett.*, vol. 77, p. 3865, 1996.

[10] J. C. Phillips and L. Kleinman *Phys. Rev.*, vol. 116, no. 2, p. 287, 1959.

[11] D. R. Hamann, M. Schlüter, and C. Chiang *Phys. Rev. Lett.*, vol. 43, p. 1494, 1979.

[12] G. P. Kerker *J. Phys. C*, vol. 13, p. L189, 1980.

[13] G. B. Bachelet, D. R. Hamann, and M. Schlüter *Phys. Rev. B*, vol. 26, no. 8, p. 4199, 1982.

[14] L. Kleinman and Bylander *Phys. Rev. Lett.*, vol. 48, p. 1425, 1982.

[15] D. Vanderbildt *Phys. Rev. B*, vol. 41, p. 7892, 1990.

[16] P. E. Blochl *Phys. Rev. B*, vol. 41, p. 5414, 1990.

[17] X. Gonze, R. Stumpf, and M. Scheffler *Phys. Rev. B*, vol. 44, p. 8503, 1991.

[18] L. Kleinman *Phys. Rev. B*, vol. 21, p. 2630, 1980.

[19] S. B. Louie, S. Froyen, and M. L. Cohen *Phys. Rev. B*, vol. 26, p. 1738, 1982.

[20] N. Troullier and J. L. Martins *Phys. Rev. B*, vol. 43, p. 1993, 1991.

[21] D. R. Hamann *Phys. Rev. B*, vol. 40, no. 5, p. 2980, 1989.

[22] M. Fuchs and M. Scheffler *Comp. Phys. Comm.*, vol. 119, pp. 67–68, 1999.

[23] E. Runge and E. K. U. Gross *Phys. Rev. Lett.*, vol. 52, p. 997, 1984.

[24] E. Runge and W. Kohn *Phys. Rev. Lett.*, vol. 82, p. 55, 1985.

[25] M. A. L. Marques, C. A. Ullrich, F. Nogueira, A. Rubio, K. Burke, and E. Gross, *Time-Dependent Density Functional Theory*, vol. 706. Springer-Verlag (Berlin), 2006.

[26] H. Luth, *Solid Surfaces, Interfaces and Thin Films.* Springer–Verlag (Berlin), 1993.

[27] A. Zangwill, *Physics at Surfaces.* Cambridge University Press (Cambridge), 1988.

[28] F. Bechstedt, *Principles of Surface Physics.* Springer–Verlag (Heidelberg), 2003.

[29] Notes from the course *Fisica delle Superfici.*

[30] C. M. Bertoni, *Interaction of atoms and molecules with solid surfaces*, ch. Basic structural and electronic properties of semiconductor surfaces. Plenum Publishing Corporation, 1990.

[31] J. R. Power, O. Pulci, A. I. Shkrebtii, S. Galata, A. Astropekakis, K. Hinrichs, N. Esser, D. S. R., and W. Richter *Phys. Rev. B*, vol. 67, p. 115315, (2003).

[32] A. Hemeryck, A. Mayne, N. Richard, A. Esteve, Y. Chabal, M. Djafari Rouhani, D. G., and G. Comtet *J. Chem. Phys.*, vol. 126, (2007).

[33] R. Del Sole, *Photonic Probes of Surfaces.* Elsevier (Amsterdam), 1995.

[34] O. Pluchery, N. Witkowski, and B. Y. *Phys. Stat. Sol. (b)*, vol. 424, p. 2696, (2005).

[35] S. G. Jaloviar, J.-L. Lin, F. Liu, V. Zialesk, L. McCaughan, and M. G. Lagally *Phys. Rev. Lett.*, vol. 82, p. 791, 1999.

[36] R. Shioda and J. van der Weide *Phys. Rev. B*, vol. 57, p. R6823, (1998).

[37] R. Del Sole, W. L. Mochan, and R. G. Barrera *Phys. Rev. B*, vol. 43, p. 2136, (1991).

[38] C. Hogan, R. Del Sole, and G. Onida, "Optical properties of real surfaces from microscopic calculations of the dielectric function of finite atomic slab," *Phys. Rev. B*, vol. 68, p. 035405, (2003).

[39] H. Ibach and D. L. Mills, *Electron Energy loss spectroscopy and surface vibrations.* Academic press, 1982.

[40] A. Selloni and R. Del Sole *Surf. Sci.*, vol. 186, p. 35, (1986).

[41] M. Palummo, O. Pulci, A. Marini, L. Reining, and R. Del Sole, "Ab initio calculation of many-body effects on the eel spectrum of the c(100) surface," *Phys. Rev. B*, vol. 74, p. 235431, 2006.

[42] L. Hedin *Phys. Rev.*, vol. 139, p. A796, 1965.

[43] T. Miyake and F. Aryasetiawan *Phys. Rev. B*, vol. 61, p. 7172, 1999.

[44] M. Shishkin and G. Kresse *Phys. Rev. B*, vol. 74, p. 035101, 2006.

[45] P. E. Blochl *Phys. Rev. B*, vol. 50, p. 17953, 1994.

[46] D. Foerster *Phys. Rev. B*, vol. 72, p. 073106, (2005).

[47] D. E. Aspnes and A. A. Studna *Phys. Rev. Lett.*, vol. 54, p. 1956, (1985).

[48] W. L. Mochan and G. Barrera *Phys. Rev. Lett.*, vol. 55, p. 1192, (1985).

[49] W. G. Schmidt and J. Bernholc *Phys. Rev. B*, vol. 61, p. 7604, (2000).

[50] G. Onida and R. Del Sole *Phys. Rev. B*, vol. 60, p. 5523, (1999).

[51] P. H. Hahn, W. G. Schmidt, and F. Bechstedt *Phys. Rev. Lett.*, vol. 88, p. 016402, (2002).

[52] W. G. Schmidt, S. Glutsch, P. H. Hahn, and F. Bechstedt *Phys. Rev. B*, vol. 67, p. 085307, (2003).

[53] M. Palummo, O. Pulci, R. Del Sole, A. Marini, M. Schwitters, S. R. Haines, K. H. Williams, D. S. Martin, P. Weightman, and J. E. Butler *Phys. Rev. Lett.*, vol. 94, p. 087404, (2005).

[54] H. Watanabe, K. Kato, T. Uda, K. Fujita, M. Ichikawa, T. Kawamura, and K. Terakura *Phys. Rev. Lett.*, vol. 80, p. 345, (1998).

[55] N. K., Y. Okazaki, and K. Kimura *Phys. Rev. B*, vol. 63, p. 113314, (2001).

[56] S. Dreiner, M. Schurmann, and C. Westphal *Phys. Rev. Lett.*, vol. 93, p. 126101, (2004).

[57] T.-W. Pi, J.-F. Wen, C.-P. Ouyang, R.-T. Wu, and G. K. Wertheim *Surf. Sci.*, vol. 478, p. L333, (2001).

[58] A. Yoshigoe and Y. Teraoka *Surf. Sci.*, vol. 32, p. 690, (2003).

[59] H. Ikegami, K. Ohmori, H. Ikeda, H. Iwano, S. Zaima, and Y. Yasuda *Jpn. J. Appl. Phys.*, vol. 35, p. 1593, (1996).

[60] H. Itoh, K. Nakamura, A. Kurokawa, and S. Ichimura *Surf. Sci.*, vol. 482, p. 114, (2001).

[61] T. Uchiyama, T. Uda, and K. Terakura *Surf. Sci.*, vol. 433, p. 896, (1999).

[62] K. Kato and T. Uda *Phys. Rev. B*, vol. 62, p. 15978, (2000).

[63] Dreiner, N. Richard, A. Estève, and M. Djafari-Rouhani *Comput. Mat. Sci.*, vol. 33, p. 26, (2005).

[64] Y. J. Chabal, K. Raghavachari, X. Zhang, and E. Garfunkel *Phys. Rev. B.*, vol. 66, p. 161315(R), (2002).

[65] Y. Widjaja and C. B. Musgrave *J. Chem. Phys.*, vol. 116, p. 5774, (2002).

[66] L. C. Ciacchi and M. C. Payne *Phys. Rev. Lett.*, vol. 95, p. 196101, (2005).

[67] A. Incze, R. Del Sole, and O. G. *Phys. Rev. B*, vol. 71, p. 035350, (2005).

[68] `http://www.abinit.org`.

[69] L. Reining, V. Olevano, A. Rubio, and G. Onida *Phys. Rev. Lett.*, vol. 88, p. 066404, (2002).

[70] F. Bruneval, F. Sottile, V. Olevano, R. Del Sole, and L. Reining *Phys. Rev. Lett.*, vol. 94, p. 186402, (2005).

[71] G. Adragna, R. Del Sole, and A. Marini *Phys. Rev. B*, vol. 68, p. 165108, (2003).

[72] R. Del Sole, G. Adragna, V. Olevano, and L. Reining *Phys. Rev. B*, vol. 67, p. 045207, (2003).

[73] R. Stubner, I. V. Tokatly, and O. Pankratov *Phys. Rev. B*, vol. 70, p. 245119, (2004).

[74] F. Sottile, K. Karlsson, L. Reining, and F. Aryasetiawan *Phys. Rev. B*, vol. 68, p. 205112, (2003).

[75] S. Baroni and R. Resta *Phys. Rev. B*, vol. 33, p. 7017, (1986).

[76] H. Ehrenreich and H. M. Cohen *Phys. Rev.*, vol. 115, p. 786, (1959).

[77] B. Walker, A. M. Saitta, R. Gebauer, and S. Baroni *Phys. Rev. Lett.*, vol. 96, p. 113001, (2006).

[78] `http://www.dp-code.org`.

[79] `http://www.etsf.eu`.

[80] K. Gaal-Nagy, A. Incze, G. Onida, Y. Borensztein, N. Witkowski, O. Pluchery, F. Fuchs, F. Bechstedt, and R. Del Sole, "Optical spectra and microscopic structure of the oxidized si(100) surface: combined in–situ optical experiments and first principle calculations," *in preparation.*

[81] N. Witkowski, O. Pluchery, Y. Borensztein, K. Gaal-Nagy, A. Incze, G. Onida, F. Fuchs, F. Bechstedt, and R. Del Sole, "All–optical determination of initial oxidation of si(100) and its kinetics," *Eur. Phys. Journal B*, vol. 66, p. 427, 2008.

[82] T. Nakayama and M. Murayama *Appl. Phys. Lett.*, vol. 77, p. 26, (2000).

[83] H. J. Monkhorst and J. D. Pack *Phys. Rev. B*, vol. 13, p. 5188, (1976).

[84] S. Botti, N. Vast, L. Reining, V. Olevano, and L. G. Andreani, "Ab initio calculations of the anisotropic dielectric tensor of $gaas/alas$ superlattices," *Phys. Rev. Lett.*, vol. 89, p. 216803, 2002.

[85] A. G. Marinopoulos, L. Reining, V. Olevano, A. Rubio, T. Puchler, X. Liu, M. Knupfer, and J. Fink *Phys. Rev. Lett.*, vol. 94, p. 219701, (2005).

[86] F. Sottile *Int. J. of Quant. Chem.*, vol. 102, p. 684, (2005).

[87] F. Bruneval, S. Botti, and L. Reining *Phys. Rev. Lett.*, vol. 94, p. 219701, (2005).

[88] Y. Borensztein *Phys. stat. sol. (a)*, vol. 7, p. 1313, (1005).

[89] T. Yasuda, S. Yamasaki, M. Nishizawa, N. Miyata, A. Shklyaev, M. Ichikawa, T. Matsudo, and T. Ohta *Phys. Rev. Lett.*, vol. 87, p. 037403, (2001).

[90] T. Yasuda, M. Kumagai, N. andNishizawa, S. Yamasaki, H. Oheda, and K. Yamabe *Phys. Rev. B*, vol. 67, p. 195338, (2003).

[91] M. A. Albao, D.-J. Liu, C. H. Choi, and J. W. Gordon, M. S. andEvans *Surf. Sci.*, vol. 555, p. 51, (2004).

[92] F. Fuchs, W. G. Schmidt, and F. Bechstedt *Phys. Rev. B*, vol. 109, p. 17649, (2005).

[93] F. Fuchs, W. G. Schmidt, and F. Bechstedt *J. Phys. Chem. B*, vol. 109, p. 17649, (2005).

[94] R. Schlier and H. E. Farnsworth *J. Chem. Phys.*, vol. 30, p. 917, 1959.

[95] M. Ono, A. Kamoshida, N. Matsuura, E. Ishikawa, T. Eguchi, and Y. Hasegawa, "Dimer buckling of the si(001)2×1 surface below 10 k observed by low-temperature scanning tunneling microscopy," *Phys. Rev. B*, vol. 67, p. 201306, 2003.

[96] K. Sagisaka, D. Fujita, and G. Kido, "Phase manipulation between $c(4\times2)$ and $p(2 \times 2)$ on the si(100) surface at 4.2 k," *Phys. Rev. Lett.*, vol. 91, p. 146103, 2003.

[97] J. Showmaker, L. W. Burggraf, and M. S. Gordon *J. Chem. Phys.*, vol. 112, p. 2994, 2000.

[98] A. Ramstad, G. Brocks, and P. J. Kelly *Phys. Rev. B*, vol. 51, p. 14504, 1995.

[99] D. J. Chadi *Phys. Rev. Lett.*, vol. 43, p. 43, 1979.

[100] J. Ihm, D. H. Lee, J. D. Joannopoulos, and J. J. Xiong, "Structural phase diagrams for the surface of a solid: A total-energy, renormalization-group approach," *Phys. Rev. Lett.*, vol. 51, pp. 1872–1875, Nov 1983.

[101] T. Tabata, T. Aruga, and Y. Murata *Surf. Sci.*, vol. 179, p. L63, 1987.

[102] S. Yoshida, T. Kimura, O. Takeuchi, K. Hata, H. Oigawa, T. Nagamura, H. Sakama, and H. Shigekawa, "Probe effect in scanning tunneling microscopy on $si(001)$ low-temperature phases," *Phys. Rev. B*, vol. 70, no. 23, p. 235411, 2004.

[103] J. Nakamura and A. Natori *Phys. Rev. B*, vol. 71, p. 113033, 2005.

[104] K. Sagisaka, D. Fujita, and G. Kido *Phys. Rev. B*, vol. 71, p. 245319, 2005.

[105] L. Kantorovich and C. Hobbs *Phys. Rev. B*, vol. 73, p. 245420, 2006.

[106] K. Seino, W. G. Schmidt, and F. Bechstedt, "Energetics of si(001) surfaces exposed to electric fields and charge injection," *Phys. Rev. Lett.*, vol. 93, no. 3, p. 036101, 2004.

[107] T. Shirasawa, S. Mizuno, and H. Tochihara *Phys. Rev. Lett.*, vol. 94, p. 195502, 2005.

[108] A. I. Shkrebtii, R. Di Felice, C. M. Bertoni, and R. Del Sole *Phys. Rev. B*, vol. 51, p. R11201, 1995.

[109] M. Kutschera, M. Weinelt, M. Rohlfing, and T. Fauster *Appl. Phys. A*, vol. 88, p. 519, 2007.

[110] M. Weinelt, M. Kutschera, R. Schmidt, C. Orth, T. Fauster, and M. Rohlfing *Appl. Phys. A*, vol. 80, p. 995, 2005.

[111] M. Palummo, G. Onida, R. Del Sole, and B. S. Mendoza *Phys. Rev. B*, vol. 60, p. 1522, (1999).

[112] F. Fuchs, W. G. Schmidt, and F. Bechstedt *Phys. Rev. B*, vol. 72, p. p075353, (2005).

[113] F. Fuchs (2004). Master's thesis, Freidrich-Schiller-Universität.

[114] M. Palummo, G. Onida, R. Del Sole, and B. S. Mendoza *Phys. Rev. B*, vol. 60, p. 2522, 1999.

[115] J. E. Rowe and H. Ibach *Phys. Rev. Lett.*, vol. 31, p. 102, (1973).

[116] H. Ibach and J. E. Rowe *Phys. Rev. B*, vol. 10, p. 710, (1974).

[117] H. Ibach and J. E. Rowe *Phys. Rev. B*, vol. 9, p. 1951, (1974).

[118] R. Ludeke and A. Koma, "Oxidation of clean ge and si surfaces," *Phys. Rev. Lett.*, vol. 34, p. 1170, 1975.

[119] H. H. Farrell, F. Stucki, J. Anderson, D. J. Frankel, G. J. Lapeyre, and M. Levinson *Phys. Rev. B*, vol. 30, p. 721, (1984).

[120] L. Gavioli, M. Grazia Betti, C. Mariani, A. I. Shkrebtii, R. Del Sole, C. Cepek, A. Goldoni, and S. Modesti *Surface Science*, vol. 377–379, pp. 360–364, (1997).

[121] X. Gonze, J.-M. Beuken, R. Caracas, F. Detraux, M. Fuchs, G.-M. Rignanese, L. Sindic, M. Verstraete, G. Zerah, F. Jollet, M. Torrent, A. Roy, M. Mikami, P. Ghosez, J.-Y. Raty, and D. Allan *Comp. Mat. Sci.*, vol. 57, p. 478, 2002.

[122] The ABINIT code is a common project of the Université Catholique de Louvain, Corning Incorporated, and other contributors (`http://www.abinit.org`).

[123] QUANTUM-ESPRESSO is a community project for high-quality quantum-simulation software, based on density-functional theory, and coordinated by Paolo Giannozzi. See `http://www.quantum-espresso.org` and `http://www.pwscf.org`.

[124] `http://www.fhi-berlin.mpg.de/th/fhi98md/fhi98PP`.

[125] YAMBO is a code based on many-body perturbation theory for calculating excited states, and is released under the GPL 2.0 license. See A. Marini, C. Hogan, D. Varsano and M. Gruning, Comp. Phys. Commun. (submitted). See `http://www.yambo-code.org`.

[126] `http://www.yambo-code.org`.

[127] A. Shkrebtii and R. Del Sole *Phys. Rev. B*, vol. 70, p. 2645, (1993).

[128] B. S. Mendoza, F. Nastos, N. Arzate, and J. E. Sipe, "Layer-by-layer analysis of the linear optical response of clean and hydrogenated si(100) surfaces," *Phys. Rev. B*, vol. 74, p. 075318, (2006).

[129] C. D. Hogan and C. H. Patterson *Phys. Rev. B*, vol. 57, p. 14843, 1998.

[130] L. Kipp, D. K. Diegelsen, J. E. Northrup, L.-E. Swartz, and R. D. Bringans *Phys. Rev. Lett.*, vol. 76, p. 2810, 1996.

[131] C. Kress, A. I. Shkrebtii, and R. Del Sole *Surf. Sci.*, vol. 377–379, p. 398, 1997.

[132] V. I. Gavrilenko and F. H. Pollak *Phys. Rev. B*, vol. 58, p. 12964, 1998.

[133] M. Palummo, N. Witkowski, O. Pluchery, R. Del Sole, and Y. Borensztein *Phys. Rev. B*, vol. 79, p. 035327, (2009).

[134] F. Arciprete, C. Goletti, E. Placidi, P. Chiaradia, M. Fanfoni, F. Patella, C. Hogan, and A. Balzarotti *Phys. Rev. B*, vol. 68, p. 125328, 2003.

[135] S. Maruno, H. Iwasake, K. Horioka, S.-T. Li, and S. Nakamura *Phys. Rev. B*, vol. 27, p. 4110, 1983.

[136] `http://www.xcrysden.org/`.

[137] L. Hedin *Phys. Rev.*, vol. 139, p. A796, 1965.

[138] J. R. Baumvol *Surf. Sci. Rep.*, vol. 36, p. 1, 1999.

[139] Y. Borensztein, O. Pluchery, and N. Witkowski, “Probing the si-si dimer breaking of si(100)2 x 1 surfaces upon molecule adsorption by optical spectroscopy,” *Physical Review Letters*, vol. 95, p. 117402, 2005.

[140] T. Yamasaki, K. Kato, and T. Uda *Phys. Rev. Lett.*, vol. 91, p. 146102, (2003).

[141] C. G. Broyden *Journal of the Institute of Mathematics and its applications*, vol. 6, p. 76, 1970.

[142] R. Fletcher *Computer Journal*, vol. 13, p. 317, 1970.

[143] D. Goldfarb *Mathematics of Computation*, vol. 24, p. 23, 1970.

[144] D. F. Shanno *Mathematics of Computation*, vol. 24, p. 647, 1970.

[145] W. Jevons and L. A. Bashford *Proc. Phys. Soc. London*, vol. 49, p. 543, 1937.

[146] R. F. Barrow and H. C. Rowlinson *Proc. Phys. Soc. London A*, vol. 224, p. 374, 1954.

[147] M. E. Casida *Journ. Chem. Phys.*, p. 054111, 2005.

[148] M. E. Casida, *Recent advances in density functional methods, Part I.* Chong, D. P., World Scientific, Singapore, 1995.

[149] J. Guan, M. E. Casida, and D. R. Salahub *J. Mol. Struct.*, vol. 527, p. 229, 2000.

[150] G. Herzberg, *Molecular spectra and molecular structure. I. Spectra of Diatomic Molecules.* Van Nostrand Reinhold (New York), 1950.

[151] C.-O. Almbladh and U. von Barth *Phys. Rev. B*, vol. 31, p. 3231, (1985).

[152] M. Gruning, "Density functional theory with improved gradient and orbital dependent functionals," (2003). PhD thesis, Vrije Universiteit.

[153] M. Gruning, O. V. Gritsenko, S. J. A. van Gisbergen, and E. J. Baerends *Jour. of Chem. Phys.*, vol. 116, p. 9591, (2002).

[154] D. Sangalli (2007). Master's thesis, Universitá degli Studi di Milano (Italy).

[155] R. Colin and D. De Greef *Canad. J. Phys.*, vol. 53, p. 2142, 1975.

[156] A. Ipatov, F. Cordova, and M. Casida *preprint*, 2008.

[157] I. D. Petsalakis, G. Theodorakopouls, and C. A. Nicolaides, 1992.

[158] F. Birch *J. Geophys. Res.*, vol. 57, p. 227, 1952.

[159] F. Murnaghan in *Proc. Nat. Acad. Sci.*, (USA), p. 244, 1944.

[160] C. Kittel, *Introduction to Solid State Physics.* Wiley, 1996.

[161] J. F. van Acker, Z. M. Stadnik, J. C. Fuggle, H. J. W. M. Hoekstra, K. H. J. Buschow, and G. Stroink, "Magnetic moments and x-ray photoelectron spectroscopy splittings in fe 3s core levels of materials containing fe," *Phys. Rev. B*, vol. 37, p. 6827, (1988).

[162] J. Callaway, "Electronic energy bands in iron," *Phys. Rev.*, vol. 99, p. 500, (1955).

[163] M. Singh, C. S. Wang, and J. Callaway, "Spin-orbit coupling, fermi surface and optical conductivity of ferromagnetic iron," *Phys. Rev. B*, vol. 11, p. 287, (1975).

[164] M. Cococcioni, “A lda+u study of selected iron compounds,” (2002). PhD thesis, SISSA.

[165] S. Hüfner and G. K. Wertheim, “Core-electron splittings and hyperfine fields in transition-metal compounds,” *Phys. Rev. B*, vol. 7, p. 2333, 1973.

[166] C. S. Fadley, D. A. Shirley, A. J. Freeman, P. S. Bagus, and J. V. Mallow, “Multiplet splitting of core-electron binding energies in transition-metal ions,” *Phys. Rev. Lett.*, vol. 23, p. 1397, 1969.

[167] G. K. Wertheim, S. Hüfner, and H. J. Guggenheim, “Systematics of core-electron exchange splitting in 3*d*-group transition-metal compounds,” *Phys. Rev. B*, vol. 7, p. 556, 1973.

[168] P. B. Johnson and R. W. Christy, “Optical constants of transition metals: Ti, v, cr, mn, fe, co, ni and pd,” *Phys. Rev.*, vol. 9, p. 5056, (1974).

[169] M. Cazzaniga, “Ab initio approach to density response and excitation spectra in metallic systems,” (2008). PhD thesis, Universtiá degli Studi di Milano.

[170] L. Wang, T. Y. Chen, and C. Leighton, “Spin-dependent band structure effects and measurement of the spin polarization in the candidate half-metal $\cos_2$,” *Phys. Rev. B*, vol. 69, p. 094412, (2004).

[171] S. A. Wolf *Science*, vol. 294, p. 1488, 2001.

[172] I. Appelbaum, B. Huang, and M. D. J. *Nature*, vol. 447, p. 295, 2007.

[173] G. A. Prinz *Science*, vol. 282, p. 1660, 1998.

[174] H. S. Jarrett, W. H. Cloud, R. J. Bouchard, S. R. Butler, C. G. Frederick, and J. L. Gillson, “Evidence for itinerant d-electron ferromagnetism,” *Phys. Rev. Lett.*, vol. 21, p. 617, (1968).

[175] W. Folkerts, G. A. Sawatzky, C. Haas, R. A. de Groot, and F. U. Hillebrecht, “Electronic structure of some 3d transition-metal pyrites,” *J. Phys. C: Solid State Phys.*, vol. 20, pp. 4135–4144, (1987).

[176] I. J. Ferrer, D. M. Nevskaia, C. de las Heras, and C. Sanchez, “About the band gap nature of fes$_2$ as determined from optical and photo-electrochemical measurement,” *Solid State Communications*, vol. 74, pp. 913–916, (1990).

[177] L. Wang, T. Y. Chen, C. L. Chien, J. G. Checkelsky, J. C. Eckert, E. D. Dahlberg, K. Umemoto, R. M. Wentzcovitch, and C. Leighton, "Composition controlled spin polarization in $co_{1-x}fe_xs_2$: Electronic, magnetic and thermodynamic properties," *Phys. Rev. B*, vol. 73, p. 144402, (2006).

[178] D. W. Bullett, "Electronic structure of 3d pyrite- and marcasite-type sulphides," *J. Phys. C: Solid State Phys.*, vol. 15, pp. 6163–6174, (1982).

[179] G. L. Zhao, J. Callaway, and M. Hayashibara, "Electronic structures of iron and cobalt pyrites," *Phys. Rev. B*, vol. 48, p. 15781, (1993).

[180] T. Shishidou, A. J. Freeman, and R. Asahi, "Effect of gga on the half-metallicity of the itinerant ferromagnet cos_2," *Phys. Rev. B*, vol. 64, p. R180401, (1974).

[181] I. I. Mazin, "Robust half metalicity of $co_{1-x}fe_xs_2$," *Appl. Phys. Lett.*, vol. 77, p. 3000, (2000).

[182] L. Wang, K. Umemoto, R. M. Wentzcovitch, T. Y. Chen, C. L. Chien, J. G. Checkelsky, and J. C. Eckert, "$Co_{1-x}fe_xs_2$: A tunable source of highly spin-polarized electrons," *Phys. Rev. Lett.*, vol. 94, p. 056602, (2005).

[183] K. Ramesha, R. Seshadri, C. Ederer, T. He, and M. A. Subramanian, "Experimental and computational investigation of structure and magnetism in pyrite $co_{1-x}fe_xs_2$: chemical bonding and half metallicity," *Phys. Rev. B*, vol. 70, p. 214409, (2004).

[184] S. F. Cheng, G. T. Woods, K. Bussmann, I. I. Mazin, R. J. J. Soulen, E. E. Carpenter, B. N. Das, and P. Lubitz, "Growth and magnetic properties of single crystal $fe_{1-x}co_xs_2$ (x=0.35-1)," *J. App. Phys.*, vol. 93, p. 6847, (2003).

[185] A. K. Mabatah, E. J. Yoffa, P. C. Eklund, M. S. Dresselhaus, and D. Adler *Phys. Rev. Lett.*, vol. 39, p. 494, (1977).

[186] R. W. G. Wickoff, *Crystal structures*, ch. Vol. 1. Interscience, New York, 1965.

[187] N. Marzari, "Ab-initio molecular dynamics for metallic systems," (1996). PhD thesis, University of Cambridge.

[188] T. A. Bither, R. J. Bouchard, W. H. Cloud, P. C. Donohue, and W. J. Siemons *Inorganic Chemistry*, vol. 1445, p. 2208, 1968.

[189] S. Lauer, A. X. Trautwein, and F. E. Harris *Phys. Rev. B*, vol. 29, p. 6774, 1984.

[190] H. van der Heide, H. R., C. F. van Bruggen, and C. Haas *J. Solid State Chem.*, vol. 33, p. 17, 1980.

[191] K. Kikuchi, T. Miyadai, H. Itoh, and T. Fukui *J. Phys. Soc. Jpn.*, vol. 45, p. 44, 1978.

[192] J. A. Wilson and G. D. Pitt *Philosophical Magazine*, vol. 23, p. 1971, 1971.

[193] A. Savitzky and M. J. E. Golay *Analytical Chemistry*, vol. 36, p. 1627, 1964.